On Dephasing and Exciton Transfer in Light-Harvesting Complexes

by

Maria Ilaria Mallus

a Thesis submitted in partial fulfillment
of the requirements for the degree of

Doctor of Philosophy in Physics

Approved Dissertation Committee

_____
Prof. Dr. Ulrich Kleinekathöfer
(Jacobs University Bremen)

_____
Prof. Dr. Jürgen Fritz
(Jacobs University Bremen)

_____
Prof. Dr. Carles Curutchet
{University of Barcelona)

Date of Defense: May 31st, 2017

Department of Physics & Earth Sciences

Abstract

Photosynthesis is the main energy source in plants, algae and different types of bacteria, such as purple and green sulphur bacteria. The primary step in photosynthesis is represented by the photo excitation of the light harvesting (LH) pigment present in the organism. Subsequently, the excitation delocalizes among the pigments due to the electronic couplings between them. The excitation energy is then transferred to neighboring LH systems and finally to the reaction center (RC) where charge separation occurs. During the last decades many studies have been carried out in order to understand the optical and the exciton transfer properties of the LH complexes. Nevertheless, a full understanding has not yet been achieved. In particular, the experimentally-observed long-lived coherences as well as dephasing processes have attracted the attention of the scientific community in recent years.

The present thesis aims at contributing to the understanding of these processes. To this end,, different methods have been employed, such as molecular dynamics simulations, quantum-chemistry methods and wave packet dynamics calculations. The combination of these methods allows a more detailed theoretical description of the studied LH systems. The dephasing phenomenon is discussed in the first half of the thesis. In this work, an analytic and a numerical methodology has been developed to relate it to the energy gap fluctuation. This formalism has been applied to the case of both single pigments and whole complexes. It can be concluded that a universal relation exists between these two entities, independently from the system and from the method used to obtain such quantities.

The second half of this thesis consists of combined molecular dynamics and quantum approaches applied to different systems. In the first application, three different LH systems are discussed and compared in detail. The role of the environment in determining the excitation-energy transfer properties of such complexes is discussed as well. In the second application, the photo-active part of a bio-inspired solar cell is studied. Diffusion properties have been analyzed, resulting in a clear importance of quantum effects in enhancing the diffusion of the excitation energy within the system.

Contents

Chapter 1

Light-Harvesting Systems

Solar energy is the main energy source on our planet. Photosynthesis is a light induced process wherein plants, algae and bacteria convert light into chemical energy [1]. This energy is then stored in carbohydrates, obtained from carbon dioxide and water. Photosynthesis consists of three important steps [2]. The light is first harvested from sunlight and then used to produce energy in the form of ATP. This energy is used for the conversion of CO_2 into cabohydrates. The general equation for such conversion is reported in Eq. 1.1, in which H_2X denotes the reducing agent and CH_2O the carbohydrate

$$CO_2 + 2H_2X + \text{photons} \rightarrow [CH_2O] + 2X + H_2O. \tag{1.1}$$

In oxygenic photosynthesis, the oxidation of water provides electrons and eventually oxygen is produced [3]. This type of photosynthesis takes place in plants, algae and cyanobacteria. In bacteria (except cyanobacteria), anoxygenic photosynthesis takes place. In this case, other compounds as arsenites are used instead of water as electrons source, and oxygen is not produced [4]. Many geochemical evidences show how oxygenic photosynthesis has evolved from the anoxygenic one, due to the anoxic atmosphere on our planet up until 2.4 billion years ago [5]. The first experiments on photosynthesis were performed in 1932 by Emerson and Arnold [6]. They suggested that about 2500 chlorophyll molecules are required for the production of a single oxygen. Two years later, the existence of such molecules called "chlorophyll units" was confirmed by Arnold and Kohn [7]. The discussion on the minimum number of chlorophylls and photons required for the reaction was open for a long time: a single chlorophyll molecule takes 1 hour to capture 4-12 photons, the number required for the evolution of an oxygen molecule [8] (for a review on the topic, see Ref. [9]). The idea of a quantum transfer of energy was firstly proposed by Wohl [8]. In his work, the "pigment molecule" absorbs and transfers the energy very efficiently to the "center" , where the charge separation

occurs. Nowadays, these two components are known as "photosynthetic unit" and "reaction center" respectively. However, despite the quantum nature of the energy transfer is clear since 60 years, the debate on the reason behind its efficiency is still open. The energy transfer in LH systems is, in fact, an highly efficient process [10], and many theoretical and experimental studies have been carried out [11, 12] to better understand it. It has recently been shown that the energy transfer shows a quantum wave-like mechanism at cryogenic temperature [13–16], even if the coherence phenomenon in vivo is still under study [17]. In particular, theoretical investigations show how coherence and dephasing effects at room temperature are essential to maintain the strength of the transfer process [18–21]. These two phenomena need to be understood. The so-called "long lived coherence" of the quantum energy transfer was revealed for the first time by Brixner and co-workers in 2005 for the FMO complex [22] at 77K and 5 years later, at room temperature, by the Engel research group for the same complex [23]. A similar feature has been found for other complexes and for the PE545 system in particular in 2010 [24]. It has been supposed that the long-lived coherence is due to the correlation of site energy fluctuations [25] and various works reported the possibility of correlated motions [20, 26–30]. However, it has been shown [31] that those correlations are improbable in the FMO complex and other reasons for such long coherence have to be found. Moreover, dephasing processes must be taken into account in the analysis of the efficiency of the energy transfer, and the first part of the present thesis aims of contributing the acquaintance of the dephasing phenomenon. These recent investigations show how the wave-like energy transfer mechanism can contribute to the near-perfect quantum efficiency of photosynthesis only if coherences survive long enough in these systems during energy transfer at physiological temperatures [23]. However as the temperature increases, a second phenomenon, the dephasing, plays an important role: the thermally excited vibrational modes of the bath, in fact, accelerate decoherence, resulting in the lost of the quantum nature of the energy transfer. Therefore, the interplay between quantum cohernce and dephasing is responsible for the high efficient energy transfer. If such equilibrium is guaranteed, a fast and unidirectional transfer within the photosynthetic complexes is present [20] and the near-unity efficiency is reached.

However, the debate on the near-perfect quantum efficiency is still open and many questions need to be addressed to exploit the mechanism of the photosynthesis to build artificial photosynthetic devices [32].
In this chapter, the light harvesting complexes studied in this thesis work will be presented. These include the light-harvesting complexes 2 and 3 (LH2 and LH3) (Sec. 1.1), the Fenna-Matthews-Olson (FMO) complex (Sec. 1.2), the Phy-

coerythrin (PE) complexes (Sec. 1.3) and the Metal Organic Framework (MOF) complexes (Sec. 1.4).

1.1 The LH2 and LH3 Complexes

The light harvesting complex 2 (LH2 complex) is an antenna complex of purple bacteria [33], prokaryotes widely spread in lakes and ponds. In these bacteria, anoxigenic photosynthesis takes place [4]. LH2 complexes absorb light and subsequently transfer the excitation energy to the reaction centers. They are one of the most well investigated light-harvesting complexes [34–40]. As can be seen in Fig. 1.1, the LH2 complex shows a symmetric structure: it is arranged in two rings, the B800 and the B850 ring, which absorb at 800 nm and 850 nm respectively. The two rings are composed of $\alpha-\beta$ subunits, each of them formed by one trans-membrane protein, three bacteriochlorophylls a (BChls a) and one carotenoid. Carotenoids are chromophores and their role is multifold: they act as antioxidant agents, they contribute to the light harvesting process absorbing in the blue-green region and they transfer the excitation energy [41]. Purple bacteria living in low-light conditions show a modified version of the LH2 complex, called LH3 complex, in which the B850 band presents a blue shift with a peak at 820 nm. Some bacteria present both LH2 and LH3 complexes to increase the spectrum range [42]. The first crystal structures have been solved in 1995 by McDermott and co-workers [44] for the bacterium *Rhodoblastus acidophila* and in 1996 by Koepke et. al. [45] for the bacterium *Rhodospirillum molischianum*. The structures represented the starting point for the comprehension and the molecular-level study of the light harvesting mechanism [44]. The structure is well conserved in all bacteria, while the number of composing pigments, varies with the bacteria species (27 BChls are present in *Rhodopseudomonas acidophila*, while 24 are found in *Rhodospirillum molischianum*). The carotenoids (Car) increment the spectral width [33]. As shown in Fig. 1.1, the two rings are differently arranged: on the one hand, the 8 (or 9) BChls of the B800 ring are arranged in a plane parallel to the membrane plane and they are 21 Å apart from their neighboring BChls, which makes the coupling between them weak and therefore the excited states are well localized on the BChls. The excitation energy transfer (EET) takes place on a 400 fs time scale [33]. On the other hand, the B850 plane is perpendicular to the membrane plane and the 16 (18) BChls are closely spaced with an inter-BChl distance of about ~ 9Å: the coupling between them is strong, and, in turn, an high delocalization of the excited states (excitonic states) for this ring has been observed [46, 47]. Another consequence of the delocalization is the different excitation energy transfer ($\sim$ 100 fs) [33]. This

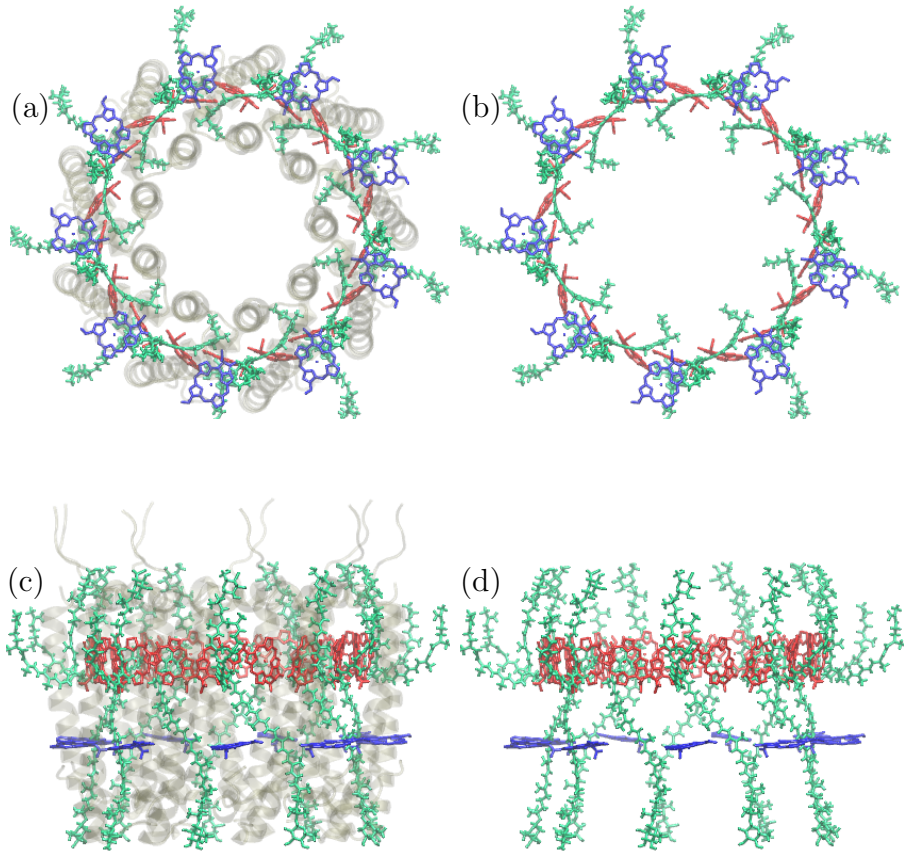

Figure 1.1: Structure of LH2 of *Rhodoblastus acidophila*. Top view of the whole pigment-protein complex (a) and of BChls and carotenoids (b). Side view of the whole pigment-protein complex (c) and of BChls and carotenoids (d). For clearness, the BChls tails are not displayed. The B850 and B800 are displayed in red and blue respectively, carotenoids in green and the apoprotein in gray. The figures were obtained using the VMD program [43].

structural difference is reflected in the different absorption bands of the two rings. A recent study [48], based on simulations of the 2D spectra, has shown that delocalized states shared by the two rings are responsible for the energy transfer from the B850 to the B800 ring. This step takes place in about 1 ps [33]. The excitation is then transferred to another LH2 complex, or to the light harvesting complex 1 (LH1) (in 2-5 ps, depending on the species [33]), and from there to the reaction center (RC), where the charge separation occurs. The whole EET process takes 20-50 ps to occur [49].

1.2 The FMO Complex

The Fenna-Matthews-Olson (FMO) complex is a water-soluble complex of green sulfur bacteria [50] and has the biological role of transferring the excitation energy from the chlorosome, the main LH antenna of green sulfur bacteria and the largest LH antenna system identified in nature [51], to the reaction center. Its location in the photosynthetic apparatus is depicted in Fig. 1.2 (c). The FMO complex

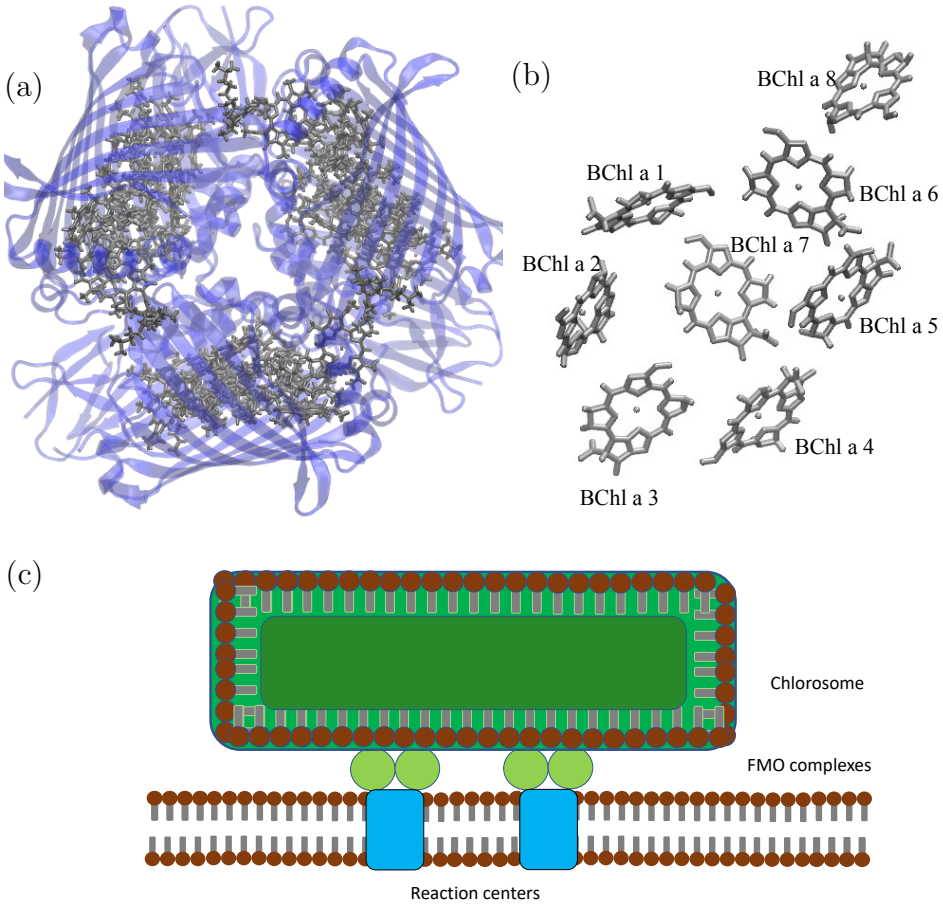

Figure 1.2: (a) Structure of the FMO trimer from the bacterium *Prosthecochloris aestuarii*. Protein and BChls are drawn in blue and gray respectively. (b) Arrangement of the 8 BChls in the FMO monomer. For the sake of clarity, tails are omitted. The figures were obtained using the VMD program [43]. (c) Location of the FMO complex in the light-harvesting apparatus.

was the first pigment-protein complex to be analyzed at atomic level. It was

crystallized for the first time in 1974 by Fenna, Matthwes and Olson. resulting in the name of the system [52]. In their work, the authors showed the presence and the spatial distribution of three monomers, each of them containing seven BChls a. Two other structures of the FMO complex were solved over the years [53,54], but the presence of an eighth BChl a was revealed only in 2009 [55]. This BChl a 8 is believed to serve as a linker between the chlorosome and the other BChls of the monomer [33]. The BChls are bound to the protein scaffold via the central magnesium atom [52]. The structure is shown in Fig. 1.2. Differently from the LH2 case described in Sec. 1.1, the spectral properties of the FMO are mostly determined by the electrostatic protein-pigment interaction, which results in localized site energies, tuned by the protein environment. The prediction of the site energies has been a challenging task since the structure was solved, and an agreement between theoretical studies and experimental evidences was achieved in 2009 only [56]. In 2011, the Kleinekathöfer and Aspuru-Guzik groups [31, 57] performed QM/MM calculations able to compute the spectral densities of the BChls. In addition to that, the authors gave an important contribution on the understanding of the role of thermal fluctuations in the long-lived coherence phenomenon observed in light harvesting systems. Engel and co-workers observed the phenomenon of the long-lived quantum coherence for the FMO complex in in 2007 [13]. After almost a decade of debate on the role of quantum coherence, Wilkins and Dattani showed the quantum coherences are probably not important in maintaining the efficiency of the transfer process in the case of the FMO complex [58]. Nevertheless, the debate is still open and the reason for such high efficiency is still not clear.

1.3 The Phycoerythrin Complexes

Phycoerythrin (PE) 545 and 555 are the antenna components of the cryptophytes, photosynthetic algae present in marine and fresh water environments. The light-absorbing pigments in cryptophytes are BChls a, BChls c_2 and bilins, located in the PE complexes. Phycoerythrins, are part of the phycobilin protein family: the chromophores (called phycobilins) are, in fact, covalently bound to a protein part [59]. They capture light and transfer the energy to the reaction center [60]. The crystal structure of the PE545 complex from the marine cryptophyte *Rhodomonas CS24* has been solved in 1999 for the first time [61,62], while the one of the PE555 system only in 2014 for the *Hemiselmis andersenii* specie [63]. The phycoerythrin systems are water soluble and are located in the lumen of the thylakoid membrane [64]. As shown in Fig. 1.3, they are composed by a quaternary structure, with

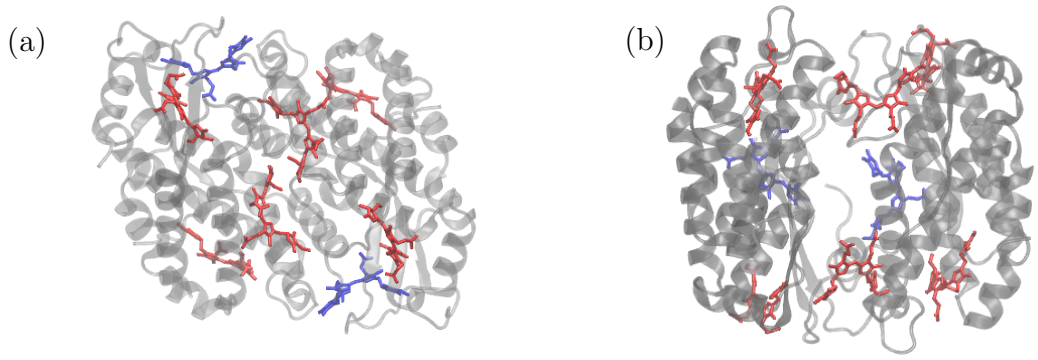

Figure 1.3: (a) Structure of PE545 complex from the marine cryptophyte *Rhodomonas sp. CS24*. (b) Structure of PE555 complex from the cryptophyte *Hemiselmis andersenii*. DBVs, PEBs and protein are displayed in blue, red and gray respectively. The figures were obtained using the VMD program [43].

two $\alpha\beta$ subunits, in which eight light-absorbing bilins are covalently bounded to the protein scaffold [64] via single or double bonds. The bilins are linear chains of four pyrrole rings (tetrapyrroles) and they are formed as a metabolic products of porphyrins in many organisms. Porphyrins are organic compounds, formed by four modified tetrapyrroles interconnected via methine bridges (=CH-). Two different types of bilins are present in the PE complexes: dihydrobiliverdin (DBV) and phycoerythrobilin (PEB), which differ in the absorption spectrum. The presence of bilins as a composing pigments (instead of BChls as it is for LH2 and FMO complexes), is due to the less amount of accessible light in marine environments: such organisms, in fact, have evolved to absorb light in the 450-640 nm spectrum, a range in which the chlorophyll absorption is negligible [64]. As it can be seen in Fig. 1.3, the difference between PE545 and PE555 complexes is the presence, in the latter complex, of a water-filled channel as a consequence of a $\sim 73^\circ$ rotation of the two monomers caused by steric effects due to the presence of a single amino acid [63]. The first evidence of quantum coherence in PE complexes was observed in 2010 by Collini and co-workers [24] and the site correlation among pigments was then studied via MD QM/MM simulations [65]. The same scheme was then used by Aghtar et. al. in 2014 [66] to study the individual spectral densities and in particular how, in contrast to the case of the FMO complex, the low frequency features of the spectrum are due to internal modes and not to the environment. The energy transfer in the PE systems takes place on a time-scale of 20-50 ps [67].

1.4 The Bio-Inspired MOF Complex

In the last decades, the need of artificial photovoltaic devices has received enormous attention. Even if such devices are usually made of inorganic semiconductors, organic based solar cells have recently been proposed. Organic solar cells are photovoltaic devices that uses conductive organic polymers or small organic molecules for converting the absorbed light into electricity via the photovoltaic effect [68]. On the one hand, compared to the standard silicon-based devices, organic solar cells are cheaper [69], more flexible and they have less environmental impact [70]. On the other hand, organic solar cells are less efficient [71] and they experience severe photochemical degradation [72]. Due to these two aspects, however, the field of organic solar cells became very popular and many researchers are currently working on improvements. In 2015, a 10% efficiency was obtained [73]. In this thesis, a photovoltaic organic system has been studied [74]. It consists of ordered arrays of porphyrins which make a particular class of hybrid compounds called metal organic framework (MOF). The device has been constructed and analyzed by Liu and co-workers [74], and its schematic representation is reported in Fig. 1.4. As reported in their work, the SURMOFs (surface grafted MOFs)

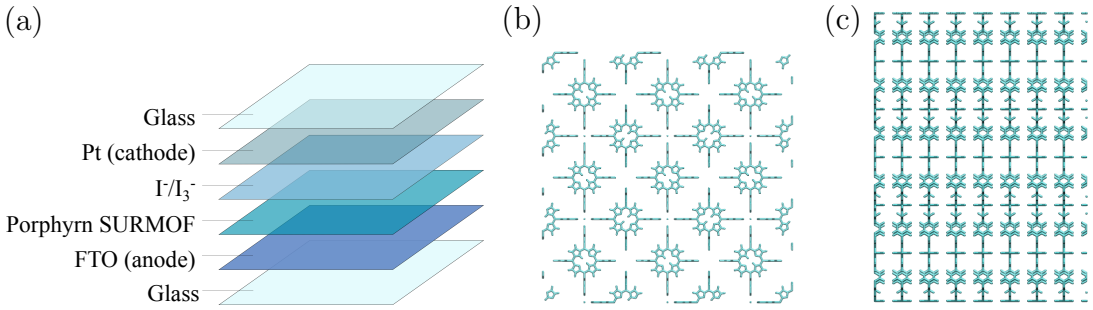

Figure 1.4: Schematic representation (a) of a porphyrin SURMOF based solar cell. Front (b) and side (c) view of the porphyrin layers. The figures in panels (b) and (c) were obtained using the VMD program [43].

are grown in a layer-by-layer way on a FTO (fluorine-doped tin oxide) substrate, which serves as anode. The cathode is made of iodine/triiodine electrolyte. In this way, a photovoltaic cell has been constructed (See Fig. 1.4), as explained in detail in Ref. [74]. Here, the porphyrin layers have been computationally generated and characterized, starting from a unitary box configuration. In fact, similarly to the studies already mentioned in the previous sections 1.1, 1.2, 1.3, a combined ap-

proach has been used to determine thermal fluctuations, excitation energies and couplings, and diffusion coefficient. The configuration used in this work is reported in Fig. 1.4. The diffusion coefficient is a key quantity to measure the exciton diffusion among the systems, giving a measure of the exciton lifetime. In Chapter 7 it will be shown that the quantum diffusion coefficient is higher than its classical limit, confirming how the quantum effects contribute to the high efficiency of the excitation energy transfer processes in photosynthetic systems.

Chapter 2

Summary of Results

In this Chapter, a brief overview of the thesis is reported. The rest of the thesis will be organized in five Chapters: the first one provides the theoretical and computational background, to better understand the results obtained in the present work, reported in the other four Chapters. The study of dephasing processes is the focus of the first half of the thesis, as it will be described later. In the second part of the present work, a comparison between LH2 and LH3 complexes of two different bacteria will be presented, as well as a study on the exciton transfer dynamics in a MOF system.

2.1 Theoretical Background

Chapter 3 provides the theoretical background needed to understand the dephasing and dynamic properties of LH complexes and the simulations methods adopted to study these phenomena. It starts with a detailed description of the Hamiltonian of the system, the core of the information used to describe the properties of the analyzed systems. This part is divided in three Sections, one for each part of the Hamiltonian: the System (Sec. 3.1), the Bath (Sec. 3.2) and the System-Bath interaction (Sec. 3.3) Hamiltonians. Simulations techniques used to obtain each term are reported as well. Next, Sec. 3.4 focuses on the equations used to derive the exciton transfer properties and the population dynamics of the system under study. The Section 3.5 describes the simulation technique called "Molecular Dynamics (MD)" used to compute the dynamics of the ground states of the system under study. The Chapter ends with a Section (3.6) dedicated to the dephasing phenomenon, which has been studied in the next 4 and 5 Chapters.

2.2 Dephasing Time Vs Energy Gap Fluctuation

In Chapter 4, the method developed to study a relation between dephasing time and energy gap fluctuation will be presented. Such a relation was found by Akimov and Prezhdo [75] by fitting the data from the excitonic gaps of an artificial system. In the present work, the relation has been analytically derived and tested to numerical data of single pigments of different systems. In this case, only the gap between ground and first excited state has been considered. The data set includes systems in which exciton transfer occurs (LH2, FMO and PE545 complexes) as well as systems in which charge transfer occurs (DNA, DNA Photolyase and Cryptochrome). Such a relation has been found to be independent from the system analyzed and from the method used in the simulations. The Chapter starts with an introductory Section 4.1 on the state-of-art of the computational study of LH systems and on the important quantities analyzed in the work. Sec. 4.2 describes in detail Kubo's generalized theory and the approximations used to derive the relation between dephasing time and energy gap fluctuation. The results based on this theoretical background are reported in Sec. 4.3. The procedure used to obtain such a relation can be followed step by step through the study of the functions reported in the graphs in this Section. The Chapter ends with Conclusions and Acknowledgments (Sec. 4.4). The present study was published in the Journal of Physical Chemistry Letters.

2.3 Vibrational Dephasing Time

In Chapter 5, an extension of the method presented in Chapter 4 will be presented. The method, in fact, has been applied to the study of the whole complexes. In this study, site energies of single pigments as well as the couplings between them have been evaluated and the system Hamiltonians have been built and diagonalized. In this way, excitonic states of the whole complex have been obtained and the relation between each excitonic gap and dephasing time has been analyzed. Neighboring gaps, as suggested by Akimov and Prezhdo [75], have been considered as well. The data set includes different light harvesting complexes such as FMO, LH2, PE545 and PE555 complexes. Again, it can be concluded that a universal relation between the two quantities exists, although the proportionality constant varies among complexes, even if composed by the same pigments. The initial decay of the autocorrelation functions, again, determines the constant. The Chapter starts with an Introduction (Sec. 5.1) on dephasing processes in LH complexes, followed by a Section (Sec. 5.2) in which the details of the molecular simulations

are reported. The Hamiltonian used to obtain the excitonic states is presented in the next Sec. 5.2.2 together with the "avoided crossings" approximation adopted in this work. Since the Hamiltonian of the whole system has been diagonalized at each time step, the problem of the site contribution among the trajectory is discussed in Sec. 5.5.2. The next Sec. 5.3 contains results obtained in this work. The actual discussion of the results is given in Sections 5.3.1, 5.3.2 and 5.3.3, where the results for autocorrelation functions, dephasing functions and times, and neighboring energies are discussed, respectively. The Chapter ends with Conclusions and Acknowledgments (Sec. 5.4). These findings were published in the Journal of Physical Chemistry B.

2.4 LH2 and LH3 Theoretical Study

In Chapter,6 a comparison of the properties of three different light-harvesting systems will be presented. The systems are the LH2 complex of *Rsp. molischianum*, the LH2 complex of *Rbl. acidophilus* and the LH3 complex of *Rbl. acidophilus*. In this work, different methods have been applied: MD simulations have been performed to compute the thermal fluctuations of the ground states of the pigments, on top of which quantum chemical calculations have been performed to determine site energies and their distributions, autocorrelations functions and spectral densities. Coupling between pigments has been determined as well, together with the population dynamics for the three systems. The Chapter starts with an Introduction (Sec. 6.1) and with a description of the systems under study, in Sec. 6.2. The results are presented in Sec. 6.3. Here, a full comparison between systems is presented and environmental effects are discussed as well. It can be concluded that the pigments of the three systems behave quite similar, as expected, although different environments play different roles, as it will be shown in the coupling and population dynamics discussions. Conclusions are given in the last Sec. 6.4.

2.5 The Porphyrin-MOF Complex

In Chapter 7, the analysis of the exciton transfer properties of the porphyrin-based Surface-grafted Metal Organic Framework (SURMOF) system will be presented. The system was built by Liu et. al. [74] to create an organic solar cells by using ordered arrays of porphyrins as the organic light-absorption molecules. The focus of the present contribution is the study of the exciton transfer properties of such a lattice. The Chapter starts with an Introduction 7.1 on the system, followed by Sec. 7.2, in which theoretical background and methods are described in detail.

This Section is divided in two sub-sections: the first one focuses on the single-pigment analysis (Sec.7.2.1), while the second one (Sec. 7.2.2) on the inter-pigment analysis. The Results Section (Sec. 7.3) firstly describe the system setup in Sec. 7.3.1. The discussion continues with the single-pigment analysis, where density of states, autocorrelation functions and spectral densities are reported (Sec. 7.3.2). Here it will be shown how internal modes determine the behavior of the single porphyrin. The next Sec. 7.3.3 focuses on the analysis of the coupling between porphyrins and on the exciton transfer properties of the systems. The diffusion coefficient is computed and compared to its classical limits, comparison that shows the importance of the quantum effects on the exciton transport. Conclusions are given in the last Sec. 7.4, together with future plans.

Chapter 3

Theoretical Background and Methods

In recent years, novel quantum chemical methods have been proposed to investigate the properties of LH complexes [76, 77]. These methods are based on the approximated solution of the Schrödinger equation (Eq. 3.1). Due to the big size of the LH systems, their fully quantum mechanical description can not be performed yet, because of the enormous computational cost associated to these calculations [77]. For this reason, two different approaches are, in general, used to study the time evolution and the properties of these systems. The first one is based on the so-called "reduced density matrix methods" [78, 79]. In this scenario, the spectral densities are obtained by different methods such as, for example, the solution of the hierarchy equations of motion (HEOM) [80,81], set of equations that describes the time evolution of a system coupled to a bath [81]. The second approach is a mixed classical-quantum study, based on classical dynamic simulations (a technique presented in Sec. 3.5) on top of which quantum chemical calculations are performed to study phenomena like exciton transfer. Several approaches of this kind exist, but the most widely used are based on the surface hopping method [82] and on the mean-field Ehrenfest dynamics [83, 84], known as "ensemble-averaged wave packet dynamics". This second approached is used in the present work to evaluate the population dynamics and it is presented in Sec. 3.4. Aghtar et. al. recently presented a nice comparison between such two approaches [85]. In their work, the authors showed how in the weak system-bath coupling limit, the two approaches yield very similar results. The theoretical background is presented in Sections 3.1, 3.2, 3.3, as well as a method used to determine key quantities like the dephasing time is presented in Sec. 3.6.

The information on the system is contained in the Hamiltonian of the time-

dependent Schrödinger equation (Eq. 3.1) [86, 87]

$$i\hbar\frac{\partial\Psi_T(t)}{\partial t} = H_T(t)\Psi_T(t). \tag{3.1}$$

Here, H_T denotes the total Hamiltonian of the system H_T and it can be split into three terms,

$$H_T = H_S + H_B + H_{SB}. \tag{3.2}$$

H_S, H_B and H_{SB} in this equation are the system, bath and system-bath interaction Hamiltonians, respectively. This architecture is represented in Fig. 3.1. The total

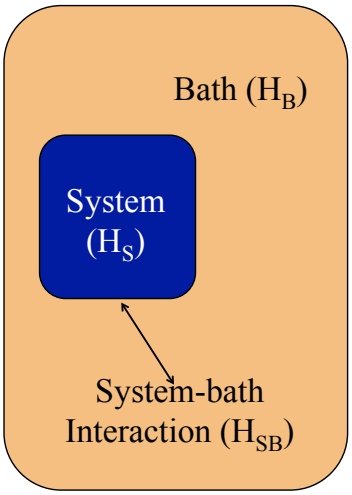

Figure 3.1: Schematic representation of the system-bath classification.

Hamiltonian is constructed for each time step of the trajectory that describes the time evolution of the system. A more precise discussion concerning the calculation of these quantities is given in the next 3.1, 3.2 and 3.3 Sections.

3.1 System Hamiltonian: H_S

H_S is the electronic Hamiltonian that describes the LH systems. It can be represented by a $N \times N$ matrix for a system composed by N pigments, see Eq. 3.3, where the diagonal elements are the gaps between the ground and the first excited states ϵ_i of the single chromophores and the off-diagonal elements are the couplings V_{ij} between them,

$$H_S = \sum_{i}^{N} \epsilon_i |i\rangle\langle i| + \sum_{i\neq j}^{N} V_{ij}|i\rangle\langle j|. \tag{3.3}$$

The methods used to calculate the site energies and the couplings of H_S are described in the next Sections 3.1.1 and 3.1.2, respectively.

3.1.1 Site Energies

To calculate the site energies in Eq. 3.3, the Schrödinger equation must be solved and several approximations must be adopted to do so. The first is the Born-Oppenheimer (B-O) approximation [88]. The B-O approximation is based on the assumption that electrons are much faster and lighter than nuclei, so the electronic and nuclear degrees of freedom can be separated. The electronic Hamiltonian is defined in Eq. 3.4, where m_e denotes the electron mass, N_e the number of electrons, N_n the number of nuclei, $\vec{r}$ and $\vec{R}$ the electron and nuclei coordinates, Z the atomic number and e the electron charge [89].

$$H_e = -\frac{\hbar^2}{2m_e}\sum_{i}^{N_e}\nabla_i^2 + \sum_{i}^{N_e}\sum_{\alpha}^{N_n}\frac{Z_\alpha e}{|\vec{R}_\alpha - \vec{r}_i|} + \sum_{i,k>i}^{N_e}\frac{e^2}{|\vec{r}_i - \vec{r}_k|} + \sum_{\alpha,\beta>\alpha}^{N_n}\frac{Z_\alpha Z_\beta e^2}{|\vec{R}_\alpha - \vec{R}_\beta|} \quad (3.4)$$

Eq. 3.4 contains the kinetic term for electrons, electron-nuclei, electron-electron and nuclei-nuclei Coulomb interactions respectively. It can be re-written as 3.5, where H_i groups the first two terms of Eq. 3.4 and represents the one-electron Hamiltonian, while V_{ee} and V_{nn} correspond to the last two terms of Eq 3.4.

$$H_e = \sum_{i}^{N_e} H_i + \sum_{i,k>i}^{N_e} V_{ee} + \sum_{\alpha,\beta>\alpha}^{N_n} V_{nn} = H_e^* + \sum_{\alpha,\beta>\alpha}^{N_n} V_{nn} \quad (3.5)$$

The electronic wave function Φ_i is called "molecular orbital" and each orbital can be occupied according to the Pauli principle. Molecular orbitals are obtained by the LCAO (Linear Combination of Atomic Orbitals) approximation [90], as shown in Eq. 3.6, where C_{ki} is the coefficient matrix.

$$\Phi_i = \sum_k C_{ki}\phi_k \quad (3.6)$$

Eq. 3.7 must be solved and electron wave functions Φ_i and orbital energies must be obtained.

$$H_e^*\Phi_i = \epsilon_i\Phi_i \quad (3.7)$$

The Hartree-Fock method, used to solve Eq. 3.7 will be presented in the next Section, as well as the semi-empirical method used in the present thesis.

Hartree-Fock Method

The Hartree Fock (HF) or self-consistent field (SCF) method it is a method used to approximate the Schrödinger equation in order to determine the electronic wave functions and the site energies [91]. The HF method makes use of several approximations:

- the B-O approximation, discussed above;
- the relativistic effects are not taken into account;
- the Slater determinant [92] is used as a solution of the Schrödinger equation, and it satisfies the antisymmetric property of the wave function and the variational principle;
- the mean field approximation is introduced to solve each electronic equation; each electron in fact, feels the mean field generated by the presence of the other electrons of the system via an effective Hamiltonian.

Following these approximations, the Fock equation can be written as Eq. 3.8 where H_i is the one-electron Hamiltonian (first two terms of Eq. 3.4), and J and K are the Coulomb and the exchange integrals respectively

$$\left[H_i(\vec{r}_1) + \sum_{i \neq j} J_j(\vec{r}_1) - \sum_{i \neq j} K_j(\vec{r}_1) \right] \Phi_i(\vec{r}_1) = \epsilon_i \Phi_i(\vec{r}_1) \tag{3.8}$$

J and K integrals are reported in Eq. 3.9. J defines the electron-electron repulsion of the two electrons of the j-th orbital, while K takes into account the antisymmetry of the wave function.

$$\begin{aligned} J_j(\vec{r_1}) &= \int d^3 r_2 |\Phi_j(\vec{r}_2)|^2 \frac{1}{|\vec{r}_2 - \vec{r}_1|} \\ K_j(\vec{r_1}) &= \int d^3 r_2 \Phi_j^*(\vec{r}_2) \frac{1}{|\vec{r}_2 - \vec{r}_1|} \Phi_i(\vec{r}_2) \end{aligned} \tag{3.9}$$

Eq. 3.8 can be solved numerically by following the scheme reported in Fig. 3.2, i. e. to obtain the eigenfunctions and the eigenstates of Eq. 3.7. The method is called "self-consistent" because the solution of the Schrödinger equation depends implicitly on the equation itself. Starting from the coordinates of the nuclei, the orbitals are built used to form the Fock matrix, which is then diagonalized. If the calculation converged, the site energies are obtained. If not, the solution is used as a input for a new calculation and the procedure is repeated iteratively until convergence is reached (e.g., the Fock matrix does not change within a certain accuracy). Because the two-electron integrals, the computational cost required to implement the HF method scales as N_e^4 [89]. The size of the LH systems makes a direct usage of the HF method impossible. DFT and semi-empirical based methods are used instead. In this thesis work the latter ones have been used.

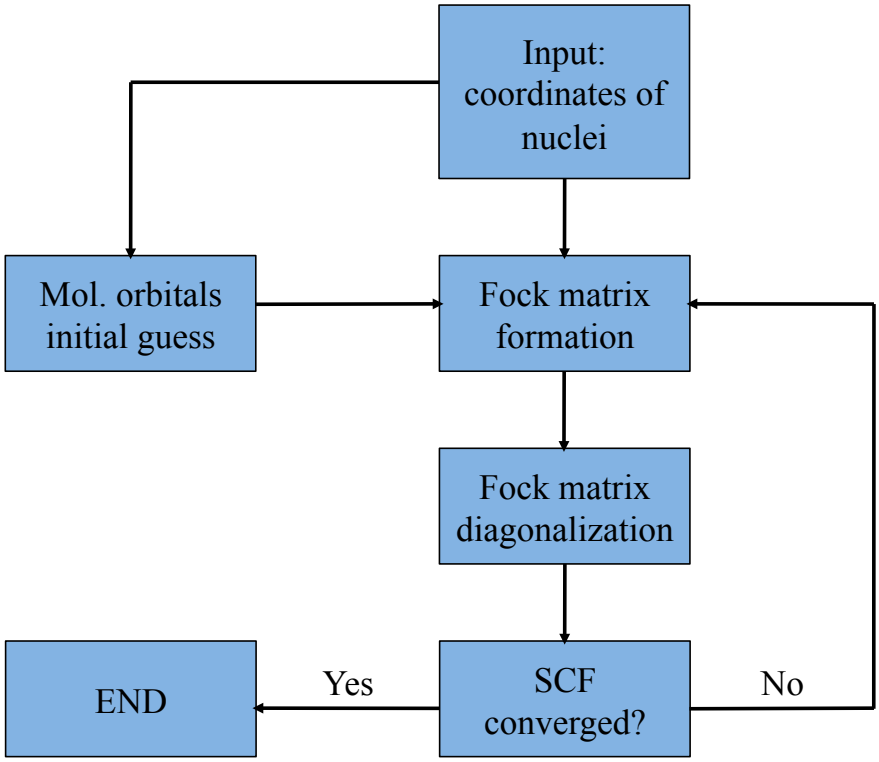

Figure 3.2: Scheme of the self-consistent method.

Semi-empirical methods

As discussed above, some approximations must be introduced to study LH complexes and empirical data are used to simplify and validate the calculation. The combination of these two elements leads to the so-called "semi-empirical" methods. Semi-empirical methods are an improvement of the so-called "empirical" methods, where the two-electron integrals are not explicitly included in the Hamiltonian, since these terms requires the most of the computational cost. Such a scheme was proposed, e. g., by Hückel [93] for π-electrons and improved for all valence electrons by Hoffmann [94]. Different semi-empirical methods exist, and the main difference between them is in the techniques used to approximate the two-electrons integrals. In the CNDO (Complete Neglect of Differential Overlap) [95] based methods for example, all two-electron integrals are replaced by parameters, according to experimental data. The INDO (Intermediate Neglect of Differential Overlap) represents an improvement of the CNDO one: in this method two-center integrals are neglected only for electrons in different atoms. Nevertheless, only organic molecules and those containing atoms from Boron to Fluorine are implemented. The spectroscopic version (INDO/S) is used to calculate excited states, which is, in turn, the quantity of interest in this work. Michael Zerner [96, 97] has implemented an

improved version of the INDO method, the ZINDO (Zerner Intermediate Neglect of Differential Overlap). This method extends the calculation to a wider range of atoms, including even the rare earth elements (and atoms like Mg, fundamental for the site energies calculated in this thesis). The ZINDO/S-CIS (Zerner Intermediate Neglect of Differential Overlap with parameters for Spectroscopic properties together with the configuration interaction scheme using single excitations only [96–98]) version is the semi-empirical method adopted in this work. The lack of a complete treatment of the Hamiltonian is of course the weakness of this method, but the parametrization implemented in ZINDO makes this method quite accurate for the study of LH systems [98]. The ZINDO method is applied in a quantum mechanical/molecular mechanical QM/MM framework, in which the actual pigment of interest is treated as a quantum entity and the atoms surrounding it are treated as classical particles (called "point charges"). The effect of the environmental fluctuations is of key importance in the prediction of the site energies of the pigments [66]. The main advantage of this approach is its efficiency: 5 s are needed for computing a calculation of the site energies in a system composed of a pigment with 50 atoms and an environment with more than 100.000 point charges. This is a common scheme adopted in the field. Two studies only have adopted a quantum description of the whole LH system. This has been done for the LH2 complex of *Rsp. molischianum* [99, 100]. However, due to the computational cost associated to such a study, the calculations are performed for a static configuration and for the BChls only. The fully quantum description of the dynamics of LH systems with environmental effects is still too expensive.

3.1.2 Pigment-Pigment Coupling

To analyze the energy transfer process among pigments, the interaction that causes the de-excitation of the donor (D) molecule and the immediate excitation of the acceptor (A) pigment must be studied. The coupling between D and A is the combination of two terms

$$V_{ij} = V_{io} + V_{Coulomb}. \tag{3.10}$$

At short range ($\sim$5Å), the electron wave functions of the involved pigments overlap: therefore the interaction due to the intermolecular orbitals V_{io} must be considered. This type of energy transfer process involves the exchange of electrons among the pigments and it is known as "Dexter" transfer [101]. The Dexter transfer rate k_D has the form:

$$k_D \approx Je^{-2R/L} \tag{3.11}$$

where J denotes the spectral overlap integral, R the distance between D and A and L the sum of the Van der Waals radii of the involved pigments. Due to its exponential dependence on the distance, it dominates only at short distances. At longer distances, the "Förster" transfer [102] dominates: the pigments are well separated and the coupling is a Coulomb coupling $V_{Coulomb}$ between the transition densities of the involved sites [103]. The transition densities ρ_{10} (Eq. 3.12) are the "virtual" charge distributions that express the way in which the electronic wave functions jump from one state (Ψ_0) to another (Ψ_1) due to the interaction with the electromagnetic field.

$$\rho_{10}(\vec{r_1}) = N \int \Psi_0(x_1, x_2, ..., x_N)\Psi_1^*(x_1', x_2', ..., x_N')dx_2, ..., dx_N dx_2', ..., dx_N' ds_1 \tag{3.12}$$

The analytic expression of ρ_{10} is given in Eq. 3.12, where N denotes the number of electrons of the pigment and the integration goes over all the spatial and spin coordinates x_i of the electrons of the pigment except electron 1 and the spin s_1 of the electron 1. A schematic representation of the two mechanisms is given in Fig. 3.3. The spatial separation between the pigments in the LH systems is

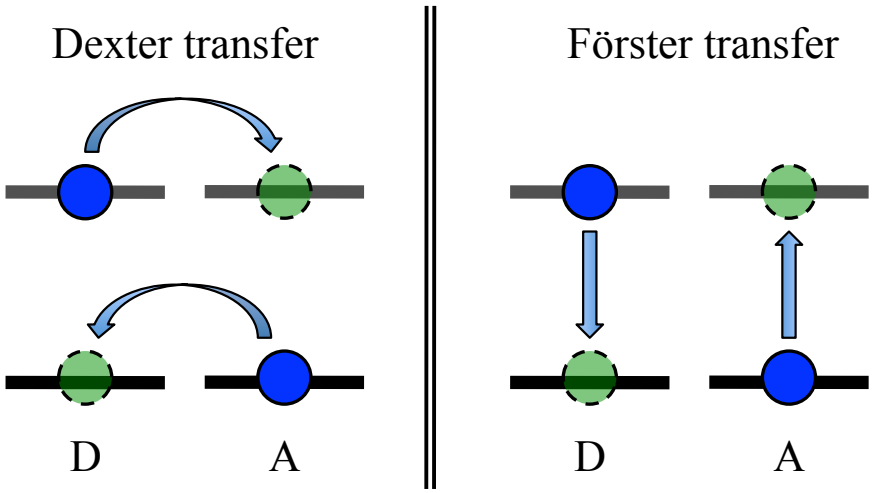

Figure 3.3: Schematic representation of Dexter and Förster transfer processes.

big compared to their size and the Dexter coupling can be neglected. Different approximations have been adopted to calculate the Coulomb coupling between the transition densities of the pigments and the next 3.1.2 and 3.1.2 Sections provide a brief description of these methods.

Point-Dipole Approximation

The point-dipole approximation (PDA) has been introduced by Förster [104]. He showed in 1946 that the exciton energy transfer is a cascade of energy transfer steps from chromophore to chromophore. The process is ruled by Eq. 3.13 where the interaction between transition dipole moments $\vec{\mu}_i$ and $\vec{\mu}_j$ makes each transfer possible. R_{ij} in Eq. 3.13 denotes the distance between the center of masses of the two pigments.

$$V_{ij}^{(PDA)} = \frac{1}{4\pi\epsilon_0}\left[\frac{\vec{\mu}_i \cdot \vec{\mu}_j}{R_{ij}^3} - \frac{3(\vec{\mu}_i \cdot \vec{R}_{ij})(\vec{\mu}_j \cdot \vec{R}_{ij})}{R_{ij}^5}\right] \tag{3.13}$$

A schematic representation of the PDA approximation is given in Fig. 3.4. The transition dipole moment $\vec{\mu}_{10}$ for the transition $0 \rightarrow 1$ is, defined in Eq. 3.14 where $\rho_{10}(r)$ is defined in Eq. 3.12.

$$\vec{\mu}_{10} = \int d\vec{r}\rho_{10}(r)\vec{r} \tag{3.14}$$

The Förster transfer rate k_F is defined as [104]:

$$k_F = \alpha\frac{k^2 Q_D J}{\tau_D n^4}\frac{1}{R^6} \tag{3.15}$$

where $\alpha = \frac{9ln10}{128\pi^5 N_A}$ with N_A denotes the Avogadro's number, k the relative orientation of the donor and the acceptor molecules, Q_D the fluorescence quantum yield of the donor in the absence of the acceptor, J the spectral overlap, τ_D the donor lifetime, n the medium index and R the distance between the pigments (in cm). This approximation is valid as long as the distance between the pigments is large enough compared to their size: due to the averaging process, in fact, the PDA method is not able to take into account the shapes of the molecules. A more accurate approximation is the TrEsp method, introduced in Sec. 3.1.2.

TrEsp Method

The "Transition charges from Electrostatic potential" (TrEsp) method [105] can distinguish the shapes of the involved pigments, an aspect that the PDA approximation missed. In this method, the coupling between the pigments i and j is the Coulomb coupling between the transitions charges q_m^T and q_n^T of all the atoms composing the i and the j pigments, respectively (see Fig. 3.4). It has the form of Eq. 3.16, where f denotes the screening factor and the sum goes over all the m transition charges in pigment i and the n transition charges in pigment j, which

can be calculated by different quantum chemical methods [105, 106]

$$V_{ij}^{(TrEsp)} = \frac{f}{4\pi\epsilon_0} \sum_{m,n} \frac{q_m^T q_n^T}{|\vec{r}_m - \vec{r}_n|}. \tag{3.16}$$

Environmental effects are included in a screening factor f. Several forms of f have been adopted during the years, but the most widely used is the one developed by Scholes and co-workers in 2007 [107]:

$$f = Ae^{-Br_{ij}} + f_0 \tag{3.17}$$

where $A = 2.68, B = 0.27/\mathring{A}, f_0 = 0.54$ and r_{ij} denotes the distance between the pigments (in Å). The TrEsp method is adopted in the calculations present in this thesis.

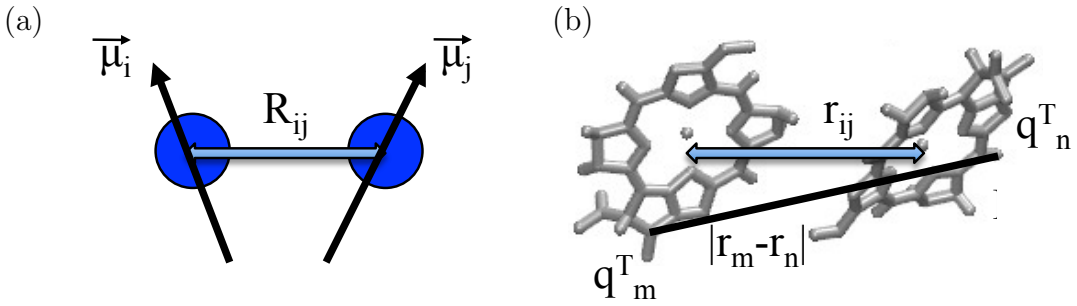

Figure 3.4: Schemes of the methods used to estimate the pigment-pigment interactions: PDA (a) and TrEsp (b) approximations.

3.2 Bath Hamiltonian: H_B

H_B is the Hamiltonian of the bath. It is a common procedure to describe the bath as a set of k harmonic oscillators of masses m_k and frequencies ω_k [108]. The bath Hamiltonian is reported in Eq. 3.18, in which p_k and r_k are the position and momentum operators.

$$H_B = \sum_k \left(\frac{p_k^2}{2m_k} + \frac{m_k \omega_k^2 r_k^2}{2} \right) \tag{3.18}$$

These harmonic oscillators are independently coupled to each pigment of the system.

3.3 System-Bath Interaction Hamiltonian: H_{SB}

H_{SB} is the Hamiltonian that describes the interaction between the system and the bath and it is usually expressed by a linear combination of the system (Φ_n) and bath (r_k) degrees of freedom, as reported in Eq. 3.19, where c_{nk} are the coupling coefficients.

$$H_{SB} = \sum_{n,k} \Phi_n c_{nk} r_k \tag{3.19}$$

The information on the frequency dependence of the coupling between a chromophore i and the bath is expressed by the spectral density function, $J_i(\omega)$ [109]

$$J_i(\omega) = \frac{\pi}{\hbar} \sum_k |c_{i,k}|^2 \delta(\omega - \omega_k). \tag{3.20}$$

Experimentally, the spectral density can be obtained by a fit of optical spectra [110]. Theoretically, the spectral density is obtained as the Fourier transform of the site energy autocorrelation function $C(t)$ [111] as shown in Eq. 3.21.

$$J_i(\omega) = \frac{\beta\omega}{\pi} \int_0^\infty dt C(t) cos(\omega t) \tag{3.21}$$

Previous studies [111, 112] have adopted a different pre-factor ($\frac{2}{\pi\hbar}\tanh(\beta\hbar\omega/2)$), but the expression given in Eq. 3.21 better fits the experimental data [113] and is a consistent high-temperature approximation. $C(t)$ is defined in Eq. 3.22, where N is the number of steps composing the trajectory of the system.

$$C(t_j) = \frac{1}{N-j} \sum_{k=1}^{N-j} \Delta E(t_j + t_k) \Delta E(t_k) \tag{3.22}$$

The most common procedure to simulate the time evolution of the system is based on molecular dynamic (MD) simulations: the dynamics of the ground state of the system is, in fact, evaluated through a MD simulation. The trajectory is then used to obtain the site energies fluctuations through different possible quantum-chemistry calculations. These two techniques are described in the 3.5 and 3.1.1 Sections, respectively. The trajectories are, in general, computed for 100-300 ps and the time steps adopted for the MD simulations are in the range of 2-5 fs, in order to include all the bond stretchings among atoms [114].

3.4 Wave Packet Dynamics

The dynamical properties of the system of interest can be obtained by solving Eq. 3.1. The following approach has been used in this work to calculate the

probability $P_m(t)$ to find the exciton wave packet at a certain time t in a particular pigment m (see Chapters 6 and 7). $\Psi_T(t)$ in Eq. 3.1 is the total wave function and it is assumed to be the product of the system ($\Psi_S(t)$) and bath ($\Psi_B(t)$) wave functions:

$$\Psi_T(t) = \Psi_S(t)\Psi_B(t). \tag{3.23}$$

The combination of Eqs. 3.2 and 3.23, yields

$$i\hbar\frac{\partial|\Psi_S(t)\rangle|\Psi_B(t)\rangle}{\partial t} = (H_S + H_B + H_{SB})\,|\Psi_S(t)\rangle|\Psi_B(t)\rangle. \tag{3.24}$$

Multiplying Eq. 3.24 by $\langle\Psi_S(t)|$ and separately by$\langle\Psi_B(t)|$, and considering that H_S acts only on $|\Psi_S(t)\rangle$ and H_B only on $|\Psi_B(t)\rangle$, it is possible to obtain the two time-dependent Schrödinger equations for the bath (Eq. 3.25) and the system (Eq. 3.26) parts.

$$i\hbar\frac{\partial|\Psi_B(t)\rangle}{\partial t} = H_B|\Psi_B(t)\rangle \tag{3.25}$$

$$i\hbar\frac{\partial|\Psi_S(t)\rangle}{\partial t} = (H_S + \langle\Psi_B(t)|H_{SB}|\Psi_B(t)\rangle)\,|\Psi_S(t)\rangle \tag{3.26}$$

This approximation is valid if the effect of the system on the bath is neglected [85]. In this approximation, the bath is kept in static equilibrium. As standard for perturbative theories, this approximation is valid for weak coupled system-bath configurations [79]. Using Eqs. 3.3 and 3.19, the effective Hamiltonian H_S^{eff} for the system can be defined as Eq. 3.27, where ΔE_m denotes the energy gap fluctuations.

$$H_S^{\text{eff}} = \sum_m (E_m + \Delta E_m(t))\,|m\rangle\langle m| + \sum_{n\neq m} V_{nm}|n\rangle\langle m| \tag{3.27}$$

This leads to the time-dependent Schrödinger equation (Eq. 3.28) for the system.

$$i\hbar\frac{\partial\Psi_S(t)}{\partial t} = H_S^{\text{eff}}\Psi_S(t) \tag{3.28}$$

$\Psi_S(t)$ can be expanded in the basis of the excitonic eigenstates μ of the system Hamiltonian H_S, as reported in Eq. 3.29.

$$|\Psi_S(t)\rangle = \sum_\mu c_\mu(t)|\mu\rangle \tag{3.29}$$

Using Eq. 3.29 into Eq. 3.26, Eq. 3.30 can be obtained.

$$i\hbar\frac{\partial c_\mu(t)}{\partial t} = \epsilon_\mu + \sum_{\mu\nu} J_{\mu\nu}(t)c_\nu(t) \tag{3.30}$$

In Eq. 3.30 $J_{\mu\nu}(t)$ represents the matrix of the system-bath interaction Hamiltonian, and its expression is reported in Eq. 3.31 in which the expansion of the excitonic states in the basis of the local sites $|\mu\rangle = \sum_\mu^m c_m^\mu|m\rangle$ has been used.

$$J_{\mu\nu}(t) = \langle\mu|\langle\Psi_B(t)|H_{SB}|\Psi_B(t)\rangle|\nu\rangle \tag{3.31}$$

Finally, the probability to find the wave packet at site m at time t is given by

$$P_m(t) = |\langle m|\Psi_S\rangle|^2 = |\sum_\mu c_m^\mu c_\mu(t)|^2. \tag{3.32}$$

Eq. 3.32 is used in Chapters 6 and 7 to obtain important quantities, such as the population dynamics, the mean squared displacement of the exciton and the diffusion coefficient.

3.5 Molecular Dynamics

The term "molecular dynamics" identifies the set of computational techniques that, through the integration of the equations of motion, allows the study of the time evolution of a biophysical system at the molecular and atomic level. It can be used to investigate a wide range of biophysical processes such as DNA unzipping, RNA hairpin formation, ion and substrate transport through membrane proteins and protein-complex interaction [115–121]. The time evolution of a generic N particles system is determined by the solution of the set of N Newton's equations:

$$\vec{F}_i(t) = m_i\ddot{\vec{x}}_i(t) = -\nabla_i V(\{\vec{x}_i(t)\}) \quad i = 1, ..., N \tag{3.33}$$

where:

- $\vec{F}_i(t)$ denotes the force-field acting on the i-th particle;
- m_i denotes the mass of the i-th particle;
- $V(\{\vec{x}_i(t)\})$ denotes the potential energy. It depends on the positions $\vec{x}_i(t)$ of the particles composing the system.

The initial configuration of the system, in most of the cases, is set up starting from the X-ray configuration of the system. Once the structure is defined, the potential energy, and, in turn, the force field acting on the system has to be evaluated. $V(\{\vec{x}_i(t)\})$ is, defined as a superposition of a bonded $V_b(\vec{x}_1, ..., \vec{x}_N)$ and non-bonded $V_{nb}(\vec{x}_1, ..., \vec{x}_N)$ potentials:

$$V(\vec{x}_1, ..., \vec{x}_N) = V_b(\vec{x}_1, ..., \vec{x}_N) + V_{nb}(\vec{x}_1, ..., \vec{x}_N) \tag{3.34}$$

These two terms define the interactions among the atoms and the force field is specified by the set of parameters described later in Eqs. 3.35 and 3.36. The parametrization of the force field is a very challenging issue and it requires both the fit of the experimental values and the quantum calculations. The most wide used force fields for biological systems are the CHARMM [122] and AMBER [123] force fields. $V_b(\vec{x}_1, ..., \vec{x}_N)$ and $V_{nb}(\vec{x}_1, ..., \vec{x}_N)$ are respectively defined as:

- $V_b(\vec{x}_1, ..., \vec{x}_N)$ describes the interaction of the atoms with their covalent-bonded neighbor atoms and has the form of Eq. 3.35.

$$V_b(\vec{x}_1, ..., \vec{x}_N) = \sum_{bonds} \frac{k_r}{2}(r - r_0)^2 + \sum_{angles} \frac{k_\vartheta}{2}(\vartheta - \vartheta_0)^2 + \\ + \sum_{dihedrals} \frac{k_\omega}{2}(\omega - \omega_0)^2 + \sum_{torsions} \frac{k_\varphi}{2}(1 + cos(n\varphi - \delta)) \tag{3.35}$$

  $V_b(\vec{x}_1, ..., \vec{x}_N)$ is responsible for the correct bond length between atoms (r_0) and for the correct structure of the molecules given by variations of $\vartheta_0, \omega_0, \delta$. These are the force constants k_α with $\alpha = \{\vartheta_0, \omega_0, \delta\}$.

- $V_{nb}(\vec{x}_1, ..., \vec{x}_N)$ takes into account electrostatic and Van der Waals interactions and it is expressed by Eq. 3.36, where q_i and q_j denote the charges of the i and the j particles, r_{ij} the distance between them, ε_0 the vacuum permittivity and σ_{ij} and ε_{ij} the *Lennard-Jones* parameters.

$$V_{nb}(\vec{x}_1, ..., \vec{x}_N) = \sum_{j=1}^{N} \sum_{i<j}^{N} \left(\frac{q_i q_j}{4\pi\varepsilon_0 r_{ij}} + 4\varepsilon_{ij} \left[\left(\frac{\sigma_{ij}}{r_{ij}} \right)^{12} - \left(\frac{\sigma_{ij}}{r_{ij}} \right)^{6} \right] \right) \tag{3.36}$$

  The Van der Waals interaction, modeled by the Lennard-Jones potential, is a balance between two terms: a short-range repulsive force between the electrons of the molecules and a long-range attractive force arising from the instantaneous dipoles induced by the fluctuations of the electron clouds.

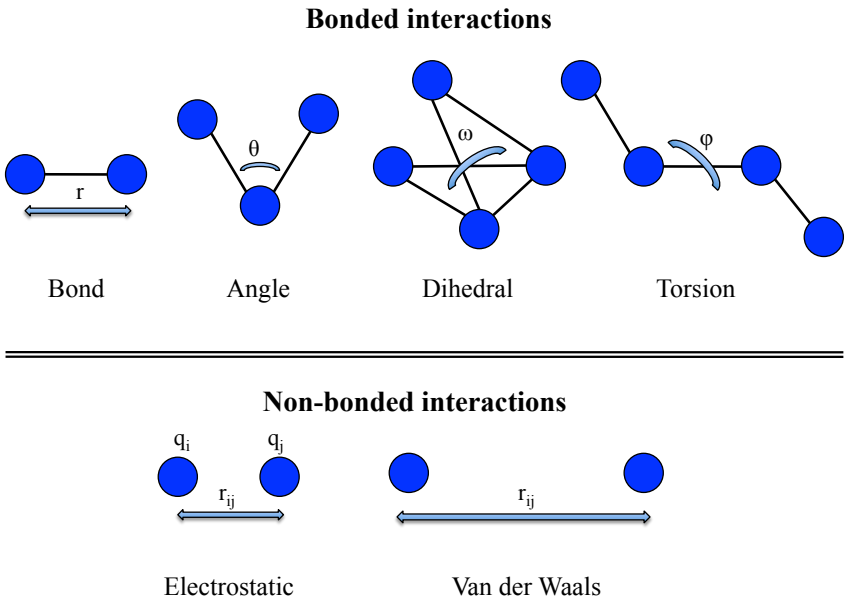

Figure 3.5: Schematic representation of the bonded and non-bonded potentials.

A schematic representation of the bonded and non-bonded interactions is given in Fig. 3.5. The time scales in biological systems go from femtoseconds (bond vibrations) to milliseconds and longer for protein folding processes, while usual MD simulations time scales are in the range of several (10 to 100) nanoseconds for large systems and up to tens of microseconds for small ones, due to the computational cost of the simulations [115]. MD modeling has the limitation to be a pure ground-state method; this means that electronic properties like excited states or energy and electron transfers can not be modeled. In particular, for what concerns the study of LH systems, a combination of MD simulations, electronic structure studies and dynamics methods is needed in order to achieve a complete treatment of these systems. This is schematic represented in Fig. 3.6, where it is shown that the use of both MD and quantum chemistry methods is fundamental to derive dynamic and optical properties of the system under study. Such properties can be extracted by solving the time-dependent Hamiltonian or by following a density-matrix propagation approach. The first method has been used in this work.

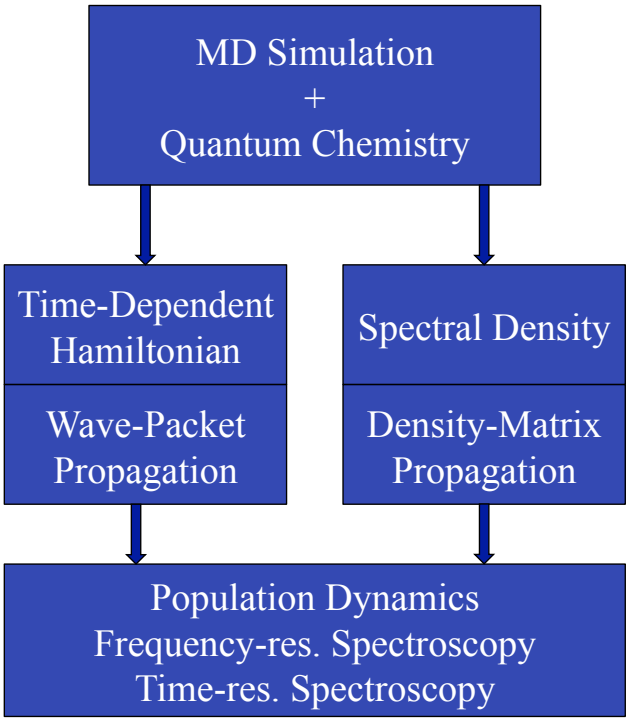

Figure 3.6: Schematic representation of the multi-scale approach used to study LH systems.

3.6 Dephasing Function and Time

An important quantity in this thesis work (see Chapters 4 and 5) is the so-called "dephasing time" τ_D, which describes the decoherence rate of a system due to the interaction with the fluctuation of the environment [124]. In this section the theoretical background will be presented. The results presented in Chapters 4 and 5 have been analyzed within the framework of the generalized Kubo's stochastic line shape theory, firstly developed to analyze the broadening in condensed phase spectroscopy [125]. The standard Kubo's theory assumes that due to a time-dependent perturbation, a generic property $A(t)$ of a certain system varies according to the simple equation:

$$\frac{dA(t)}{dt} = i\omega(t)A(t) \tag{3.37}$$

where $\omega(t)$ denotes the frequency of the system. A random process is assumed to modulate the frequency such that:

$$\omega(t) = \omega_0 + \delta\omega(t) \tag{3.38}$$

where $\omega_0 = \langle\omega(t)\rangle = \lim_{T\to\infty} \frac{1}{T}\int_0^T \omega(s)ds$ and $\langle\delta\omega(t)\rangle = 0$. By integrating Eq. 3.38, one obtains the time evolution of $A(t)$:

$$A(t) = A(0)\exp\left[i\int_0^t \omega(s)ds\right] = A(0)e^{i\omega_0 t}\exp\left[i\int_0^t \delta\omega(s)ds\right] \tag{3.39}$$

. Now, multiplying Eq. 3.39 by $A^*(0)$ and taking the ensemble average, it is possible to get the autocorrelation function of the $A(t)$ quantity:

$$C(t) = \langle A(t)A(0)\rangle = |A(0)|^2 e^{i\omega_0 t}D(t) \tag{3.40}$$

in which $D(t) = \langle\exp\left[i\int_0^t \delta\omega(s)ds\right]\rangle$ denotes the so-called Dephasing function. $D(t)$ represents the Fourier transform of the lineshape function $I(\omega)$ and can be expanded in a cumulant series of averages, as reported below in Eq. 3.45. The dephasing function is of key importance since it is later used to define the dephasing time. In this thesis, this theory have been applied to develop an analytic procedure to relate the energy gap fluctuation of a pigment (or of a whole system) to its dephasing time [126]. The fluctuation ΔE of the energy gap is the starting point of this analysis and it is defined in Eq. 3.41 as the standard deviation along the trajectory:

$$\langle\Delta E^2\rangle^{1/2} = \sqrt{\langle\Delta E^2\rangle - \langle\Delta E\rangle^2} \tag{3.41}$$

where $\Delta E = E(t) - \langle E\rangle$. As already mentioned, in Kubo's theory, ΔE in Eq. 3.41 is described as a Gaussian random process with mean value zero. Furthermore,

in the generalized Kubo's theory, the autocorrelation function $C(t)$ (Eq. 3.22) is assumed to decay exponentially with two different time scales, $\tau_{c,1}$ and $\tau_{c,2}$, known also as correlation times, as it can be seen in Eq. 3.42 where $\alpha_1 + \alpha_2 = 1$ are the normalization coefficients.

$$C(t) = \langle \Delta E^2 \rangle \left(\alpha_1 \exp(-t/\tau_{c,1}) + \alpha_2 \exp(-t/\tau_{c,2}) \right)) \tag{3.42}$$

The correlation time τ_c is in general defined as

$$\tau_c = \frac{1}{\langle \Delta E^2 \rangle} \int_0^\infty C(t) dt. \tag{3.43}$$

In Kubo's model the key quantity is the line shape $I(\omega)$, defined as

$$I(\omega) = \frac{1}{\pi} \int_0^\infty dt cos(\omega t) \exp[-D(t)]. \tag{3.44}$$

In Eq. 5.6 $D(t) \equiv \exp[-g(t)]$ is the pure-dephasing function, in which $g(t)$ denotes the line shape function [127]. Using the cumulant approximation [78], $D(t)$ can be written as:

$$D(t) = \exp\left[-\frac{1}{\hbar^2} \int_0^\infty d\tau (t - \tau) C(\tau) \right]. \tag{3.45}$$

Using the definition of C(t) given in Eq. 3.42, Eq. 3.45 becomes

$$g(t) = \frac{\langle \Delta E^2 \rangle}{\hbar^2} \sum_{i=1}^{2} \alpha_i \tau_{c,i}^2 \left[\exp(-t/\tau_{c,i}) + t/\tau_{c,i} - 1 \right]. \tag{3.46}$$

An additional approximation needs to be introduced at this point: the fluctuations in the systems are the sum of only fast and slow oscillations. Then $g(t)$ can be approximated as [128]

$$g(t) = \frac{\langle \Delta E^2 \rangle}{\hbar^2} \left[\alpha_1 \tau_{c,1} t + \alpha_2 t^2/2 \right]. \tag{3.47}$$

The expression in Eq. 3.47 can be used to analytically integrate $D(t)$ to obtain the dephasing time τ_D

$$\tau_D = \frac{2}{\sqrt{\pi}} \int_0^\infty D(t) dt = \sqrt{\frac{2\hbar^2}{\langle \Delta E^2 \rangle \alpha_2}} e^{-A\langle \Delta E^2 \rangle} \text{erfc}\left(\sqrt{A \langle \Delta E^2 \rangle} \right). \tag{3.48}$$

where $A = \frac{\tau_1^2 \alpha_1^2}{2\hbar^2 \alpha_2}$. Eq. 3.48 relates the dephasing time to the energy gap fluctuation. This functional behavior is universal and valid independent from the method used in the simulations [126]. For a detailed discussion of this method and its application, see Chapters 4 and 5.

Chapter 4

Relation Between Dephasing Time and Energy Gap Fluctuations in Biomolecular Systems

Excitation energy and charge transfer are fundamental processes in biological systems. Due to their quantum nature, the effect of dephasing on these processes is of interest especially when trying to understand their efficiency. Moreover, recent experiments have shown quantum coherences in such systems. As a first step in a better understanding, we studied the relationship between dephasing time and energy gap fluctuations of the individual molecular subunits. A larger set of molecular simulations has been investigated to shed light on this dependence. This set includes bacterio-chlorophylls in Fenna-Matthews-Olson complexes, the PE545 aggregate, the LH2 complexes, DNA, photolyase, and cryptochromes. For the individual molecular subunits of these aggregates it has been confirmed quantitatively that an inverse proportionality exists between dephasing time and average gap energy fluctuation. For entire complexes including the respective inter-molecular couplings such a relation, however, still needs to be verified.

Reprinted under the ACS AuthorChoice license from the article by M. I. Mallus, M. Aghtar, S. Chandrasekaran, G. Lüdemann, M. Elstner and U. Kleinekathöfer "Relation Between Dephasing Time and Energy Gap Fluctuations in Biomolecular Systems" *J. Phys. Chem. Lett.*, **2016**, 7, 1102-1108. **DOI**: 10.1021/acs.jpclett.6b00134. Copyright ©2016 ACS Publications

4.1 Introduction

In biomolecular systems, the transfer of excitation energy and charges is ubiquitous. Quantum effects do play a major role in these processes and therefore also the amount of dephasing present in these system is of quite some interest. It has been shown that coherence effects are important in charge [129, 130] and excitation energy transfer [131,132]. Even in liquid water vibrational quantum coherence plays an interesting role [133]. Moreover, even in single pigments dephasing is of key importance as shown by two-dimensional electronic spectroscopy [134, 135]. In all these systems the environment has two effects on the respective quantum (sub)system of interest: quantum coherences are washed out and relaxation to the thermal equilibrium is enforced.

Coherences are usually associated with off-diagonal elements of density matrices and dephasing with the decrease of the coherences [79]. For electronic two-level systems with nuclear degrees of freedom, this dephasing is proportional to the so-called nuclear overlap/phase function [136–138]. Its absolute value is usually termed dephasing or decoherence function. This function is in turn used to define the pure dephasing time [139, 140]. Up to an oscillatory phase factor, the dephasing function describes the time-dependent overlap of two initially identical nuclear wave packets evolving on two separate electronic states. Often these states are the ground and an excited state of the system of interest but, for example, can also be a neutral and ionized state. Initially the overlap of the wave packets on the two surfaces equals unity but due to the different forces acting on the nuclei on the two electronic surfaces, the overlap decreases with time. The probability of a revival is negligible due to the large number of atoms usually involved. In the Fermi Golden rule and the high-temperature approximation, the dephasing function has a purely Gaussian form [139]. In another approximation, a purely exponential decay for the dephasing function was obtained [141]. A comparison of these approximate functional dependencies to numerical results from molecular simulations is reported below.

The other important function in this study is the energy-energy autocorrelation function. By fitting its short time behavior, for example, one can obtain the respective correlation time. Sometimes a proportionality between correlation and dephasing times is assumed [142], while in a recent study the independence between the two time scales for some test systems was shown [75]. Moreover, these authors reported a surprising finding concerning their simulations of organic heterodimer molecules in different solvents. Plotting the pure dephasing times versus the corresponding average energy gap fluctuations resulted in a clear func-

tional relationship between the two quantities. Furthermore, the dephasing time was found to be independent of the energy-energy autocorrelation time. It seems intuitive to some extent that a larger electron-nuclear correlation time leads to an enhanced dephasing time. That this assumption is not true, is clear latest since the study by Akimov and Prezhdo [75].

In the present study we are analyzing the relationship between dephasing time and the average energy gap fluctuation for a much larger set of simulations. This data set is based on sequential combinations of MD simulations and quantum chemistry calculations for the light-harvesting system II (LH2) [112] the Fenna-Matthews-Olson (FMO) trimer [143, 144], the PE545 system [66], DNA [145], photolyase [146], and cryptochrome [147]. Due to the size of some of these systems we do restrict ourselves to the analysis of the dephasing behavior for the individual subunits of the respective system, e.g., individual BChl *a* molecules in light-harvesting systems. As detailed below, the functional form found for these systems is different from the one found earlier by Akimov and Prezhdo [75]. Nevertheless, a clear functional dependence between the dephasing time and the electron-nuclear correlation time is found. This common behavior is traced back to common features of the energy-energy autocorrelation function.

4.2 Background on Dephasing Function and Time

For a better interpretation of our numerical results on molecular systems, we will analyze them within a generalized version of the stochastic line shape theory by Kubo [125] which was developed to describe homogeneous and inhomogeneous broadening in condensed phase spectroscopy. The time-dependent fluctuation of the energy gap is the key quantity in this expression. For the light-harvesting systems, we are concerned with the gap between ground and (first) excited state while for charge transfer complexes the ionization energy, i,e., the energy difference between ionized and neutral state, is of interest. For simplicity we refrain here from adding a site subscripts to all quantities like energy gap and correlation function since it should be clear that these always refer to single chromophore. So, for example, the energy gap will simply be denoted as $\Delta E = E - \langle E \rangle$. The average fluctuation along a trajectory can be characterized by

$$\langle \Delta E^2 \rangle^{1/2} = \sqrt{\langle \Delta E^2 \rangle - \langle \Delta E \rangle^2} \; . \tag{4.1}$$

In Kubo's lineshape theory the energy gap fluctuation is described by a Gaussian random process with mean value zero. Moreover, its autocorrelation function $C(t)$ is assumed to decay exponentially. Here we employ a generalized Kubo model with

two different time scales [148]. In this model the unnormalized correlation function $C(t)$ consists of two parts with normalized prefactors α_1 and α_2, i.e., $\alpha_1 + \alpha_2 = 1$, as well as correlation times $\tau_{c,1}$ and $\tau_{c,2}$

$$C(t) = \langle \Delta E^2 \rangle (\alpha_1 \exp(-t/\tau_{c,1}) + \alpha_2 \exp(-t/\tau_{c,2})) \ . \tag{4.2}$$

The function $C(t)$ describes the correlation between the different electronic states which are functions of the time-dependent nuclear coordinates. Therefore, this function is also called the electron-nuclear correlation function. For the example of a light-harvesting 2 complex we have shown earlier that the correlation function can reasonably be described by two exponential functions while the addition of damped oscillations makes a almost perfect fit possible [112]. Furthermore, from Eq. (4.2) one can deduce a general definition of the correlation time τ_c given by [149]

$$\tau_c = \frac{1}{\langle \Delta E^2 \rangle} \int_0^\infty C(t) dt \ . \tag{4.3}$$

For vanishing α_1 or α_2 in Eq. (4.2), this definition of the correlation time reproduces the respective correlation time. In Kubo's stochastic model, the line shape is defined as

$$I(\omega) = \frac{1}{\pi} \int_0^\infty dt \cos(\omega t) \exp[-D(t)] \ . \tag{4.4}$$

In this expression $D(t) \equiv \exp(-g(t))$ denotes the pure-dephasing function and can be expressed through the lineshape function $g(t)$ [127]. Within the cumulant approximation [78] the dephasing function is given by

$$D(t) \equiv \exp(-g(t)) = \exp\left[-\frac{1}{\hbar^2} \int_0^t d\tau (t-\tau) \langle \Delta E(\tau) \Delta E(0) \rangle \right] \ . \tag{4.5}$$

In addition to the simplified structure of the expression, the cumulant version of the dephasing function converges numerically much better than the original expression [150]. Moreover, this expression indicates that the dephasing is faster for larger correlation functions. As already discussed above, the dephasing function describes the decoherence rate of a system due to the influence of the environmental fluctuations and is directly connected to the off-diagonal matrix elements of the respective density matrix [136–138]. The dephasing function is a key quantity for the present study, e.g., since it is used to define the dephasing time τ_D below. Using a sum of two exponentials as correlation function as given in Eq. (4.2), the lineshape function reads

$$g(t) = \frac{\langle \Delta E^2 \rangle}{\hbar^2} \sum_{i=1}^{2} \alpha_i \tau_{c,i}^2 \left(\exp(-t/\tau_{c,i}) + t/\tau_{c,i} - 1 \right) \ . \tag{4.6}$$

Two limits for purely exponential correlation functions with correlation time τ_c are usually considered [127]. On the one hand, one can assume short correlation times $\tau_{c,1}$, i.e., $t \gg \tau_{c,1}$ corresponding to the homogeneus case. On the other hand one obtains the inhomogeneus case in which the absorption lineshape reflects a static distribution of frequencies in the limit of long correlation times $\tau_{c,2}$, i.e., $t \ll \tau_{c,2}$. Assuming that the fluctuations in the system under consideration includes slow and fast fluctuations at the same time, the line shape function can be approximated by [148]

$$g(t) = \frac{\langle \Delta E^2 \rangle}{\hbar^2} \left(\alpha_1 \tau_{c,1} t + \alpha_2 t^2/2 \right) \ . \tag{4.7}$$

As defined above, the respective dephasing function is given by $D(t) = \exp(-g(t))$ while the dephasing time τ_D can now be defined as

$$\tau_D = \frac{2}{\sqrt{\pi}} \int_0^\infty D(t) dt \ . \tag{4.8}$$

This definition is similar, e.g., to the definition of the correlation time as an integral over the normalized energy autocorrelation function [138]. The prefactor is chosen such that the standard definition of a dephasing time for a Gaussian dephasing function is reproduced [75] (see below). Calculating the dephasing time τ_D for the lineshape function given in Eq. (4.7) leads to the following expression

$$\tau_D = \sqrt{\frac{2\hbar^2}{\langle \Delta E^2 \rangle \alpha_2}} e^{-A\langle \Delta E^2 \rangle} \operatorname{erfc}(\sqrt{A \langle \Delta E^2 \rangle}) \ . \tag{4.9}$$

In this equation $\operatorname{erfc}(x)$ denotes the complementary error function and the constant A is given by

$$A = \frac{\tau_1^2}{2\hbar^2} \frac{\alpha_1^2}{\alpha_2} \ . \tag{4.10}$$

In the limit of vanishing α_1, i.e., a single-exponential correlation function with large correlation time, the Gaussian limit for the dephasing time is recovered [75]

$$\tau_{D,G} = \frac{B}{\sqrt{\langle \Delta E^2 \rangle}} \ . \tag{4.11}$$

According to Kubo's theory [125] the constant B has the value $B = \sqrt{2}\hbar$. However, Akimov and Prezhdo [75] argued that this value needs to be slightly enlarged when not employing the cumulant expansion of the dephasing function leading to $B = \sqrt{12/5}\hbar$. Moreover, in the same study an even larger value of $B = 1.82\hbar$ was obtained by fitting to their numerical data. Below we show that this latter value leads to an excellent agreement with our numerical data for charge transfer systems as well.

Number	System	Sites	Force field	Energy gap	Ref.
1	FMO complex, *C. tepidum*	24	CHARMM	ZINDO	143
2	FMO complex, *P. aestuarii*	24	CHARMM	ZINDO	144
3	FMO complex, *P. aestuarii*	24	CHARMM	TDDFT	144
4	FMO Complex, *P. aestuarii*	24	AMBER	ZINDO	144
5	LH2 complex, *R. molischianum*	24	CHARMM	ZINDO	112
6	LH2 complex, *R. acidophila*	27	CHARMM	ZINDO	151
7	PE545 complex	8	AMBER	ZINDO	66
8	DNA	7	AMBER	DFTB	145
9	DNA Photolyase, *E. coli*	3	AMBER	DFTB	146
10	Cryptochrome	3	AMBER	DFTB	147

Table 4.1: List of the eight different systems investigated in this study together with some details and the corresponding references. Moreover, the FMO complex from one bacterium has been calculated with two additional combinations of force field and quantum chemistry approach.

Moreover, in the limit of vanishing α_2, i.e., a purely exponential correlation function with a short correlation time, the exponential limit for the dephasing time is obtained

$$\tau_{D,E} = \frac{2\hbar^2}{\sqrt{\pi}\tau_{c,1}\langle\Delta E^2\rangle} \ . \tag{4.12}$$

In this exponential case the dephasing time is inversely proportional to the correlation time $\tau_{c,1}$ while in the former Gaussian case the dephasing time, Eq. (4.11), is completely independent of the respective correlation time $\tau_{c,2}$. This independence has been discussed earlier in Ref. 75 for a purely exponential correlation function. At this point we would like to stress that the independence of $\tau_{D,G}$ from the long correlation time $\tau_{c,2}$ is also reflected in our generalized results, Eq. (4.9), since the value of A is independent of this quantity.

4.3 Results Based on Molecular Simulations

The dephasing times of heterodimers in simple fluids were at the focus of the investigation by Akimov and Prezhdo [75]. In the present study, simulations on a variety of systems are being analyzed though we focus on the dephasing of the individual monomers. All results are based on a MD simulation and subsequent single-point quantum chemistry calculations either for the lowest excitation energy gap in the case of the exciton transfer systems or for the ionization energy

in case of charge transfer systems. For the MD simulations either the CHARMM or AMBER force fields have been employed while the quantum chemistry calculations were performed using the ZINDO, TDDFT and DFTB approaches. The quantum chemistry predictions have all been performed as mixed QM/MM calculations since the effect of the environmental fluctiations on the electronic structure determinations is of key importance as, for example, shown in Ref. 66. Table 5.1 lists the simulations together with the corresponding references in which all the details concerning the calculations are reported. Here we refrain from repeating all these simulation details since the purpose of the present study is to analyze these data in a way different from that done before.

The FMO and LH2 systems contain BChl *a* molecules as their functional subunits. Though the average energy gap fluctuations $\sqrt{\langle \Delta E^2 \rangle}$ of the individual pigments vary by about a factor of two (see below) the normalized correlation functions $\tilde{C}(t)$ show a large degree of similarity. As shown in Fig. 4.1, these functions start with a sharp drop on a 5 fs time scale followed by a much slower decay combined with a fast oscillation with a period of around 20 fs. Certainly we cannot extract this time scale accurately from this plot since the time step in these simulations was 5 fs, i.e., our analysis of this data is restricted by this time step. The fast oscillations in case of the BChls are connected to modes involving C=C and C=O double bond vibrations [114]. The interesting part is to see that the normalized correlation functions do show very similar forms despite the different environments into which they are embedded. This finding strongly indicated that the normalized correlation function is to a large degree determined by the chemical structure of the investigated entity and not so much by its surroundings.

The PE545 complex contains bilin molecules instead of bacterio-chlorophylls, i.e., six phycoerythrobilins (PEBs) and two dihydrobiliverdins (DBVs) [66]. As in the case of the BChl molecules, the normalized autocorrelation functions for the bilin molecules show a fast intial decay on a 5 fs time scale and fast oscillations with a period of around 20 fs. This finding is not surprising since the bilins do have quite some chemical similarity to BChl molecules. At the same time it is also clearly visible that the correlation functions of the two DBVs show larger oscillations around a slightly shifted curve compared to the PEBs. Four of the PEBs behave very similar while two of them show somewhat larger deviations. The enhanced resolution of the curves for the bilins compared to the BChl molecules in Fig. 4.1 is due to the shorter time step in the underlying MD simulations of 2 fs compared to 5 fs.

In a next step we look at the dephasing functions as defined in Eq. (4.5). The integrals over the correlation functions in this expression need to be performed

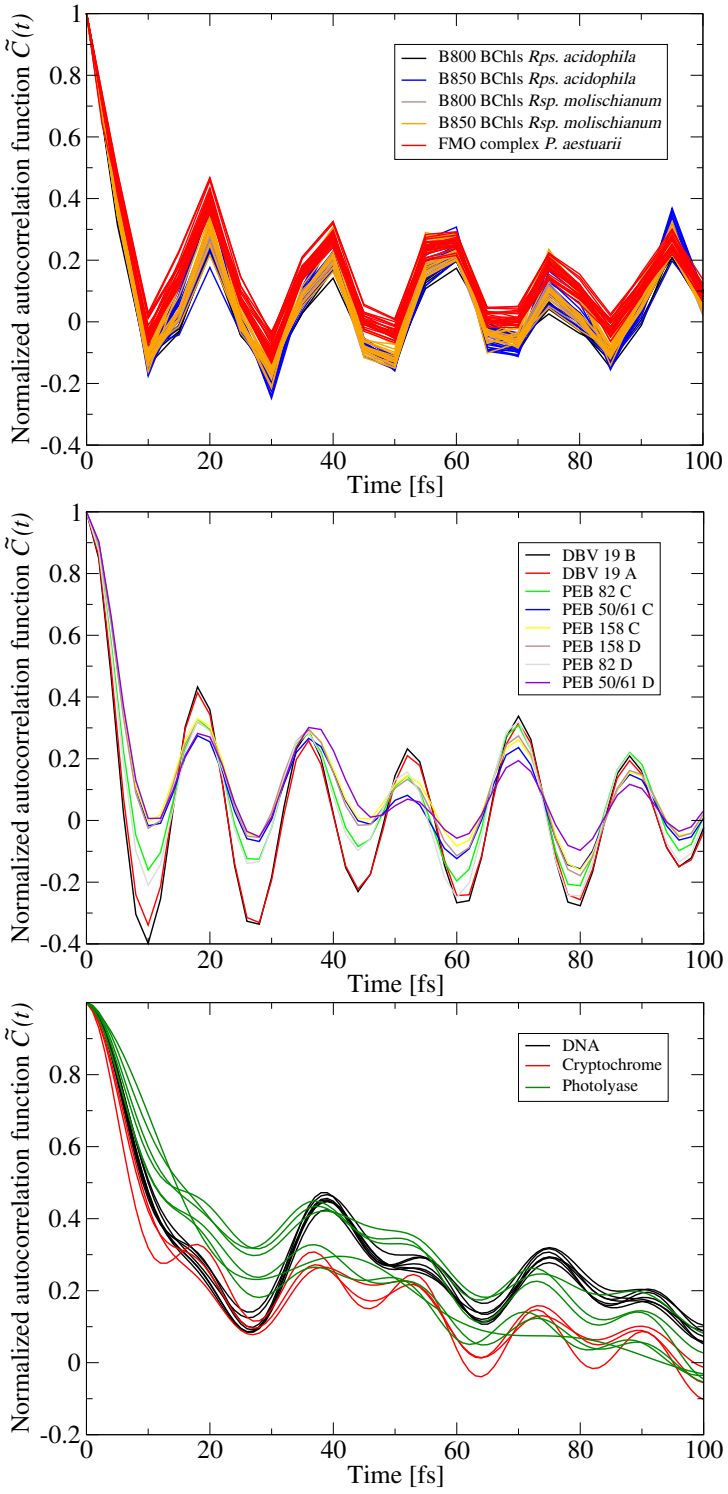

Figure 4.1: Normalized autocorrelation functions for BChls *a* (top), bilins (middle) and charge-able subunits (bottom) in different protein environments.

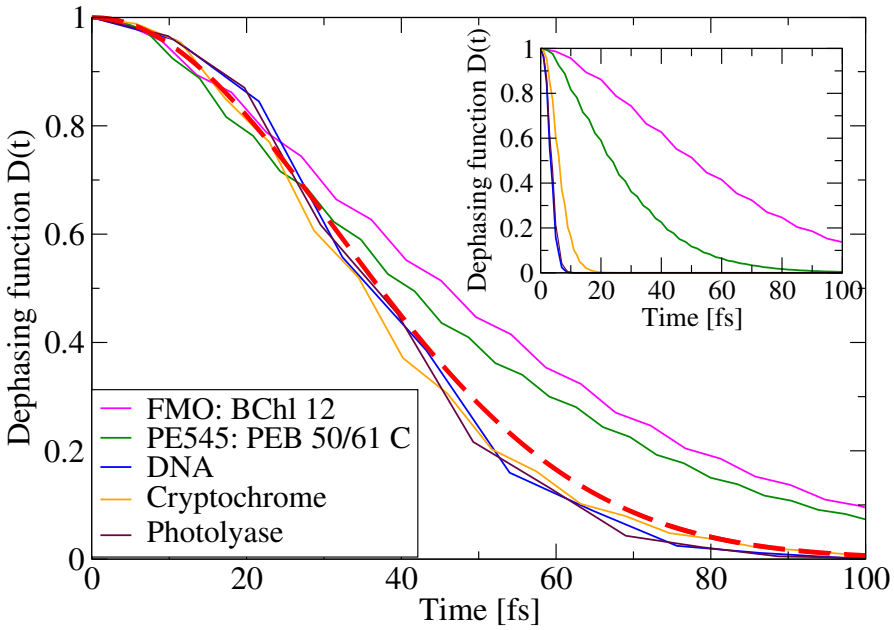

Figure 4.2: Different behaviour of some example dephasing functions: In the inset the unscaled dephasing functions are shown while in the main panel the functions are scaled to have the same short time behavior. The red dashed line represents a perfect Gaussian from.

numerically. Here we want to note once more that due the integration over the correlation function its oscillatory features do not play a key role in the results below. Thus, the approximation of the correlation functions by a sum of two exponentially decaying functions as described above leads qualitatively to the same results. For some of the studied subunits the dephasing functions are shown in the inset of Fig. 4.2. In the main part of the figure, we have rescaled the dephasing functions of the different systems such that they overlap at short times. Due to the definition of the dephasing function, Eq. (4.5), all curves show a Gaussian behavior at very short times. For larger times, however, the curves for the examples from photosynthetic complexes, i.e., FMO and PE454, start to deviate from the Gaussian behavior while the curves corresponding to the charges transfer systems DNA, cryptochrome and photolyase do behave quite Gaussian. Please note, that the dephasing functions of these charge transfer systems decay much faster than those for the light-harvesting systems due to their larger fluctuations, i.e., stronger coupling to the environment. It is interesting to note, however, that for the excitonic heterodimers in simple fluids, Akimov and Prezhdo [75] found a purely Gaussian behavior.

Based on Eq. (4.8) the dephasing time can be determined by numerical in-

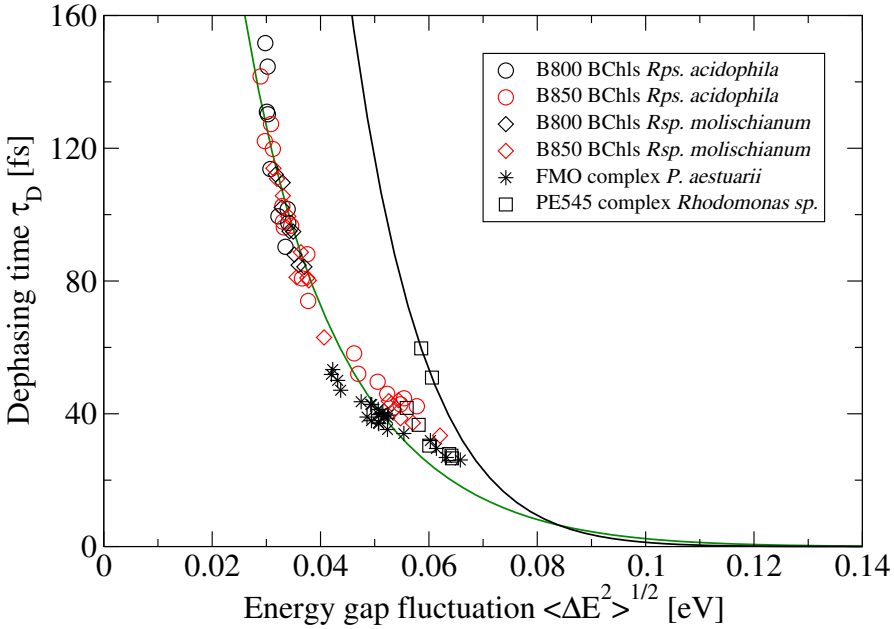

Figure 4.3: Dependence of the dephasing times on the electronic energy gap fluctuations for various light-harvesting systems. The green solid line is based on an almost exponential case with $A = 121$ and $\alpha_2 = 0.02$ while the black curve depicts an purely exponential case with $A = 225$ and $\alpha_2 = 0.0007$.

tegration from the corresponding dephasing function. Figure 4.3 depicts these dephasing times for individual pigments of light-harvesting complexes as a function of the fluctuation of the energy gap function, $\langle \Delta E^2 \rangle^{1/2}$. All pigments of the respective complex are shown separately. It is very surprising to see that the results for almost all pigments lie on one curve. To better understand this numerical data we employed Eq. (4.9) with A and α_2 as fitting function for the bulk of the data, i.e., the data points for FMO and LH2 rings from *Rps. acidophila*. Thus, although the data from the LH2 rings of *Rsp. molischianum* were not included their data points are very close to the fitted curve. The fit resulted in values of $A = 121$ and $\alpha_2 = 0.02$. In addition, included in this plot is a line for an purely exponential case with $\alpha_2 = 0.0007$ and an A value of $A = 225$. This curve is chosen to fit the data for the two points based on the exponential form which belong to the DBV bilins from the PE545 complex. These two pigments indeed showed an exponential behavior of the dephasing function. The values of the parameters A and α_2 were obtained by fitting the numerical data points. Alternatively one could fit the corresponding autocorrelation functions to a sum of two exponentials, Eq. (4.2), and thus obtain the parameters α_1, α_2, $\tau_{c,1}$, and $\tau_{c,2}$. With the help of Eq. (5.10) the value of A can be determined subsequently. The values of A obtained through

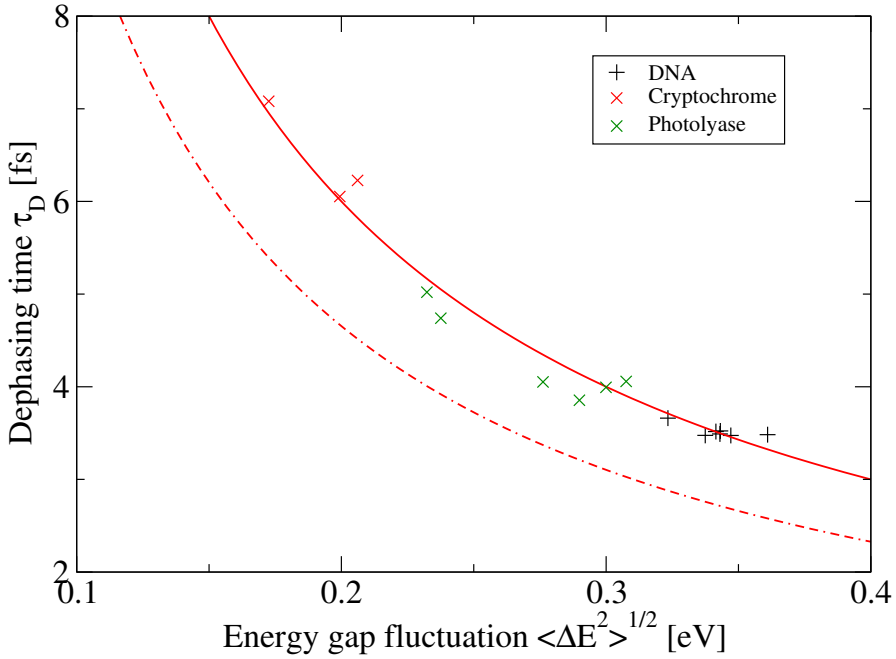

Figure 4.4: Dependence of the dephasing times on the electronic energy gap fluctuations for charge transfer systems with purely Gaussian dephasing functions . The relation in Eq. (4.11) is used with the values $B = \sqrt{2}\hbar$ for the dashed line and $B = 1.82\hbar$ for the solid curve.

the latter procedure differs from the value obtained through direct fitting roughly by a factor of four. It is not surprising that one does not obtain exactly the same value since the correlation functions from the molecular simulations do contain the strong fast oscillations which are neglected in the sum of two purely exponential functions. During the integration process to obtain the dephasing function most of these oscillatory features are averaged out but not completely. Moreover, to obtain the lineshape function in Eq. (4.7), we did further assume that the energy gap fluctuations contain very fast and slow components but none in the intermediate regime. Keeping these approximations in mind, it is rewarding to see that the values for A only differ by a factor of about four indicating that the theory developed in the previous section does capture the main ingredients of the process.

In a next step we look at the dephasing in individual subunits of charge transfer systems. One system consists of a double-stranded DNA heptamer with base sequence poly(dG)-poly(dC) in water [145]. Therefore, seven subunits of this system will be studied. The second system is the DNA photolyase [146]. Hole transfer events in this aggregate are key steps in the photoactivation process and five tryptophans in this compound have been studied. Moreover, three tryptophans in the

structurally very similar cryptochrome complex were included in the analysis [146]. The normalized energy gap autocorrelation functions of these systems are shown in Fig. 4.1 as well. The oscillations in this graph are not as pronounced as those of the previously discussed light-harvesting systems. Furthermore, the initial decay is slower. More importantly, however, is the fact that for the charge transfer systems the energy gap fluctuations are much larger than those for the pigments of the light-harvesting systems. A change in the charge state of a molecular subunit couples much stronger to movements of charges in the environment than a rotation of a dipole moment in case of a chromophore excitation. Therefore, the corresponding points in the diagram of dephasing times versus fluctuation of the energy gap function, $\langle \Delta E^2 \rangle^{1/2}$, lie in a rather different part of the parameter space. This part of the diagram is shown in Fig. 4.4 where all subunits of the respective charge transfer systems are depicted separately. Again it is surprising that the results for subunits of the different charge transfer systems lie on one curve. Shown in the graph is also the expression for the dephasing time in the Gaussian limit since the dephasing function in Fig. 4.2 proofed to be of Gaussian form. The equation for the dephasing time in this case, Eq. (4.11), contains the proportionality factor B. In Fig. 4.4 two values for B are used. The factor resulting from the original Kubo theory $B = \sqrt{2}\hbar$ already leads to a reasonable agreement with the numerical data points though an offset can be observed. Employing instead the value $B = 1.82\hbar$ as obtained by Akimov and Prezhdo [75] from their numerical data, the agreement between analytic curve and the data points for realistic systems do agree very well again supporting the overall theory employed in the present study.

One question is now how much the obtained results do depend on the level of theory which was used to obtain the numerical data points for the realistic systems in the present study. To this end, we employed two different MD force fields and two different quantum chemistry approaches. Recently we have performed a comparison for the FMO complex using the CHARMM or AMBER force fields, the ZINDO/S-CIS and TDDFT approaches for calculating the energy gaps and using different bacteria [144]. The results for dephasing time versus energy gap fluctuation for several of these combinations are shown in Fig. 4.5. It is clearly visible that there is quite a spread in the results. These results, however, all lie on or close to the same curve which we already identified in Fig. 4.4. These results shows that the present finding does not strongly depend on the employed MD or quantum chemistry method but might, however, be influenced by our sequential scheme of performing the energy gap calculations on a pre-determined MD trajectory. The effects of polarization in the QM/MM approach [152, 153] or of *ab initio* MD [154] need to be investigated as well. Furthermore, this result sup-

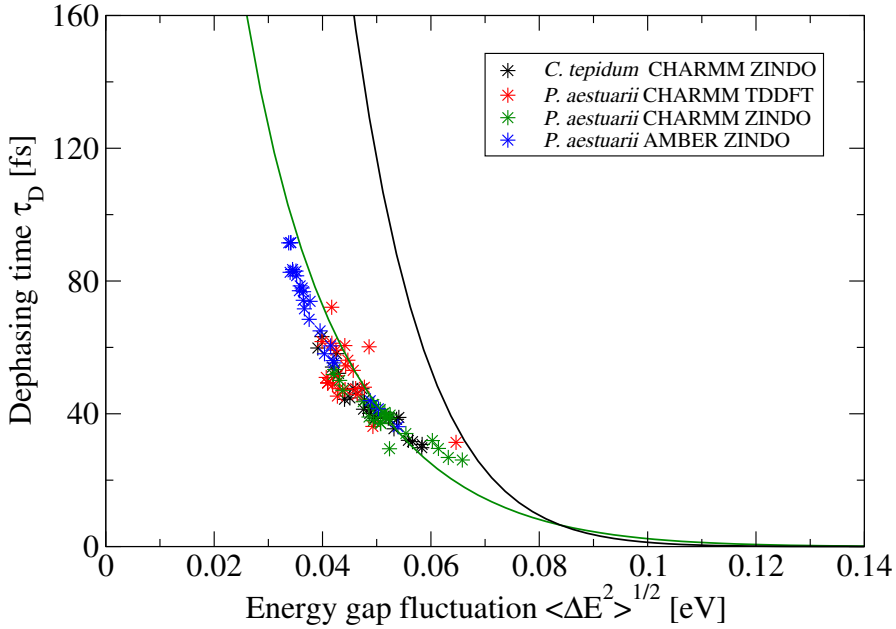

Figure 4.5: Independence of the relation between dephasing time and energy gap fluctuaction from methods used in the simulations.

ports the fact that the normalized correlation functions are basically influenced by the molecular structure of the studied subunit and not so much by its surroundings. This "molecular fingerprint" in turn leads to the observed relation between dephasing time and average gap fluctuations.

4.4 Conclusions

In this study we have shown that for BChl *a* molecules in different protein environments the respective normalized autocorrelation functions show a large degree of similarity and can be seen as a kind of "molecular fingerprint". These functions have a fast initial decay on a 5 fs time scale as well as oscillations on the 20 fs time scale. Assuming that these correlation functions can be approximated by a sum of two exponential functions, one with a fast and one with a long decay time, we were able to derive an expression for the dephasing time as function of the average energy gap fluctuation. The data from the molecular simulations can be fitted accurately with this functional form. Moreover, the calculation of the respective parameters in this function directly from a fit of the autocorrelation functions to sums of two exponential functions yields similar but not identical values which is not surprising taking into account the underlying assumptions. Nevertheless, with this generalized Kubo formalism we can understand that the dephasing times for

BChl *a* molecules in various protein systems show a unique functional dependence as a function of energy gap fluctuation. The PEB bilins from the PE545 complex show autocorrelation functions very similar to those of the BChl *a* molecules and actually follow the same behavior. For the DBV bilins from the same complex we can see distinctly larger oscillations in the correlation function leading to a different functional behavior for the dephasing time. The average energy gap fluctuations are much larger for the studied charge transfer systems. Based on the generalized Kubo model we can understand that in this case the dephasing time becomes much more independent of the details of the normalized correlation function. It is interesting to note that the analytic formula for the dephasing time obtained from the generalized Kubo theory does not depend on the long time scale $\tau_{c,2}$ of the autocorrelation function. A finding consistent with earlier results for simpler systems showing purely Gaussian dephasing functions [75]. This long time scale $\tau_{c,2}$, however, severely influences the low frequency part of the spectral density which is basically a half-sided Fourier transform of the autocorrelation function [31, 66, 111, 155]. This low frequency part of the spectral density is actually very important for the dephasing and exciton transfer dynamics in the full complex in which small energies between excitonic states of the full complex play a major role [144, 156, 157]. Therefore, we need to emphasize that the dephasing times determined in the present study are those for the individual chromophores and not the complete complexes. Further investigations are needed to unravel the connection of the present findings and the observed long-lived quantum coherences in detail. The present study, however, yields important insight into the behavior of individual pigments and their similarities in different protein environments. It needs to be seen in how much the present findings can be applied to other molecular and nanoscopic objects such as quantum dots [150], clusters [158] and nanocrystals [159].

Acknowledgements

This work has been supported by grant KL 1299/12-1 of the Deutsche Forschungsgemeinschaft (DFG).

Chapter 5

Relation Between Vibrational Dephasing Time and Energy Gap Fluctuations

Dephasing processes are present in basically all applications in which quantum mechanics plays a role. These applications certainly include excitation energy and charge transfer in biological systems. The present work extends a previous study to entire complexes. Electronically coupled pigments within the Fenna-Matthews-Olson and LH2 complexes as well as bilins in PE545 and PE555 aggregates are investigated. It can be concluded that a universal and inverse proportionality exists between dephasing time and variance of the excitonic energy gap fluctuations while the respective proportionality constants can be rationalized using the excitonic-gap autocorrelation functions. Furthermore, these findings can be extended to the gaps between higher-lying neighboring excitonic states

5.1 Introduction

Quantum effects in (bio)molecular complexes have attracted considerable attention in the last years [129–132, 160]. Environmental ramifications on these quantum mechanical processes are twofold. On the one hand, an energy relaxation sets in on the so-called T_1 time scale while, on the other hand, the quantum mechanical phases are lost on the usually much shorter T_2 time scale. This dephasing time can be due to vibrational, electronic or mixed vibronic effects. In any case, quantum phase relations are washed out and the processes lose their quantum nature.

In this study we focus on vibrational dephasing in light-harvesting systems. In case of electronic two-level systems with nuclear degrees of freedom, the vibrational dephasing can be theoretically determined using the so-called nuclear overlap/phase function since its magnitude is termed dephasing function [133,136–138]. The dephasing time is subsequently defined as an integral expression over the dephasing function [139, 140]. Different approximations have been performed previously to realize analytic expressions for the dephasing function. A purely Gaussian form can be obtained in the Fermi Golden rule and the high-temperature approximation [139] while also purely exponentially decaying dephasing functions can be reached [141]. In the present investigation we will compare numerical data for real systems to these functional forms. Due to the classical treatment of the bath, the present study only captures the dephasing and neglects the quantum nature of the bath degrees of freedom.

Interestingly, some earlier studies assumed a proportionality between correlation and dephasing times [142] while others explicitly showed an independence between the two time scales [75]. In our previous study on individual pigments, we found that, in general, a dependence exits between correlation and dephasing times [126]. Moreover, the latter two studies found a clear dependence between the dephasing times and the corresponding average energy gap fluctuations. The details of this dependence between these two quantities, however, seems to be different for varying systems. With the present study we want to contribute to clarifying this issue.

Aim of the present study is to analyze the dephasing times for the excitonic states in light-harvesting systems. The dephasing of the excitonic states of the whole molecular aggregates is much closer connected to the experiments in which excitonic states are excited than looking at individual chromophores as done previously [126]. At this point we want to mention that the related decoherence time has been determined experimentally for specific systems [161, 162]. Moreover, the dephasing function is, in fact, directly connected to the line shape and can thus

be estimated indirectly as well. However, a direct comparison between theoretical and experimental values is out of scope of the present work. Other theoretical schemes might actually make use of the results from the present study. In the popular approach of fewest switches surface hopping (FSSH), dephasing effects are not included properly since the vibrational bath is modeled classically [163, 164]. The present insight into the dephasing times in light-harvesting systems can help to introduce dephasing effects into surface hopping simulations of these complexes.

In the present study several LH complexes have been analyzed, i.e., the light-harvesting system 2 (LH2) [112], the Fenna-Matthews-Olson (FMO) trimer [143, 144], the PE545 system [66] as well as the PE555 aggregate [165]. At the same time, we have to clearly highlight the restriction of the present work to vibrational dephasing, i.e., electronic dephasing caused by different excitonic states is not included. Especially in regions with many avoided crossings between the excitonic states and strong non-adiabatic couplings, this shortcoming leads to artificially long (vibrational) dephasing times. The full (experimental) dephasing times will be shorter in these cases due to electronic dephasing effects between the excitonic surfaces. Nevertheless, an interesting universal dependence between vibrational dephasing time and average excitonic energy gap fluctuations is visible. As shown below, the relation between these two quantities is universal and the data points for the different excitonic states of one system lie on one curve.

5.2 Methods

5.2.1 Molecular Simulations

Before going into details of the dephasing times, we want to briefly describe the molecular simulations used to obtain the time series of excitonic states. The four analyzed simulations are listed in Tab. 5.1. These simulations consist of sequential combinations of classical molecular dynamics (MD) simulations and quantum mechanics/molecular mechanics (QM/MM) calculations for the excitation energy gaps of the individual pigments as previously done by our [66,143,144,156,165,166] and by other groups [77,113,155,167–172]. In addition, the excitonic couplings between the chromophores have been determined. At each time step, the full Hamiltonian can thus be constructed and diagonalized to obtain the excitonic states. Despite its limitation, e. g., the geometrical mismatch arising from the classical MD simulations being coupled to a quantum approach, this scheme is quite popular in the analysis of light-harvesting processes. Treating the dynamics of the system at least partially quantum mechanically to be more consistent with the

Number	System	Sites	Force field	Energy gap	Ref.
1	FMO complex, *C. tepidum*	24	CHARMM	ZINDO	143
2	LH2 complex, *R. acidophila*	27	CHARMM	ZINDO	151
3	PE545 complex, *Rhodomonas sp. CS24*	8	AMBER	ZINDO	66
4	PE555 complex, *Hermiselmis andersenii*	8	AMBER	ZINDO	165

Table 5.1: The four different light-harvesting systems together with some details and the corresponding references.

computations of the vertical excitation energies is computational much more expensive and, so far, has only been performed for a relatively small light-harvesting complex, i.e., the water-soluble chlorophyll-binding protein (WSCP) [154]. Non-adiabatic excited-state molecular dynamics has been applied to chlorophyll dimer only very recently [173]. In the present study, the LH2 and the FMO complexes contain bacteriochlorophylls (BChls) as their pigments while the two cryptophyte complexes PE545 as well as PE555 contain bilin molecules for capturing the sun light. The CHARMM as well as the AMBER force field sets have been employed for the 300 K MD simulations as listed in Tab. 5.1. For details of the simulations we refer the interested reader to the cited references. The site energies have been determined using the semi-empirical ZINDO/S-CI approach (Zerner Intermediate Neglect of Differential Overlap method with parameters for spectroscopic properties together with the configuration interaction scheme using single excitations only) [99]. In alternative calculations on the same or related complexes, Time-dependent Density Functional Theory (TDDFT) approaches have been employed resulting in similar results. For a comparison on the FMO complex, see Ref. 144. Moreover, the excitonic couplings have either been determined using the point-dipole approximation for the PE545 aggregate or the transition charges from electrostatic potentials (TrEsp) method for the three other systems. In our previous study for the dephasing time of individual pigments, different approaches for the site energy and coupling calculations were used and the main findings were robust with respect to these variations [126].

5.2.2 Theoretical Background

Using the above results from molecular simulations, the system Hamiltonian $\hat{H}_S(t)$ is given by the time-dependent tight-binding model with site energies $E_i(t)$ at site

i and intersite couplings $V_{ij}(t)$:

$$\hat{H}_S(t) = \sum_{i=1}^{N} E_i(t) \left|i\right\rangle \left\langle i\right| + \sum_{\substack{i,j=1 \\ i\neq j}}^{N} V_{ij}(t) \left|i\right\rangle \left\langle j\right| \ . \tag{5.1}$$

Based on this time-dependent Hamiltonian, adiabatic eigenstates $|\mu(t)\rangle$ can be defined as the instantaneous eigenstates of this Hamiltonian [174,175] via a time-dependent orthogonal transformation

$$\hat{H}'_S(t) = \sum_{\mu=1}^{N} \varepsilon_\mu(t) \left|\mu(t)\right\rangle \left\langle \mu(t)\right| \ . \tag{5.2}$$

Both the excitonic energies $\varepsilon_\mu(t)$ and the eigenstates $|\mu(t)\rangle$, depend on the actual time at which the Hamiltonian is diagonalized. Exciton energy levels for different light harvesting systems along pieces of MD trajectories are shown in Fig. S1. Moreover, the contribution of the different sites to the excitonic states are discussed in the supplementary information.

In a previous study the dephasing time as a function of energy gap fluctuation has been analyzed for the uncoupled pigments [126]. Here, this investigation is extended to excitonic states which include also the effect of time-dependent electronic couplings between the pigments. For the sake of completeness, we review the basics of the dephasing time theory with a focus on the present applications. Moreover, for the sake of simplicity, we suppress the index for the excitonic states since it should be evident that each excitonic state has its own dephasing time.

The present theoretical consideration is based on generalized version of Kubo's stochastic line shape theory [125]. To this end, one defines the energy gap $\Delta\varepsilon = \varepsilon - \langle\varepsilon\rangle$ and its fluctuation quantified using the standard deviation $\langle\Delta\varepsilon^2\rangle^{1/2}$. In the present case this quantity, of course, refers to the gap between excitonic energies.

$$\langle\Delta\varepsilon^2\rangle^{1/2} = \sqrt{\langle\Delta\varepsilon^2\rangle - \langle\Delta\varepsilon\rangle^2} \ . \tag{5.3}$$

Gaussian random processes with mean value zero are at the heart of Kubo's line-shape theory and its generalized version [148]. The unnormalized autocorrelation function is assumed to be a sum of two exponential functions

$$C(t) = \langle\Delta\varepsilon^2\rangle \left(\alpha_1 \exp\left(-t/\tau_{c,1}\right) + \alpha_2 \exp\left(-t/\tau_{c,2}\right)\right) \tag{5.4}$$

This function contains two normalized prefactors α_1 and α_2, i.e., $\alpha_1 + \alpha_2 = 1$, as well as correlation times $\tau_{c,1}$ and $\tau_{c,2}$. The correlation function of the excitonic states depends on the time-dependent nuclear coordinates of the system under

investigation. Using a cumulant approximation [78], the dephasing function $D(t)$ can be defined as

$$D(t) \equiv \exp(-g(t)) = \exp\left[-\frac{1}{\hbar^2}\int_0^t d\tau (t-\tau)\langle\Delta\varepsilon(\tau)\Delta\varepsilon(0)\rangle\right] \ . \tag{5.5}$$

where $g(t)$ is the line shape function. This function is of crucial importance for the present study since it is used to define the dephasing time. It is related to the line shape $I(\omega)$ which can be given as

$$I(\omega) = \frac{1}{\pi}\int_0^\infty dt \cos(\omega t)\exp\left[-D(t)\right] \ . \tag{5.6}$$

Using the analytic approximation of the correclation function, Eq. (5.4), and assuming that one of the two correlation times is very short while the other one is large, one obtains [149]

$$D(t) = \exp\left[-\frac{\langle\Delta\varepsilon^2\rangle}{\hbar^2}(\alpha_1\tau_{c,1}t + \alpha_2 t^2/2)\right] \tag{5.7}$$

Based on the dephasing function, the dephasing time is defined as

$$\tau_D = \frac{2}{\sqrt{\pi}}\int_0^\infty D(t)dt \ . \tag{5.8}$$

As already shown in Ref. 126, the relation between the dephasing time and the energy gap fluctuation can be given in an analytic form

$$\tau_D = \sqrt{\frac{2\hbar^2}{\langle\Delta\varepsilon^2\rangle\alpha_2}}e^{-\langle\Delta\varepsilon^2\rangle A}\mathrm{erfc}\left(\sqrt{\langle\Delta\varepsilon^2\rangle A}\right) \tag{5.9}$$

with $\mathrm{erfc}(x)$ denoting the complementary error function and

$$A = \frac{\tau_1^2}{2\hbar^2}\frac{\alpha_1^2}{\alpha_2} \ . \tag{5.10}$$

Two limiting cases can be given for the dephasing time expression. For vanisihing α_1. i.e. in the so-called Gaussian limit, the dephasing time can be written as

$$\tau_{D,G} = \frac{B}{\sqrt{\langle\Delta\varepsilon^2\rangle}} \ . \tag{5.11}$$

The constant B has a value of $B = \sqrt{2}\hbar$ according to Kubo's theory [125] though alternative values have been discussed as well [75,126]. In the opposite exponential limit, i.e., with vanishing α_2, one gets

$$\tau_{D,E} = \frac{2\hbar^2}{\sqrt{\pi}\tau_{c,1}\langle\Delta\varepsilon^2\rangle} \ . \tag{5.12}$$

As will be seen below, for the case of excitonic energies, this exponential limit is of prime interest together with its dependence on the correlation time $\tau_{c,1}$.

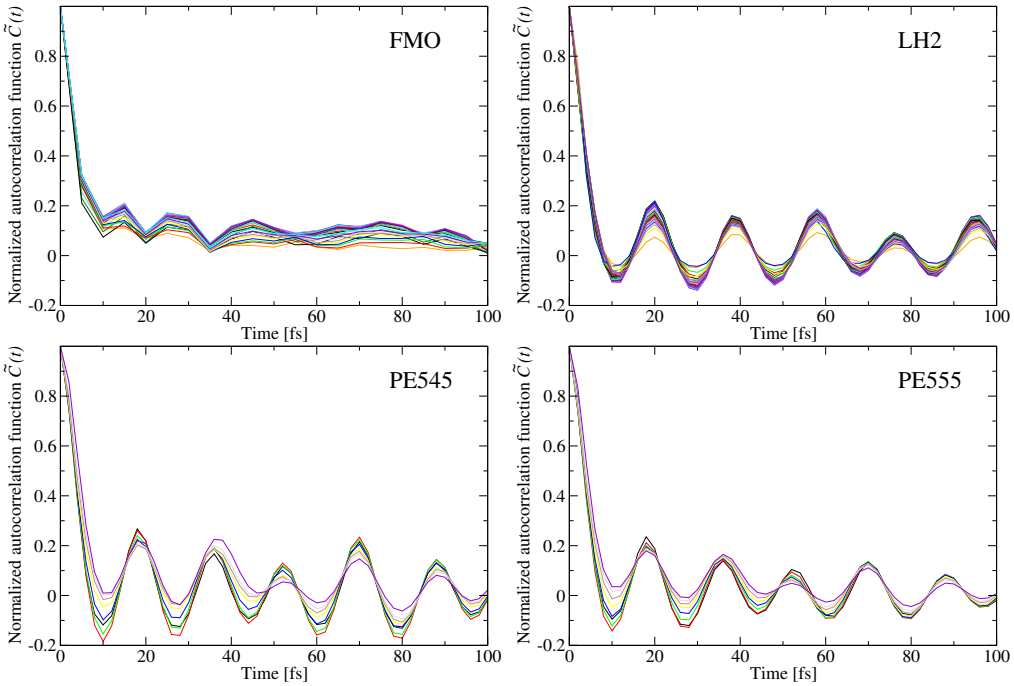

Figure 5.1: Normalized autocorrelation functions for different light harvesting complexes.

5.3 Results and Discussion

5.3.1 Correlation functions and their functional behavior

Starting from the energy eigenvalue for each site i and the respective couplings between them, exciton energies have been calculated. Subsequently, the excitonic autocorrelation functions $C(t)$ have been built. More interesting than the unnormalized correlation function is its normalized counterpart $\tilde{C}(t)$. As can be seen in Fig. 5.1 these normalized correlation functions do behave very similar for all excitonic states within one particular system. At the same time, these normalized functions do significantly differ even if they contain the same pigments like BChl a molecules in the case of LH2 and FMO. In case of the FMO system, the normalized autocorrelation seems to be dominated by two decays, one very fast one and one much slower one. The latter decay is superimposed by some remnants of some oscillation while for the other three systems, a clear oscillatory pattern is visible. When looking at the normalized correlation functions for the individual pigments [126], the situation was different. These functions were mostly determined by the chemical structure of the pigment and not by its surroundings. Thus, in that case, the normalized autocorrelation functions for pigments in LH2

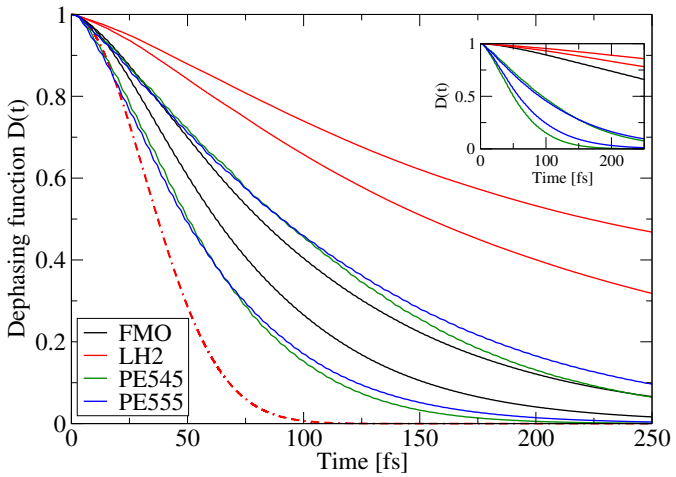

Figure 5.2: Examples of some dephasing functions (two per system). In the main panel the dephasing functions are scaled on top a perfect Gaussian function (red dashed line), while in the inset the unscaled dephasing functions are depicted.

and FMO were quite similar.

Nevertheless, there is a common feature of the normalized autocorrelation functions of the excitonic systems for the systems shown in Fig. 5.1. This feature is the fast initial decay which corresponds to a $\tau_{c,1}$ time of roughly 5 fs. To understand this common property of the correlation functions one has to analyze their functional forms. In addition to the fast initial decay, another important feature is the fast oscillation with a period length of about 20 fs. For the BChl and bilins molecules the fast oscillations are caused by modes involving C=C and C=O double bond vibrations [114]. In the shown autocorrelation functions, these fast oscillations are overlayed by a relatively fast damping. Despite the different damping times for the various systems, the fast initial decay is a reminiscent of the 20 fs oscillation, i.e., it corresponds to the first quarter of these oscillations.

5.3.2 Dephasing times

The dephasing function is defined in Eq. 5.5 and the numerical data for different excitonic states are shown in Fig. 5.2. Depicted are unscaled dephasing functions in the inset of the figure but more importantly scaled versions thereof. These scaled functions have been constructed to have the same initial behavior for short times. Shown in this figure is a perfect Gaussian function for comparison. Although all dephasing functions do have a Gaussian behavior for short times due to their definition, this turns over into an exponential form rather quickly. Apparently the short time behavior of the correlation function plays a more important role than

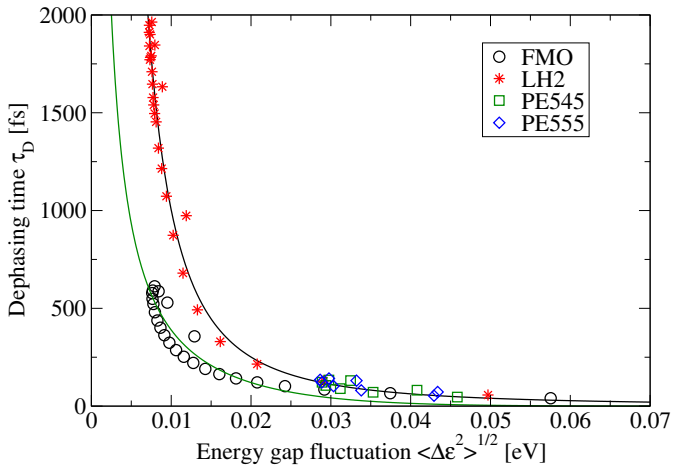

Figure 5.3: Relation between dephasing times and energy gap fluctuations for various light harvesting systems. The black and green solid lines show exponential fits of the data according to Eqs. 5.12 and 5.9, respectively, as discussed in the text.

the oscillating long time appearance. The contribution of these oscillatory parts of the correlation functions is canceled out to a larger degree due to the integral form of the dephasing function. Actually, all dephasing functions analyzed in the present study show a clear exponential behavior. This finding is different from that in case of dephasing functions for individual sites showing a Gaussian behavior in most cases.

The dephasing times as function of the exciton energy gap fluctuations are shown in Fig. 5.3. Plotted are the results of the numerical integration according to Eq. 5.8 based on the numerical data of the dephasing functions. A clear inverse proportionality between dephasing time and average exciton energy gap fluctuation is visible. Those excitonic states with energies in the middle of the excitonic spectrum have, in general, the smallest average energy gap fluctuations due to the avoided crossings (see Fig. S1). The excitonic states with the largest and smallest energies, however, are subject to less avoided crossings, leading to larger gap fluctuations which in turn results in shorter dephasing times. Looking at Fig. 5.3 it also becomes apparent that the results for the FMO system lie on a different curve than those for the other three systems. This different behavior can be traced back to the unlike autocorrelation functions. In case of the LH2, PE545 and PE555 complexes, the correlation functions have a sharp initial decay on a 5 fs time scale followed by oscillations which survive much longer than 100 fs. For the determination of the dephasing functions and subsequently dephasing times, the contributions of the oscillatory parts do average out to quite some extend.

Thus we can reasonably well approximate these autocorrelation functions by their initial exponential decay only. This approximation leads to the exponential limit for the dephasing time given in Eq. 5.12. Fitting the data for LH2, PE545 and PE55 in Fig. 5.3 to this exponential limit yields a value for the correlation time $\tau_{c,1}$ of 4.9 fs in excellent agreement with the correlation times visible in Fig. 5.1.

In case of the FMO complex the story is slightly more complicated. As mentioned above, these correlation functions are better approximated by a double-exponential form with a short correlation time of around 5 fs and a long one of about 100 fs. Thus, the functional form is of the shape given in Eq. 5.4 leading to the more general form of the dephasing time given by Eq. 5.9. Fitting the numerical data, we obtained $\tau_{c,1} = 3.6$ fs, $\alpha_1 = 0.98$ and thus $\alpha_2 = 0.02$. Thus, this fit yields a basically exponential behavior which is actually consistent with the form of the dephasing functions (examples shown in Fig. 5.2). In total and as in case of the dephasing times for the individual pigments discussed in Ref. 126, one gets a clearly inverse proportional relation between dephasing time and average gap fluctuation but the respective proportionality factor can possibly differ between systems for excitonic states.

5.3.3 Neighbouring Energies

As suggested by Akimov and Prezhdo [75], the energy fluctuations between neighboring exciton energy levels could lie on the same curve as the energy fluctuations of the first exciton levels relative to the excitonic ground state. Therefore, the same process as described above was repeated for the same systems comparing neighboring excitonic energies. This means that the energies used now correspond to the energies $\varepsilon_2 - \varepsilon_1$, $\varepsilon_3 - \varepsilon_2$, etc. The number of gaps between neighboring states is $n-1$ with n being the number of pigments in the system. We want to point out that even if these dephasing times have no direct experimental counterparts, the analysis has been extended to these gaps to further validate the present model. It turns out that, no matter where the gap fluctuation originates from, the relation between this quantity and the corresponding dephasing time is still valid.

The corresponding excitonic energy gap autocorrelation functions are shown in Fig. 5.4. One has to realize that the autocorrelation decays very quickly for the gaps between neighboring states and therefore only part of the functions are shown in Fig. 5.4. This finding clearly shows that the oscillations in this case are much smaller than those for the case of the energy gaps between ground and the respective excitonic state shown in Fig. 5.1. The form of the oscillations are partially non-sinusoidal caused by the avoided crossings. Moreover, the oscillations

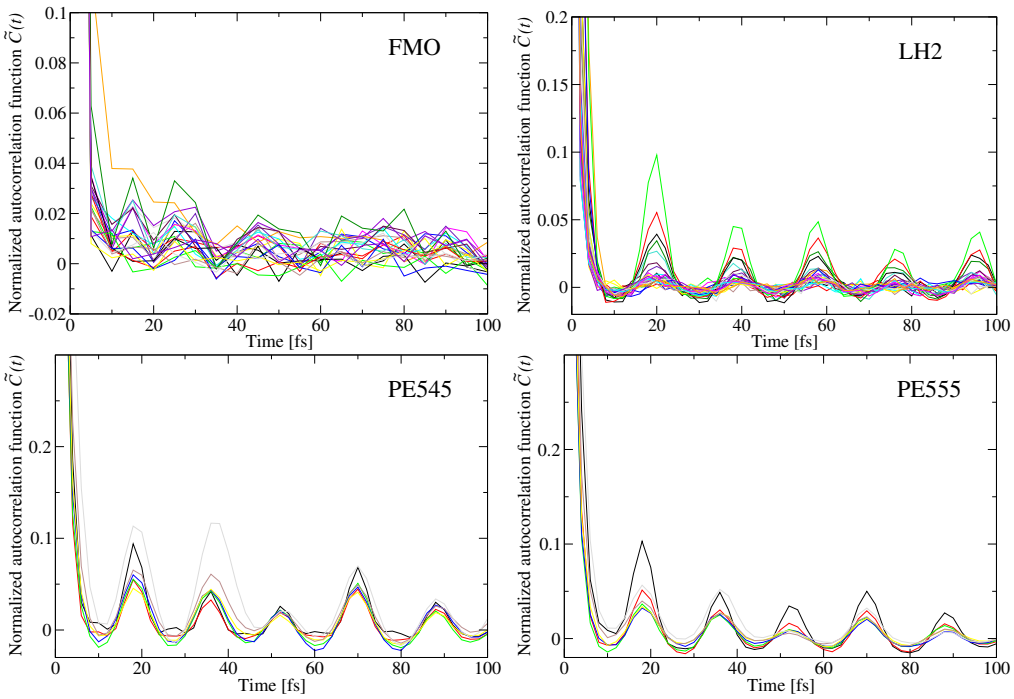

Figure 5.4: Normalized autocorrelation functions for neighbouring energy gaps fluctuations for different light harvesting systems.

do hardly reach values below zero. Nevertheless, the data is clearly dominated by the very fast initial decay down to almost zero independent of the system. Thus, for this case of neighboring exciton energy level we expect all data to lie on one curve as they show the same behavior of the autocorrelation function.

Examples of dephasing functions for the case of neighboring excitonic states are shown in Fig. 5.5. Since the autocorrelations functions were dominated by the fast initial decay even more than in the previous case, it is not surprising to see that the dephasing functions have a clear exponential behavior.

Determining the dephasing times numerically, again led to a picture in which all results are close to one line. The data was again fitted with the analytical form for the dephasing time based on the exponential limit, i.e., Eq. 5.12. This time the numerical value obtained by this fitting procedure was $\tau_{c,1} = 4.1$ fs can being consistent with the form of the autocorrelation functions.

5.4 Conclusions

The present investigation extends an earlier study on the dephasing times of the individual pigments in light-harvesting systems [126]. Determining the dephasing

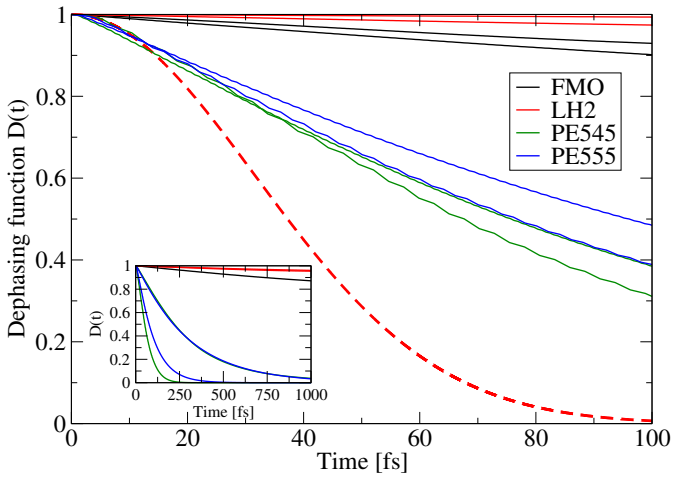

Figure 5.5: Examples of some dephasing functions for neighbouring energy gap fluctuations (two per system). In the main panel the dephasing functions are scaled on top a perfect Gaussian function (red dashed line), while in the inset the unscaled dephasing functions are depicted.

times for excitonic states rather than excitations of individual pigments offers the advantage of being closer to experiment since experimentally only excitons of the whole complex can be excited. Moreover, the dephasing function, for example, is associated with the line shape function. Thus, even if a direct measure is not possible, an indirect estimation should be feasible nevertheless. The autocorrelation functions for excitonic and site energies do actually look quite similar. Both have a fast initial decay on a time scale of a couple of fs followed by a damped oscillatory behavior. This damping of the oscillation does, however, differ more between systems for the excitonic than for the site energies. Further differences between site and excitonic energies are visible for the dephasing function which is being determined based on the autocorrelation function. In case of the individual chromophores, most dephasing functions had a clear turnover to an exponential form after a short Gaussian period which is always present due to the definition of the dephasing function. In this case, some dephasing functions, however, showed a Gaussian form over the complete time range. The respective systems included electron transfer systems which are not at the focus of the present investigation. For the investigated excitonic states, no such pure Gaussian behavior was observed. Thus, the relation between dephasing time and average excitonic energy gap fluctuation can nicely be fitted using the expression for exponential limit of the relation between these two quantities (Eq. 5.12). This finding also results in the fact that the dephasing times for the present light-harvesting systems de-

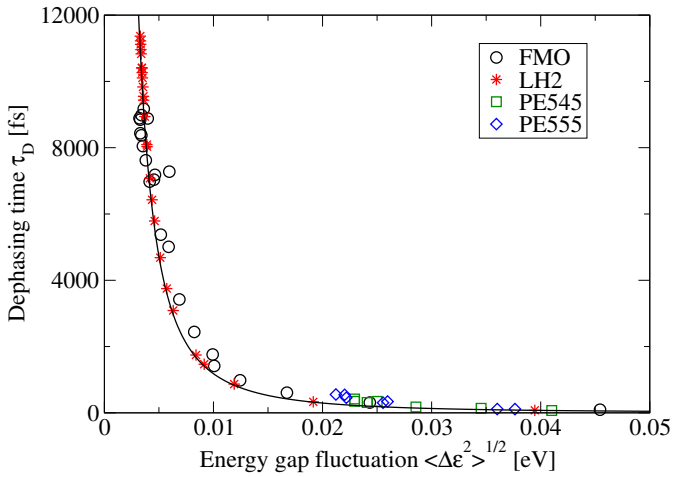

Figure 5.6: Relation between dephasing times and neighbouring energy gap fluctuations for various light harvesting systems. The solid line shows an exponential fit to the data according to Eq. 5.12 with fitting constant $\tau_{c,1} = 4.1$ fs

pend inversely on the correlation time, i.e., the fast initial decay of the correlation function (see Eq. 5.12). This dependence of the correlation time is, however, in contrast to the findings by Akimov and Prezhdo [75] for molecular dimers in different solutions. In that case, the dephasing times were found to be independent of the correlation time. Certainly, one has to keep in mind that the those systems and environments are clearly different from the ones in the present study.

In case of an excitation from the ground to the first exciton state, the dephasing times reach up to 800 fs in the present study. This finding is indeed on the order of the experimentally observed long-lived quantum coherences [131, 132]. At the same time, one has to keep in mind that the present definition of the dephasing time does only include vibrational dephasing effects. Dephasing effects due to the different excitonic surfaces are not included. Especially, when many similar pigments are involved, the respective excitonic states come pretty close and avoided crossings are ubiquitous. In the limit of very dense electronic states, the electronic dephasing would eventually take over in importance. In addition, the quantum nature of the bath is not taken into account neglecting possible additional decoherence effects [133]. Thus, the obtained dephasing times should be seen as upper limits of decoherence times since electronic effects would shorten these times. Moreover, the calculations have been extended to the analysis of neighboring energy gaps. Again, it can be concluded that the data do show a clear inverse proportionality. The dephasing times of the different systems can, however, be quite different and might be used as input of further theoretical considerations

such as the surface hopping formalism [163, 164]. In this context it is interesting to note that recent variants of that formalism [69, 176, 177] include energy-based decoherence corrections, i.e., dephasing times between two states in the surface hopping algorithm. The dephasing times between neighboring electronic times determined in the present study should indeed be closely related to the energy-based decoherence correction for these variants of the surface hopping approach.

Supporting Information

Details of the excitonic energies and the respective site contributions are discussed in the supplementary material.

Acknowledgements

We thank Mortaza Aghtar and Suryanarayanan Chandrasekaran for providing the time-dependent Hamiltonians of the cryptophyte systems. This work has been supported by grant KL 1299/12-1 of the Deutsche Forschungsgemeinschaft (DFG).

5.5 Supplementary Information

5.5.1 Exciton Energies and Their Behavior

At this point we need to mention that for the PE545 system, the employed quantum chemistry approach leads to a rather poor approximation of the linear absorption spectrum. Thus, and as has been introduced earlier already in Ref. [157], the site energies of the DBV bilins have been shifted towards higher energies by 0.09919 eV while the site energies of the PEB bilins by 0.23557 eV. Actually for the quantum dynamics and the dephasing discussed in this study, only the relative shift between the two types of bilins matters. Apparently the employed ZINDO/S-CIS approach cannot properly distinguish between the two type of bilins concerning the vertical excitation energies.

Shown in Fig. 5.7 are the excitonic energies for different systems. These plots are quite crowded though it is clear that the different excitonic energy states do not cross. The states are energetically ordered at each time step. Please note that the states in the middle of the spectra do show reduced fluctuations due to avoided crossings with neighboring states. The levels at the edges of the spectra, however, show fluctuations closer to those known from the site energies [126] since these states at the edge of the spectrum do have less avoided crossings.

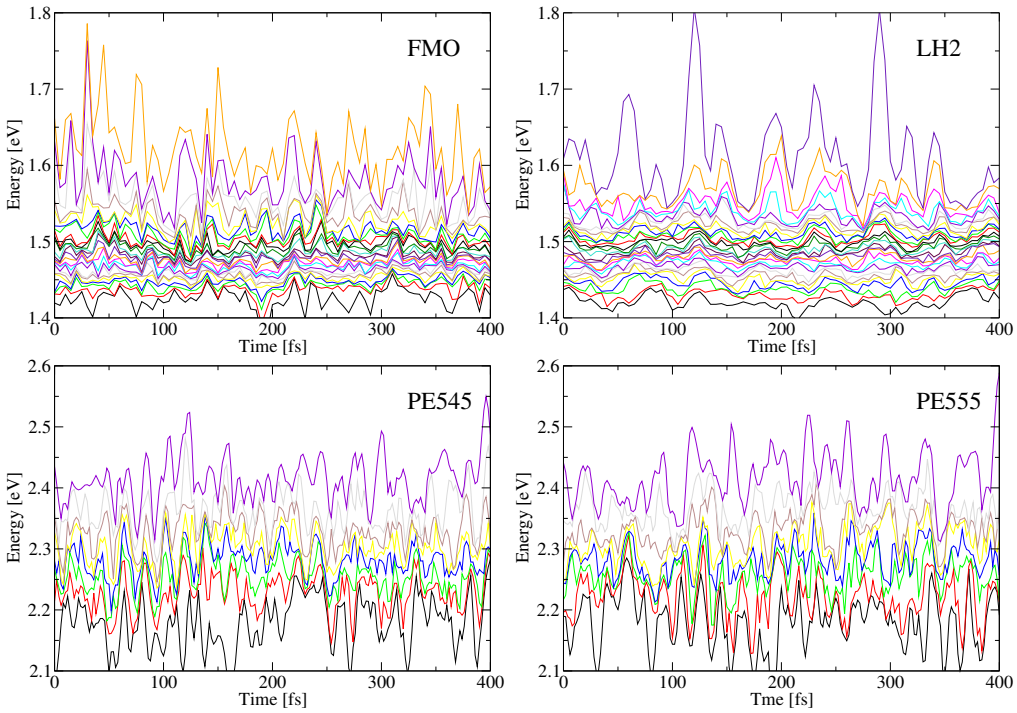

Figure 5.7: Exciton energy levels for different light harvesting systems along pieces of MD trajectories.

Very small coupling values lead to avoided crossing for which the gap can be very small, however. In dynamical simulations these gaps might be overcome due to non-adiabatic crossings. In the present theory on vibrational dephasing times, non-adiabatic crossing are not considered. As an example, we want to mention the FMO trimer with 24 pigments in total. This trimer can be split into three monomers which are electronically coupled to each other only very weakly. Thus, although sets of eight pigments seem to act independently of the other 16 chromophores, the excitonic spectra do differ significantly when analyzing the three monomers separately or the whole trimer due to the small but non-zero couplings between pigments of neighboring monomers.

5.5.2 Site Contributions

In time-independent considerations, the contribution of the different sites in the systems to specific excitonic eigenstates are often analyzed and interpreted. To show that the excitonic states do behave very differently we have plotted the absolute value squares of some of the adiabatic expansion coefficients in Fig. 5.8 for the PE545 system. The figure only shows the first three expansion coefficients for three eigenstates in the 8-pigment system for which in total $8 \times 8 = 64$ coefficients

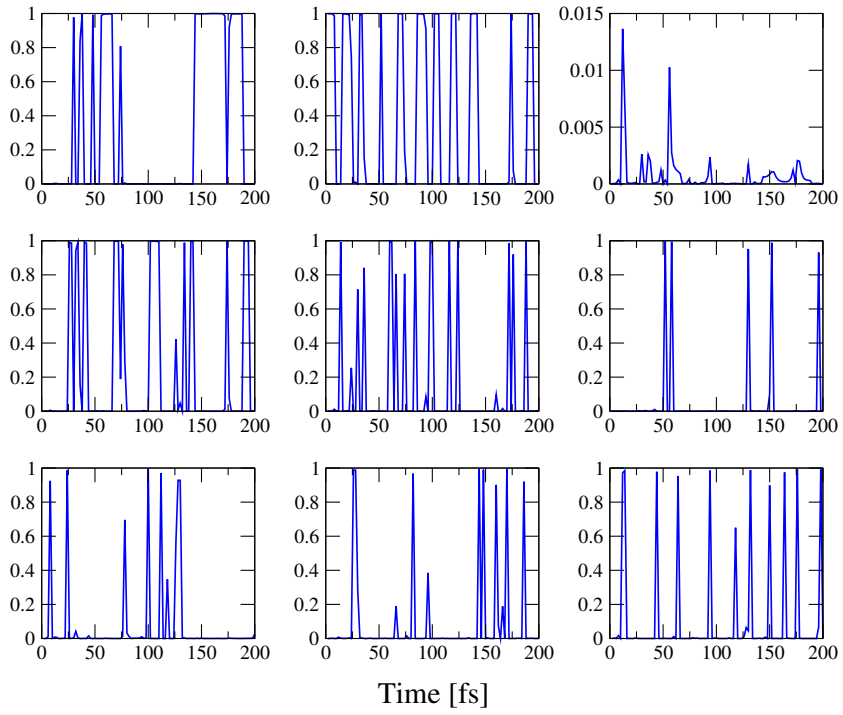

Figure 5.8: As an example, three squared adiabatic exciton expansion coefficients for three eigenstates in the PE545 system along a piece of the respective MD trajectory.

are present. As, for example, studied earlier for a dendrimer system [174,175], the expansion coefficients of the excitonic state in the site basis do heavily fluctuate in time. This finding is a direct consequence of the larger energy fluctuations of the site energies compared to the energy differences between the average site energies at different sites. The contribution of individual chromophores to specific eigenstates can vary between 0 and 1 within femtoseconds. Thus, it is clear that an interpretation of the results in terms of pigment contributions to specific excitons is at least problematic when analyzed in a time-dependent fashion.

Chapter 6

Environmental Effects on the Light-Harvesting Complexes LH2 and LH3 Based on Molecular Simulations

A multi-scale approach that combines molecular dynamics simulations and quantum chemistry methods is used to obtain different properties such as correlation functions, spectral densities and exciton dynamics for three similar systems: the light-harvesting complex 2 (LH2) of the purple bacterium *Rhodospirillum molischianum* as well as for the light-harvesting complexes 2 (LH2) and 3 (LH3) of *Rhodoblastus acidophilus*. Initially, molecular dynamics simulation are performed starting from the crystal structures of the three systems. On top of the MD trajectories, the semi-empirical ZINDO/S-CIS approach has been used to calculate the fluctuations of the energy gaps between ground and first excited states for individual pigments of each system. Furthermore, the TrEsp method for determining the couplings between the individual pigments has been used. The total Hamiltonian of each system has been built and the population dynamics is analyzed, to estimate the transport properties, resulting in a different behavior of the two rings.

This work has been done by by M. I. Mallus, Y. Shakya, J. Prajapati and U. Kleinekathöfer. Task of the author of the present thesis was to perform the complete set of calculations for the LH2 complexes and to contribute to the analysis of the LH3 complex.

6.1 Introduction

Among the photosynthetic bacteria, purple bacteria are the oldest photosynthetic organisms. Two types of LH complexes are present in purple bacteria: the light harvesting complex 1 (LH1) and peripheral LH complexes, also called antenna complexes. Antenna complexes are composed of light harvesting complex 2 (LH2) and sometimes light harvesting complex 3 (LH3). LH3, which absorbs at shifted wavelength, is present under low light conditions [42]. Numerous studies on the light-harvesting complexes of purple bacteria have been performed [33, 77, 111, 178–180]. In recent years the experimentally observed long-lived coherence in several light-harvesting systems [13, 16, 24] has raised considerable effort to understand these effects experimentally as well as theoretically [32, 156, 181, 182]. The importance of these coherence phenomena *in vivo* is, however, still debated [17]. Also in case of LH2 complexes in purple bacteria long-lived quantum coherence have been studied experimentally as well as theoretically [183–186]. Even *in vivo* coherences in LH2 complexes were observed using two-dimensional electronic spectroscopy [132, 187]. It is, however, not the aim of this work to assign the nature of these coherences but to provide an atomistic description of some of the properties of these systems. The crystal structures of several LH complexes from different purple bacteria are known, including LH2 of *Rhodospirillum molischianum* [45] and *Rhodoblastus (Rbl.) acidophilus* [44, 188] (previously known as *Rhodopseudomonas acidophila* [189]) as well as LH3 of *Rbl. acidophilus* [42]. The knowledge of these molecular details has enabled numerous theoretical studies to investigate these systems at atomic level. Due to the size of the systems in their natural environment, i.e., in a membrane and surrounded by water, almost all atomistic studies start with a classical molecular dynamics simulation which yield the thermal fluctuations of systems of the size of individual LH systems or even larger [190]. Despite its power, the MD simulation is a classical technique and can not be used to study excited-state or energy transfer properties. Therefore, it has be used in combination with some quantum chemistry approaches. Due to the number and size of the pigments, semi-empirical methods are often employed. Other studies use density function approaches with small to medium size basis sets. In the present study we employ the ZINDO/S-CIS approach (Zerner's Intermediate Neglect of Differential orbital with parameters for spectroscopic properties combined with the configuration interaction formalism at the single configuration level) [96–98] to determine the vertical excitation energies of the individual pigments, i.e., the bacterio-chlorophyl *a* (BChl *a*). This approach combined with MD trajectories has been applied to quite some LH systems within

the subsystem-based approach [66,99,112,143,156,172,191–196] and other systems as well, e.g., Refs. 197–199. The electronic coupling between the individual pigments will be determined via the Transition charges from Electrostatic potential (TrEsp) [105, 200] method.
Aim of the present work is to describe and compare optical and exciton transfer properties of three different LH systems, the LH2 complexes of *Rsp. molischianum* and of *Rbl. acidophilus* and the LH3 complex of *Rbl. acidophilus*. The present contribution starts with a description of the theoretical background to make the results easier to comprehend. The section starts with a detailed description of the MD simulations, the technique used to compute the thermal fluctuations of the ground states of the pigments. On top of these trajectories, the ZINDO/S-CIS method has been used to compute the vertical transitions energies between ground and first excited states, also known as site energies. The density of states (DOS) of the site energies are presented and used as a input to compute the autocorrelation functions and spectral densities of the individual BChl molecules. These findings can then be used to discuss the influence of the environment and the differences between the three systems under investigation. In a further step, the couplings between the pigments have been calculated. Subsequently, the total Hamiltonian of each system has been built and the ensemble-averaged wave-packet dynamics approach is used to evaluate the different exciton transfer properties of the different pigment rings of each system. It will be shown how different the exciton transfer dynamics is in the rings and that these variations are due to the unequal environmental properties and arrangements of the BChls in the two rings. Finally, the results are discussed in the last section.

6.2 Molecular-level Description of the LH Systems

6.2.1 Molecular Dynamics Simulations

The simulations for the LH2 and LH3 complexes of are based on their crystal structures. The structures are taken from the Protein Data Bank, with entries PDB:1LGH [45], PDB:1NKZ [201] and PDB:1IJD [42] for LH2 of *Rsp. molishianum*, LH2 of *Rbl. acidophilus* and LH3 of *Rbl. acidophilus* respectively. The same setup has been adopted for the two LH2 complexes, while a more complicated setup was required for the LH3 complex. In the first case, water molecules have been added on both sides to the POPC (1-palmitoyl-2-oleoyl-sn-glycero-3-

phosphocholine) lipid bilayer membrane into which each complex was embedded. The two systems were neutralized using Cl^- ions. The two final systems consisted of 114.011 and 154.708 atoms for LH2 of *Rsp. molischianum* and LH2 of *Rbl. acidophilus* respectively. Following an energy minimization, a 10 ns equilibration at room temperature and 1 atm pressure was performed employing the particle mesh Ewald (PME) method and a 2 fs time step using the SHAKE constraint on all hydrogen atoms. In the case of the LH3 complex, the deposited structure consisted of only three copies of the transmembrane α and β-apoprotein, B820 α, B820 β and B800 and carotenoid pigments. The missing residues were predicted using the MODELLER version 9.15 [202] with homology modeling based approach by considering the LH2 structure (PDB ID: 1NKZ) [201] from *Rbl. acidophilus* bacterium as template structure. Later on, the remaining six copies for all the components were built using the VMD version 9.1 [43]. Subsequently, the whole complex was aligned to the z-axis and inserted into the pre-equilibrated and fully hydrated POPC lipid bilayer. After elimination of overlapping lipid with complex, total 353 lipid were left in the inner cavity and surrounding. At next step, system was solvated with TIP3P water molecules and neutralized with Cl^- ions. The final system was composed of 158.992 atoms. After energy minimization of 50000 steps, the system was equilibrated for 1 ns using a NVT ensemble at 300 K with a time step of 1 fs. During this step, only the lipid tails can fluctuate. Next, the system was equilibrated for 4 ns using a NPT ensemble to keep the pressure at 1 bar. The constrains were applied to protein backbone, Bchl*a*, carotenoid and water atoms during this step. Furthermore, the constraints from the water molecules were removed and the equilibration was performed for 10 ns in NPT ensemble by keeping the constraints of the protein backbone, Bchl*a* and carotenoid atoms. Finally, the whole system was equilibrated for 4 ns in NPT ensemble without applying any constraints. As the carotenoid found in LH3 complex, rhodopinal glucoside, is modified form of the rhodopin glucoside caratenoid found in LH2 complex of the same bacterium, the new parameters were predicted using the CGenFF database [203–205] For all three MD simulations, the temperature and pressure were maintained using the Langevin dynamics along with a Langevin piston algorithm. Periodic boundary conditions were used. The cutoff of 12 Å was adopted for short-range nonbonded interactions. The long-range electrostatic interactions were treated with particle mesh Ewald (PME) method [206]. All three simulations were performed using the NAMD version 2.9 [207] and CHARMM27 force fields for the protein, lipid and waters [122]. the force fields reported in Ref. 111 for the BChls and caroteinoids were used. The production run is 250 ps long for the three simulations, with a 1 fs time step. All atomic coordinates were saved every 2 fs.

6.2.2 Spectral Densities and Exciton Dynamics

The so-called spectral density $J(\omega)$ is a key quatity in the theory of open quantum systems, used to describe the exciton dynamics of a certain systems. It describes the frequency-dependent coupling between the excitonic sub-system and its environment. Starting with a classical autocorrelation function $C(t)$, the spectral density $J(\omega)$ can be determined by [113]

$$J(\omega) = \frac{\beta\omega}{\pi} \int_0^\infty dt C(t) \cos(\omega t) \tag{6.1}$$

where $\beta = 1/(k_B T)$ denotes the inverse temperature and $C(t)$ the autocorrelation function. More details on the definition and derivations of $J(\omega)$ can be found in Sec. 3.3. Not only the excitation energies fluctuate along the MD trajectory. Also the electronic couplings between the pigments do so. Estimations for the couplings in purple bacteria have been listed for example, in Ref. 208. Various methods exist to determine the coupling values and here the TrEsp method has been used. In this approach, the interaction between pigments is modeled as a Coulomb interaction between the I transition charges q_I^T located in the two pigments. The coupling between two pigment molecules is then given by

$$V_{nm} = \frac{f}{4\pi\epsilon_0} \sum_{I,J} \frac{q_I^T \cdot q_J^T}{|\mathbf{R}_m^I - \mathbf{R}_n^J|} \ . \tag{6.2}$$

where f denotes the screening factor.

For a more detailed description of the coupling term and of its composing terms, such as the transition partial charges and the screening factor, see Sec. 3.1.2. The gap between the ground and the Q_y states E_m together with the electronic couplings V_{nm} lead to a time-dependent Hamiltonian:

$$H = \sum_m (E_m + \Delta E_m(t)) \left|m\right\rangle \left\langle m\right| + \sum_{n \neq m} V_{nm} \left|n\right\rangle \left\langle m\right| \tag{6.3}$$

This Hamiltonian can be employed in a subsequent step to directly use wave packet dynamics approach, e. g., in the Ehrenfest approximations. [174, 209–211].

If one wants to understand the dynamic properties of the exciton, this Hamiltonian must be diagonalized for each time step, by solving:

$$i\hbar \frac{\partial \Psi_S(t)}{\partial t} = H \Psi_S(t) \tag{6.4}$$

where $\Psi_S(t)$ is the total wave function of the system and it can be expanded in the exciton basis, $\left|\Psi_S(t)\right\rangle = \sum_\alpha c_\alpha(t) \left|\alpha\right\rangle$. Since only the expansion coefficients

depend on time, solving Eq. 6.4 is equivalent to solve:

$$i\hbar\frac{dc_\alpha(t)}{dt} = \varepsilon_\alpha + \sum_{\alpha\beta} J_{\alpha\beta}(t)c_\beta(t)J_{\alpha\beta}(t) = \sum_j c_j^\alpha c_j^\beta \Delta E_j(t) \tag{6.5}$$

where $J_{\alpha\beta}(t)$ represents the system-bath interaction Hamiltonian. The excitonic states $|\alpha\rangle$ have been expanded in the site basis, i.e., $|\alpha\rangle = \sum_m^\alpha c_m^\alpha |m\rangle$. The probability to find the exciton in a particular pigment m at the time step t can be calculated by projecting $\Psi_S(t)$ in that pigment:

$$P_m(t) = |\langle m|\Psi\rangle|^2 = |\sum_\alpha c_m^\alpha c_\alpha(t)|^2 \tag{6.6}$$

By plotting this probability over time, one gets the so-called population dynamics, to observe the exciton transfer in a particular system. The population dynamics will be evaluated for the two rings separately, and then compared for the three systems.

6.3 Results

The multiscale scheme adopted in the present work starts with MD simulations of the investigated systems. The key property when trying to determine spectral densities is the vertical excitation energy. The vertical excitation energies have to be determined for each system,for each BChl along the trajectory composed of 125000 snapshots. This leads to 24×125.000, 27×125.000 and 27×125.000, i.e., 3.000.000, 3.375.000 and 3.375.000 excitation energy calculations for the LH2 complexes of *Rsp. molischianum* and *Rbl. acidophilus* and for the LH3 complex of *Rbl. acidophilus*, respectively.

The vertical excitation energies, also called site energies, along the MD trajectories lead to rather broad distributions which we call densities of states (DOS), reported in Fig. 6.1 for the three systems. In case of the bacterium *Rsp. molischianum* the DOS of the α and β BChls of the B850 ring have very similar distributions with the energies of the α BChls slightly smaller than those of the β BChls. This is different for the DOS of the *Rbl. acidophilus* complex. The differences of the two B850 pigments within the building block is much larger.This fact is known as dimerization and its advantages in transport have been discussed theoretically [212]. as well as experimentally [213]. Even if less evident, a similar behavior is found in the B820 ring of the LH3 complex of *Rbl. acidophilus*. The DOSs for the B800 BChls behave very similar for both for LH2 and LH3 complexes of*Rbl. acidophilus*, whereas a different behavior is present in the LH2

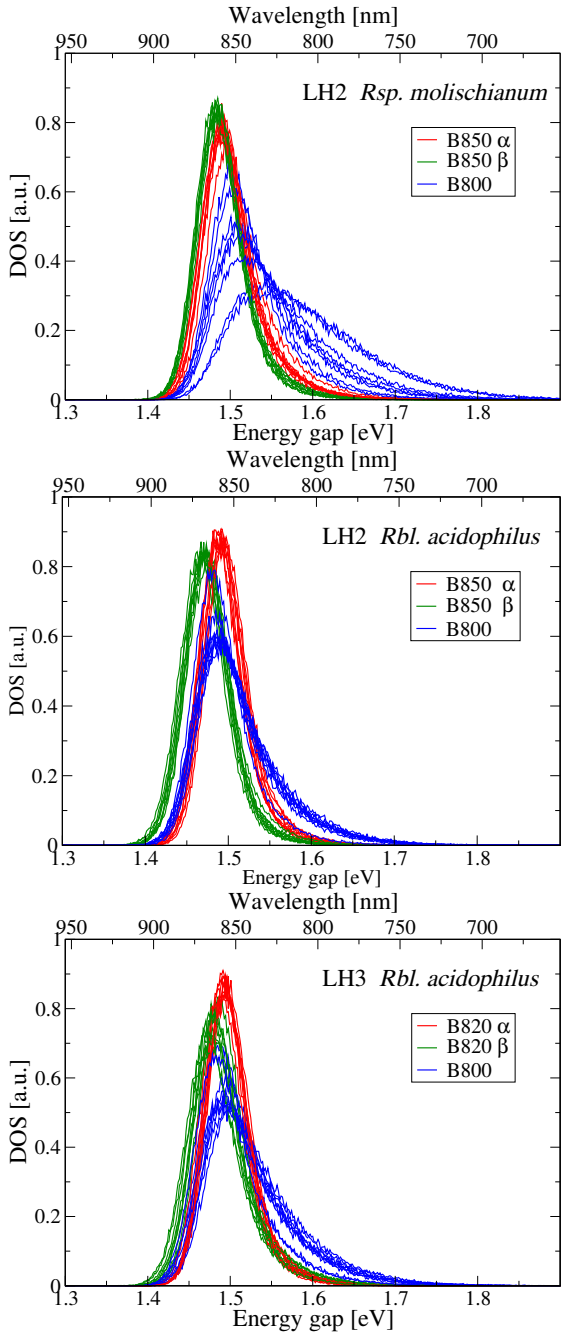

Figure 6.1: Distribution of energy gaps (DOS) between ground and Q_y state for individual BChls for LH2 of *Rsp. molischianum* (top), for LH2 of *Rbl. acidophilus* (center) and for LH3 of *Rbl. acidophilus* (bottom). The B850 (or B820) α, B50 (or B820) β and B800 BChls are displayed in red, green and blue respectively,

complex of *Rsp. molischianum*. The DOSs for the BChls of one kind should be identical. As can be seen in Fig. 6.1, this is not true for the B800 BChls in *Rsp. molischianum*, indicating possible disorder which is not captured by the present approach. This could, e.g., result from slightly different lipids surrounding the pigment and would lead to a disorder usually modeled as static. The static disorder is often assumed to be Gaussian. This certainly shows that the contribution of the environment is non-negligible and modeling only based on a static crystal structure is problematic. Furthermore, the DOSs have an asymmetric shape, visible especially for the B800 rings. This is in agreement with a recent study that demonstrated the electrostatic fluctuations of the protein-water interface might be globally non-Gaussian [214]. The time- and frequency-dependence of the site energies fluctuations can be observed in the energy gap autocorrelation functions and in their Fourier transform (spectral densities) below. The averaged spectral densities are reported in Fig. 6.2. for the B850 (or B820) α BChl, B50 (or B820) β BChl and one B800 BChl. The spectral densities of BChls in one ring, in fact, do overlap because of symmetric properties of the rings and of the same environment around each BChl. Although the general behavior of the spectral densities of the B800 ring is similar to the one of the B850 (or B820), the spectral densities of the B800 ring are easily two times larger than the others, and this feature is independent of the system, even if less evident in the case of the LH3 complex. This difference is due to the larger energies gap fluctuations of the BChls of the B800 ring compared to the ones of the B850 (or B820) ring. The role of the environment is evident in these graphs. We can say that for the case of the BChls of LH2s of *Rsp. molischianum* and *Rh. acidophila* and of LH3 of *Rh. acidophila*, the BChls frequency response comes from the interaction with the environment and not from internal modes. Peaks positions are in fact different for the two rings, with some exceptions in the high-frequency region. However, only the low-frequency region is important in understanding relaxation processes studied in the present work.
Spectral densities, as previously discussed, are obtained from the Fourier transform of the autocorrelation functions. The averaged ones are shown in Fig. 6.3. As expected, the autocorrelation functions of the BChls in the B800 ring are larger than their counterparts in the B850 (or B820) ring. Although the fluctuations of the B800 ring are larger in absolute values, the frequency of the vibrations is the same for the two rings and for the three systems. This is not surprising, since the rings are composed by the same BChl a pigment. The 20 fs period of the oscillations is known to be related to the modes of the C=C and C=O double-bond stretchings [114]. The fast initial decay on a 5 fs time-cale, is also in agreement with our previous findings [126].

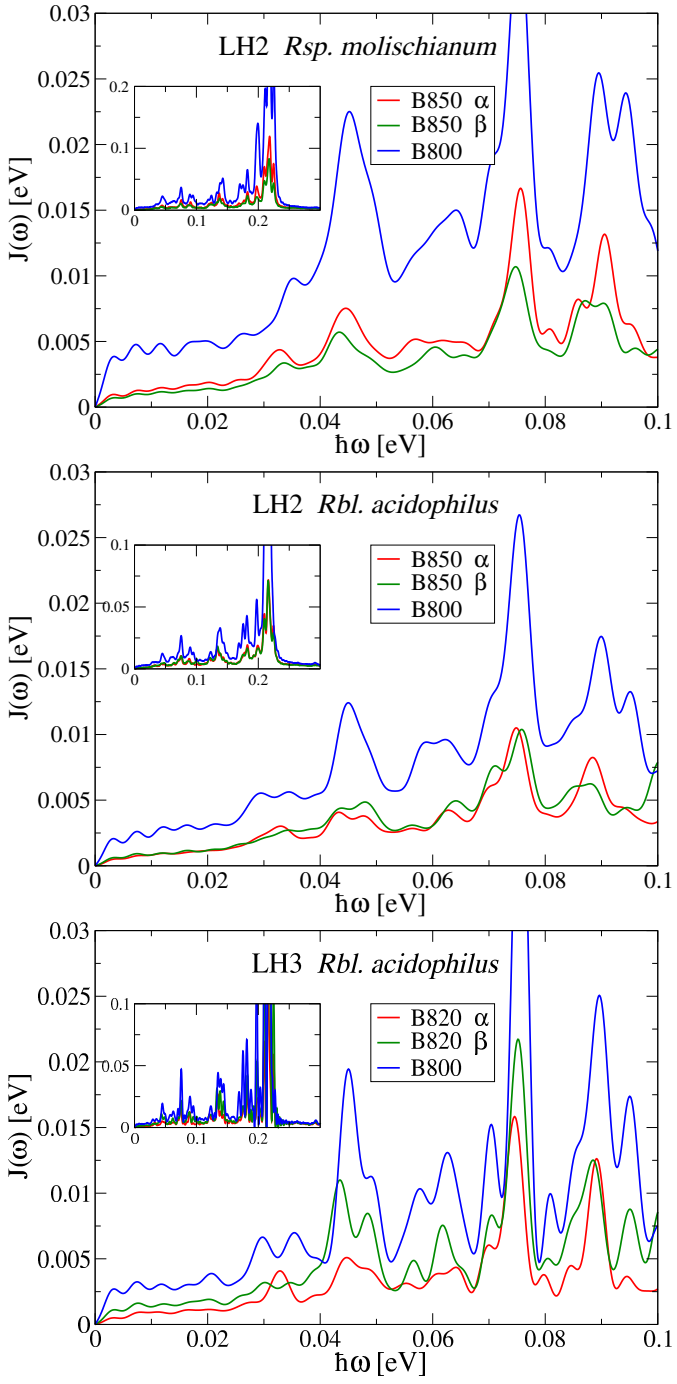

Figure 6.2: Spectral densities for LH2 of *Rsp. molischianum* (top panel), for LH2 of *Rh.) acidophila* (central panel) and for LH3 of *Rbl. acidophilus* (bottom panel). The B850 (or B820) α, B50 (or B820) β and B800 BChls are displayed in red, green and blue respectively.

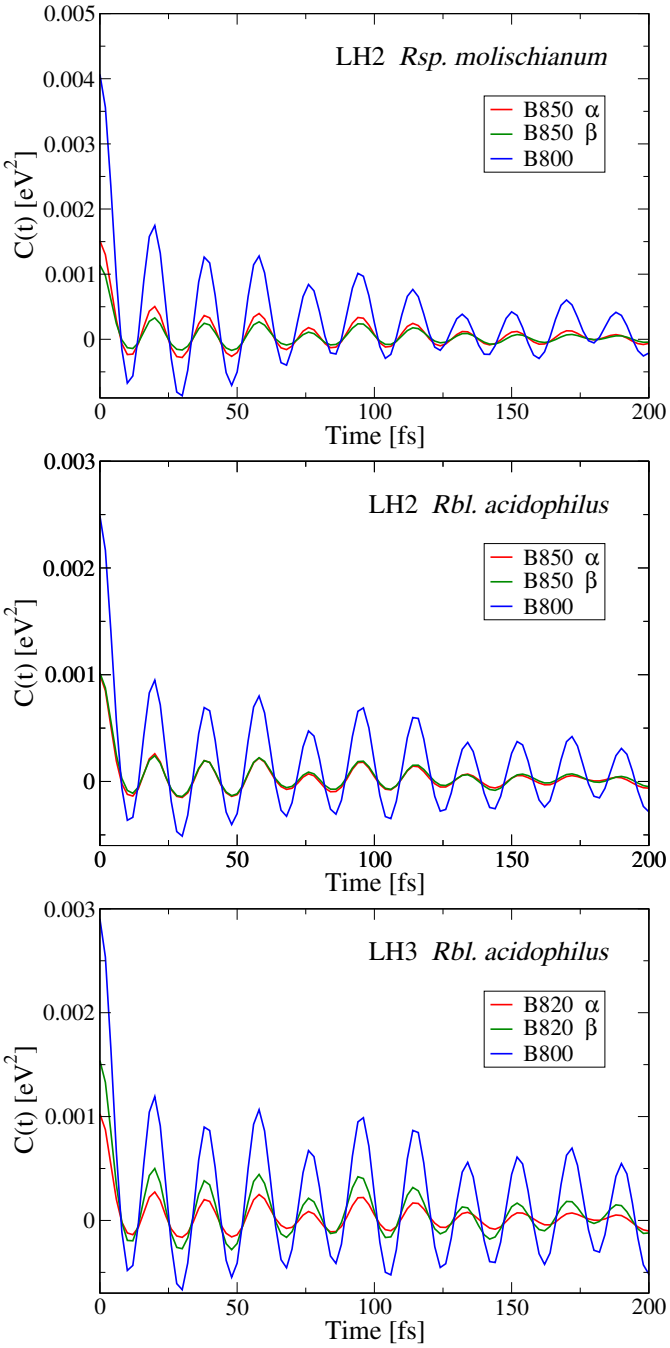

Figure 6.3: Autocorrelation functions for LH2 of *Rsp. molischianum* (top panel), for LH2 of *Rbl. acidophilus* (central panel) and for LH3 of *Rbl. acidophilus* (bottom panel). The B850 (or B820) α, B50 (or B820) β and B800 BChls are displayed in red, green and blue respectively,

Site energies and couplings are combined to build the Hamiltonian in Eq. 6.3, which has been diagonalized at each time step. In this way, excitonic energies have been obtained. The probability in Eq. 6.6 has been then calculated for each pigment of the three systems, for each time step. The results are reported in Fig. 6.4 and Fig. 6.5 for the B850 (or B820) and B800 respectively. In order to have a better statistics, the dynamics has been evalueated for 6000 fs, a reasonable time for the population to decay even in the B800 and it has been averaged over 1000 trajectories per each system. The dynamics in the two rings are completely different. In Fig. 6.4 the population dynamics in the case of the B850 (or B820) ring for the three systems are presented. Due to the configuration of these rings, the pigments are heavily coupled and therefore the exciton is delocalized among them. The exciton takes about 30 fs to leave the excited site, and to reach the first neighbors. Then, as soon as these pigments receive the excitations, they transfer it in a cascade process to their neighbors. Due to different couplings and environments, small differences in time scales of the process are visible for the three systems (Fig. 6.4), but the general behavior of the three systems is rather similar. A different scenario is presented in Fig. 6.5 for the B800 rings of the three systems. It is clear how the population of the excited site takes about 3 ps to decay. This reflects the highly localized feature of the excitons located in this ring: the distance between the BChls is about 21 Å, and the coupling between the BChls is weaker compared to the coupling between the BChls in the other ring.This produce an high localization of the excitons. As a result, if one site is excited, the excitation takes 3 ps to reach the neighboring BChls.

6.4 Conclusions

In this contribution, a theoretical comparison of three different light harvesting systems is proposed. The systems under investigation are the LH2 complexes of the bacteria *Rsp. molischianum* and *Rbl. acidophilus* and the LH3 coomplex of the bacterium *Rbl. acidophilus*. Site energies of individual BChls have been computed and used as a input for the determination of the spectral densities. Then, they have been combined to the coupling to determine the population dynamics along a MD trajectory. The semi-empirical ZINDO/S-CIS method has been used to compute the vertical transition energies, as well as the TrEsp method has been adopted to calculate the coupling between pigments. Site energies DOS are evaluated and compared resulting in a non-perfect Gaussian distributions. Starting from the individual site energies, the autocorrelation function has been computed for each BChl, for each complex. The behavior of the BChls in the B850/B820 ring is

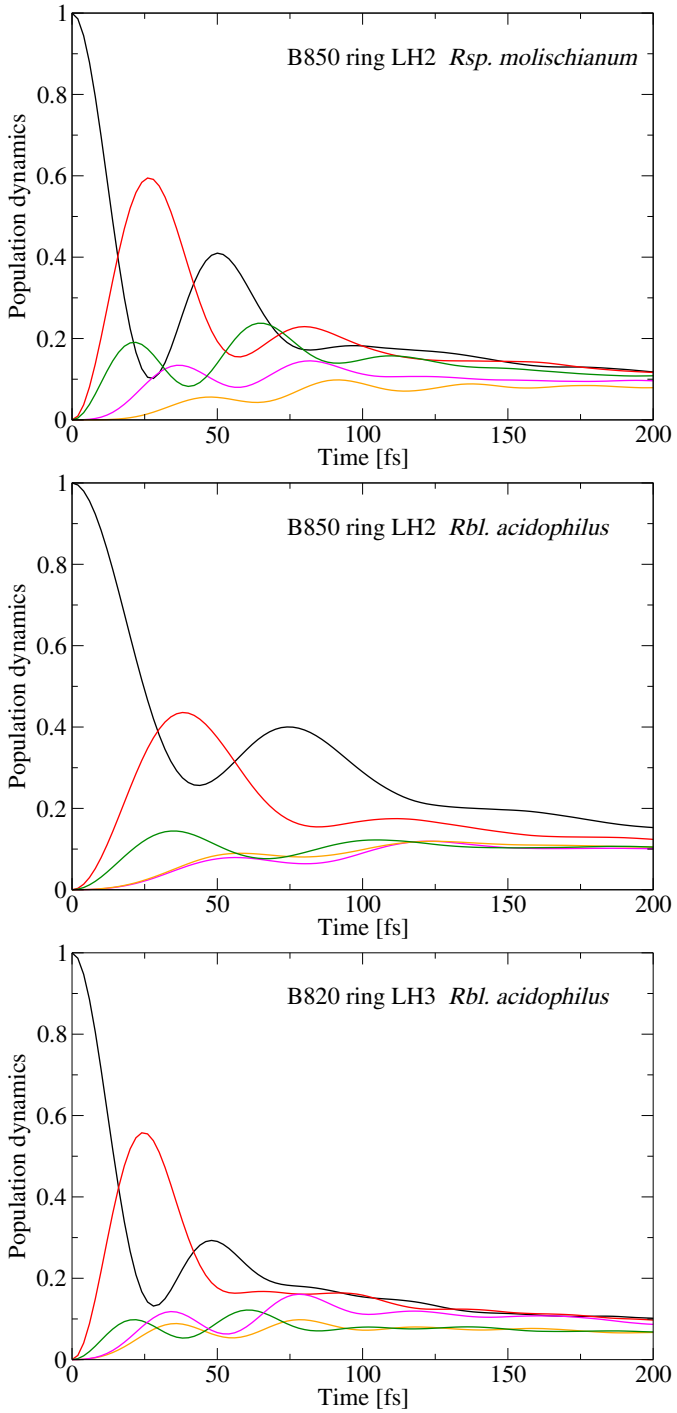

Figure 6.4: Population dynamics for the B850 rings of LH2 of *Rsp. molischianum* (top), of LH2 of *Rbl. acidophilus* (center) and for the B820 ring of LH3 of *Rbl. acidophilus* (bottom).

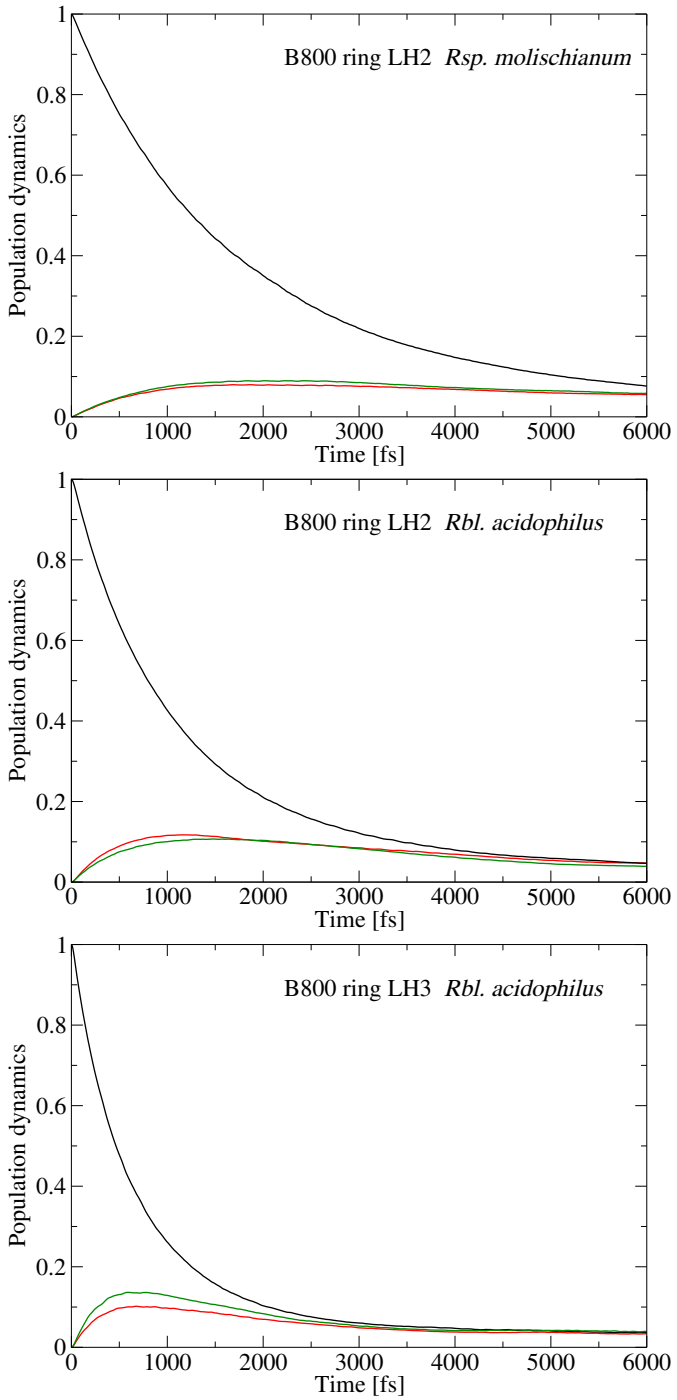

Figure 6.5: Population dynamics for the B800 rings of LH2 of *Rsp. molischianum* (top), of LH2 of *Rbl. acidophilus* (center) and of LH3 of *Rbl. acidophilus* (bottom).

similar for all the systems, and smaller in absolute values respect to their B800 counterparts. Oscillations with a period of about 20 fs are clearly visible and reflect stretchings of heavy atoms. The Fourier transform of the autocorrelation function is denoted as spectral density. As well as for the autocorrelation functions. the B800 ones are larger than the B850 (or B20) ones, even by a factor of two in the low frequency region. However, an assignment of the peaks present in the spectral density is a complicated issue. As a second part of this analysis, the dynamic properties of the three systems have been studied. Starting from the site energies and the couplings, the time-dependent Hamiltonian has been diagonalized for each system at each time step. Then, the probabilty to find an exciton in a particular site has been calculated and populations dynamics for the two rings have been separately computed. A clear difference between the two rings is visible. The decaying time for the population dynamics in the B800 rings is much larger than the one for the B850 (or B820) ring, as a consequence of a weaker couplings between pigments and an higher localization of the exciton in the excited sites. Small differences in the time scales are present in the ring of the same kind of three systems, but the general behavior is similar, as expected due to the presence of the same pigment in the three systems and to the similar environment surrounding it.

Chapter 7

Exciton Transfer in Porphyrin-Metal Organic Frameworks

Ordered arrays of porphyrins can be constructed using metal organic frameworks (MOFs), a class of hybrid compounds which have received enormous attention in the past decades. In this study, the exciton transfer in such porphyrin-MOF has been studied using a combination of various computational techniques. As a first step, the thermal fluctuations in the system have been determined using the ground state DFTB method. Subsequently, the site energies of the porphyrins have been determined along the DFTB trajectory together with the excitonic couplings between the pigments. Similarly to studies on biological LH complexes, the autocorrelation function and the spectral density have been analyzed for each pigment. Based on the site energies and couplings, a time-dependent model Hamiltonian of the system can be constructed and the exciton diffusion through the MOF has been then determined. To this end, the quantum diffusion coefficient (QDC) D has been computed in all three spatial directions. It has been found to be bigger in the inter-layer direction. In addition to these calculations, the QDC has been compared to its classical limit. This comparison shows how strong quantum effects are in enhancing the transfer efficiency of the exciton. The quantum diffusion coefficient is, in fact, considerably larger than its classical counterpart.

This work has been done by M. I. Mallus, M. Addicoat, T. Heine and U. Kleinekathöfer. Task of the author of the present thesis was to perform the ZINDO/S-CIS calculations and to compute site energies, autocorrelation functions and spectral densities Furthermore, the implementation of the TrEsp method (except the calculation of the transition charges), as well as the wave packet dynamic and the D calculations have been part of this thesis work.

7.1 Introduction

Over the last years, the request of phtovoltaic devices has increased enormously. The "standard" devices are formed by inorganic-semiconductors, such as silicon, able to convert the light directly into electricity by the photovoltaic effect. Although silicon-based solar cell are still the most widely used ones, the field of organic solar cells is growing year by year. In this kind of devices, organic polymers or small organic molecules are used for absorbing light and for the charge transport to produce electricity [68]. The simplest organic solar cell is made of a single layer [215], in which the organic active part is embedded between the two conductors. However, bilayer [216] as well as discrete/bulk-heterojunction [217] organic solar cells are used nowadays.
Compared to standard solar cells, organic solar cells are more flexible and cheaper [69]. Nevertheless, the efficiency of such devices have limited their real application. Nowadays, standard solar cells reach values above 40% [218]. On the contrary, a 10% efficiency was obtained only in 2015 for organic solar cells [73]. Another important feature, the stability of the devices [72], has driven the search of organic molecules suitable for such devices. Different organic molecules are used, such as polyacetylene [215], phthalocyanine [219], polyphenilene [220] and poprhyrin [221] molecules. Such molecules are repeated to form polymers. The present work focuses on the latter ones. Porphyrins are organic compounds, composed of four modified pyrroles interconnected via methine bridges (=CH-). Porphyrins can be packed to form columns through which the solar energy under exciton form is transported [221]. These ordered arrays of porphyrins belong to a particular class of compounds called "metal organic framework" (MOF).
MOFs are one-, two- or three-dimensional structures and they are part of the coordination-polymers class, in which single entities are repeated and coordinated to organic ligands [222]. MOFs are essentially composed by a metal ion or a cluster of them and by an organic atom or molecule called "linker". The choice of these two elements determines the properties of the MOF [223]. The MOF studied in the present work is a SURMOF (Surface-grafted MOF) system and it is grown layer-by-layer on a particular substrate, the fluorine-doped tin oxide (FTO), which constitutes the anode of the solar cell. The cathode is composed of a iodine/triiodine electrolyte. Further technical details on the SURMOF and on the characterization of the solar cell are given in Ref. [74].
Aim of the present study is to describe the exciton transfer dynamics in the SURMOF porphyrin-based system realized by Liu et. al. [74]. In order to do so, a multi-scale approach is needed. Differently from the work reported in Chapters

4, 5 and 6, in which the dynamic of the ground state has been obtained through MD simulations, here a ground state Density Functional Tight Binding (DFTB) method is adopted. On top of this trajectory, a quantum-chemical calculation has been performed to obtain the excited states of the porphyrins. The ZINDO/S-CIS method has been employed to this purpose [99].
The discussion on the single pigment calculation is reported in Sec. 7.2.1. It includes site energies, autocorrelation functions and spectral densities for each pigment. The TrEsp method [105] has been used to calculate the coupling between the pigments and the results are presented in Sec. 7.3.2. Site energies and couplings are the building blocks of the system Hamiltonian. Such a Hamiltonian has been built and the ensemble-averaged wave packet dynamics procedure has been employed to evaluate the population dynamics, as discussed in Sec. 7.3.3. In the same Section, the mean squared displacement (MSD) of the exciton and the diffusion coefficient are presented. Conclusions are given in Sec. 7.4.

7.2 Background and Methods

In this Section a brief discussion on the theoretical background and on the computational methods used in this work will be reported. As previously mentioned, a multi-scale approach is adopted to study the optical and the exciton dynamic properties of the porphyrin system.
The standard procedure requires:

- the calculation of the site energies for each pigment;
- the analysis of the autocorrelation function of each pigment, obtained from the energy gap fluctuation, and its Fourier transform, the spectral density;
- the calculation of the interaction between subsystems, i. e. the Coulomb coupling;
- the total Hamiltonian to be built to study the dynamics of the wave packet;
- the definition of a diffusion coefficient, D, in order to evaluate the diffusion properties of the exciton in the lattice made of porphyrins.

The theoretical background needed to understand the single pigment calculation is reported in the next Sec. 7.2.1. The coupling methods and the ensemble-averagede wave packet dynamics approach are presented in Sec. 7.2.2. The results obtained from the simulations are discussed in detail in Sec. 7.3.

7.2.1 Single-Pigment Analysis

The vertical transition between the ground and the first excited state $E_i(t)$, also known as "site energies" of each pigment i together with the coupling between them $V_{ij}(t)$ define the time-dependent Hamiltonian of the system

$$\hat{H}_S(t) = \sum_{i=1}^{N} E_i(t) \left|i\right\rangle \left\langle i\right| + \sum_{\substack{i,j=1 \\ i \neq j}}^{N} V_{ij}(t) \left|i\right\rangle \left\langle j\right| \ . \tag{7.1}$$

Both $E_i(t)$ and $V_{ij}(t)$ are time-dependent entities and therefore they have to be defined for each time step of the trajectory. As a result, in a next step (described in Sec. 7.2.2), the Hamiltonian will be built and diagonalized at each time. In this Section, the functions obtained from the site energies will be discussed. In the present work, the site energies have been calculated using the semiempirical ZINDO/S-CIS approach (Zerner Intermediate Neglect of Differential Orbital method with parameters for spectroscopic properties together with the configuration interaction scheme using single excitations only) [99]. This method is often used for big systems such as light-harvesting systems.
ZINDO/S-CIS has been parametrized for such systems and it is very fast compared to other methods, e. g., some density-functional theory methods (ZINDO requires 5 s to compute a frame, compared to 45 m of computational time if density functional based approaches are used). A more detailed discussion on the site energies was given in Sec. 3.1.1. The properties of the single pigment can be extracted from the analysis of its autocorrelation function $C(t)$ and more importantly from its Fourier transform, the spectral density $J(\omega)$, which describes the coupling between the pigment and its environment. $C(t)$ is defined as:

$$C_{ij}(t) = \langle \Delta E_{ij}(t) \Delta E_{ij}(0) \rangle \tag{7.2}$$

where $\Delta E_{ij}(t) = E_{ij}(t) - \langle E_{ij} \rangle$ denotes the fluctuation of the energy gap $E_{ij}(t)$ between state i and j with respect to its average value $\langle E_{ij} \rangle$. In the present analysis, i and j are the ground and the first excited states, respectively.
The spectral density $J(\omega)$ is defined as:

$$J(\omega) = \frac{\beta\omega}{\pi} \int_0^T dt C(t) \cos(\omega t) \tag{7.3}$$

where $\beta = 1/k_B T$ denotes the Boltzmann's factor. For a more detailed derivation, see Sec. 3.3. Autocorrelation functions and spectral densities have been computed for each pigment and the discussion of the results is given in Sec. 7.3.2.

7.2.2 Coupling and Wave Packet Dynamics

Another important quantity that must be taken into account is the coupling between the pigments V_{ij}. In fact, this quantity is needed, together with the site energies, to build the system Hamiltonian in Eq. 7.1 used to propagate the exciton wave functions and to define the diffusion coefficient of the system.
The method used in this work to calculate the coupling between pigments is the so-called TrEsp (Transition charges from Electrostatic Potential) method [105]. This method calculates the Coulomb coupling between the partial transition charges q_m^T in pigment i and q_n^T in pigment j. Namely:

$$V_{ij}^{TrEsp} = \frac{f}{4\pi\epsilon_0} \sum_{m,n} \frac{q_m^T \cdot q_n^T}{\mid \boldsymbol{R}_m - \boldsymbol{R}_n \mid} \tag{7.4}$$

where f denotes a screening distance-dependent factor, $\mid \boldsymbol{R}_m - \boldsymbol{R}_n \mid$ the distance between the two partial charges and the sum goes over all the atoms in the two pigments. A detailed explanation of the TrEsp method, as well as other methods such as the PDA approximation used to calculate the coupling term of the Hamiltonian were given in Sec. 3.1.2. The coupling values for the porphyrins are listed in Tab. 7.1. The couplings represent the off-diagonal elements of the Hamiltonian of the system (Eq. 7.1), while the site energies are the diagonal ones. Such a Hamiltonian can be built and the Schrödinger equation can be solved in order to propagate the system wave function $\Psi_S(t)$ to obtain the population dynamics [85]:

$$i\hbar \frac{\partial \Psi_S(t)}{\partial t} = H_S \Psi_S(t). \tag{7.5}$$

The wave function $\Psi_S(t)$ can be expressed as a linear comination of the $|\mu\rangle$ excitonic states of the system, $|\Psi_S(t)\rangle = \sum_\mu c_\mu(t)|\mu\rangle$. Furthermore, each excitonic state can be expanded in the basis of the local m sites:

$$|\mu\rangle = \sum_m c_m^\mu |m\rangle. \tag{7.6}$$

These steps are needed to obtain the population dynamics, which represents the probability $P_m(t)$ at each time step to find the exciton wave packet in a particular pigment m

$$P_m(t) = |\langle m|\Psi_S\rangle|^2. \tag{7.7}$$

By calculating this probability, it is possible to observe the evolution of the population of each site on time, i. e. the "population dynamics". Nevertheless, the population dynamics itself can not fully describe the excitation energy transfer properties of a system. In fact, to estimate the transport efficiency, the diffusion

coefficient $D(t)$ must be computed and analyzed. It is in general defined as the time derivative of the mean squared displacement $\langle x(t)^2 \rangle$ (MSD) of the diffusing particle, by solving the diffusion equation. The MSD is defined as:

$$\langle x(t)^2 \rangle = \sum_m P_m(t) R_m^2 \tag{7.8}$$

where $P_m(t)$ denotes the probability (given in Eq. 7.7) and R_m the distance between pigment m and the excited pigment i. It is assumed that $P_i(t = 0) = 1$, i. e., at time $t = 0$ only pigment i is excited. The diffusion coefficient $D(t)$ is then obtained as:

$$D(t) = \frac{d\langle x(t)^2 \rangle}{dt}. \tag{7.9}$$

As suggested by Dutta and Bagchi [224], the definition of $D(t)$ in Eq. 7.9 can be compared to its classical limit. For a one-dimensional random walk, D can be in fact written as [225]:

$$D = \sum_m \frac{k_m}{2} R_m^2 \tag{7.10}$$

where k_m denotes the rate constant of site m. This comparison is important to estimate the quantum effects in the exciton transport. The rate constant can be expressed in terms of the coupling corelation function $C_V(t)$ [224]:

$$k_m = \frac{2}{\hbar^2} \int_0^\infty dt C_V(t) = \frac{2}{\hbar^2} \int_0^\infty dt \langle V_{im}(t) V_{im}(0) \rangle. \tag{7.11}$$

where i denotes the excited pigment and m a generic pigment of the system. To compute it, an exponential decay for the coupling autocorrelation function has been assumed:

$$\langle V_{im}(t) V_{im}(0) \rangle = V_{0m}^2 e^{-b_m t}. \tag{7.12}$$

By using these approximations, Eq. 7.11 becomes

$$k_m = \frac{2V_{0m}^2}{\hbar^2 b_m}. \tag{7.13}$$

The two definitions of the diffusion coefficient, reported in Eqs. 7.9 and 7.10 have been computed and then compared. The results are given in Sec. 7.3.3.

7.3 Results

In this Section, the results obtained from the simulations wiill be presented and analyzed. The discussion starts with the description of the system setup in Sec. 7.3.1 and continues with the results on the analysis on the single pigments, which includes the site energies and their DOSs, the autocorrelation funcions and the spectral densities, in Sec. 7.3.2. The couplings, the population dynamics, the MSD and the diffusion coefficient are given in Sec. 7.3.3.

7.3.1 System Setup

As a starting point for the site energies calculation, the unit cell has been analyzed. It is composed by four identic pigments as shown in Fig. 7.1. The lattice vectors

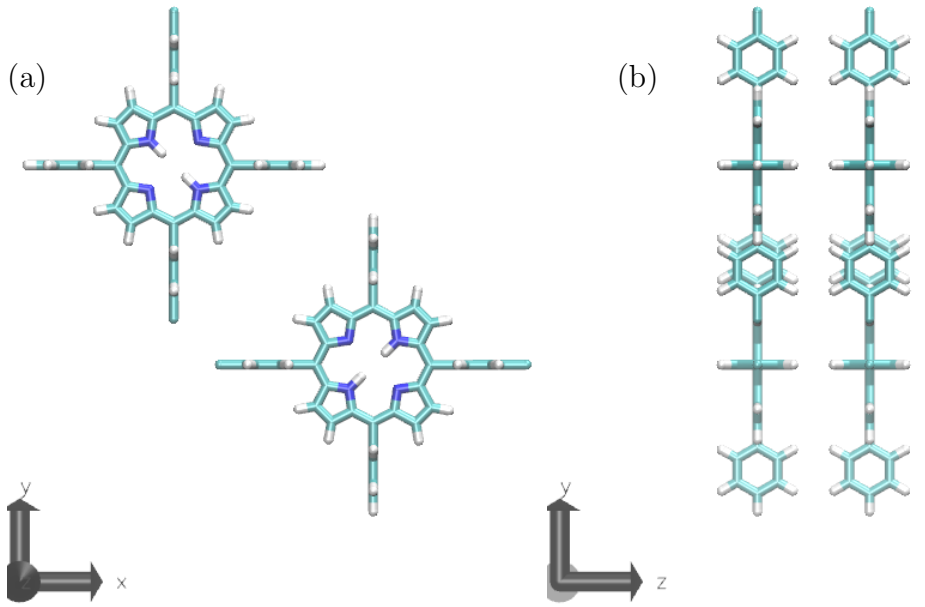

Figure 7.1: Front (a) and side (b) views of the unit cell composed by four porphyrins. The figures were obtained using the VMD program [43].

are a = 23.9620 Å, b = 23.9621 Å and c = 13.4922 Å for the x, y and z axes respectively. The porphyrins in the same z-plane are differently oriented, as it can be seen in Fig. 7.1. Even if they are chemically identic, the dynamics of the ground state was performed for the four pigments independently. The site energies calculations therefore, have been performed for every pigment of the unit cell. The ZINDO/S-CIS approach described previously in Sec. 3.1.1 has been employed to calculate the vertical transitions from the ground to the first excited state for each pigment. The semi-empirical method has been applied in a QM/MM framework (see Sec. 3.1.1). To perform a good QM/MM calculation, a symmetric and big enough classic environment is needed in order to avoid boundary effects due to the small size of the unit cell. Several copies of the unit box are therefore needed. The configuration used to perform the site energies calculation is shown in Fig. 7.2. It consists of $3 \times 3 \times 4$ unit cells. The configuration shown in Fig. 7.2 has been created for each pigment in the unit cell, in order to place each of them at the center of the final structure, to create a fully symmetric environment around that

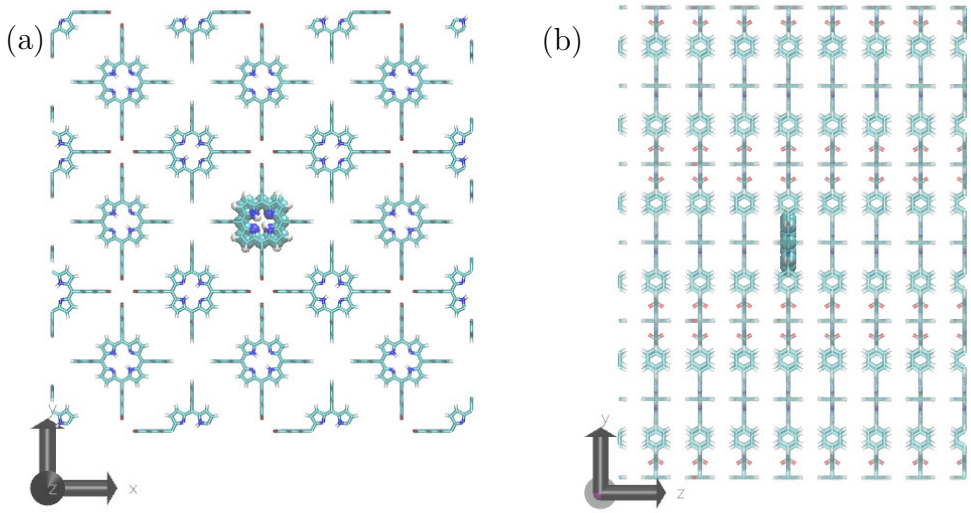

Figure 7.2: Front (a) and side (b) views of the final configuration adopted for the site energies calculation. One of the pigment of the unit cell is placed in the center of the structure. The figures were obtained using the VMD program [43].

pigment. Differently from the case of the other LH systems studied in Chapters 4, 5 and 6 the classic environment in this case is made of other pigments instead of water, protein or lipids. Therefore, we expect a different frequency response to the thermal vibrations of the environment.
A different configuration with respect to the one presented above in Fig. 7.2, has been adopted for the coupling calculations and for building the Hamiltonian to evaluate population dynamics and diffusion coefficient. As it will be explained in the next Sec. 7.3.3, the diffusion coefficient was found to be significant along the z-axis only. Due to this reason, to save computational time, the unit box was copied only in the z direction. It resulted in $1 \times 1 \times 2$ boxes, i. e., a four-layers structure, with two porphyrins per z-layer. This final configuration is shown in Fig. 7.3.

7.3.2 DOS, Autocorrelations and Spectral Densities

The energy gaps between ground and first excited states have been computed for each pigment independently and their fluctuations over time as well as their density of states are depicted in Fig. 7.4. Site energies have been calculated on top of a DFTB+ trajectory [226], performed at 300K and for 300 ps, with a 1 fs time

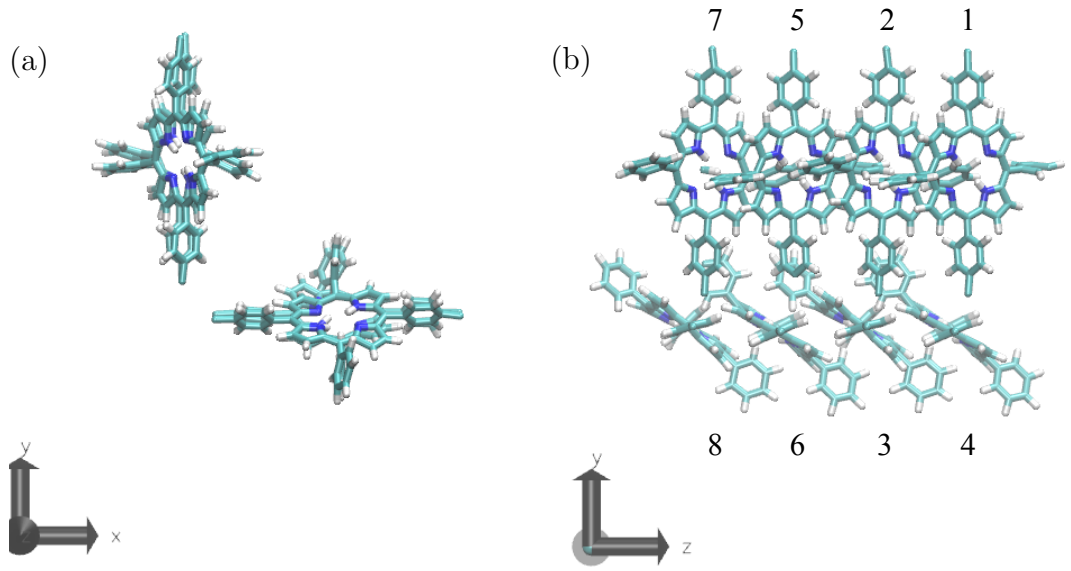

Figure 7.3: Front (a) and side (b) views of the final configuration adopted for the coupling calculations. Numbering of porphyrins is showed in panel (b). The figures were obtained using the VMD program [43].

step, for a total of 300.000 snapshots. The structure setup has been previously shown in Fig. 7.2. As can be seen in Fig. 7.4, the four sites behave quite similarly,

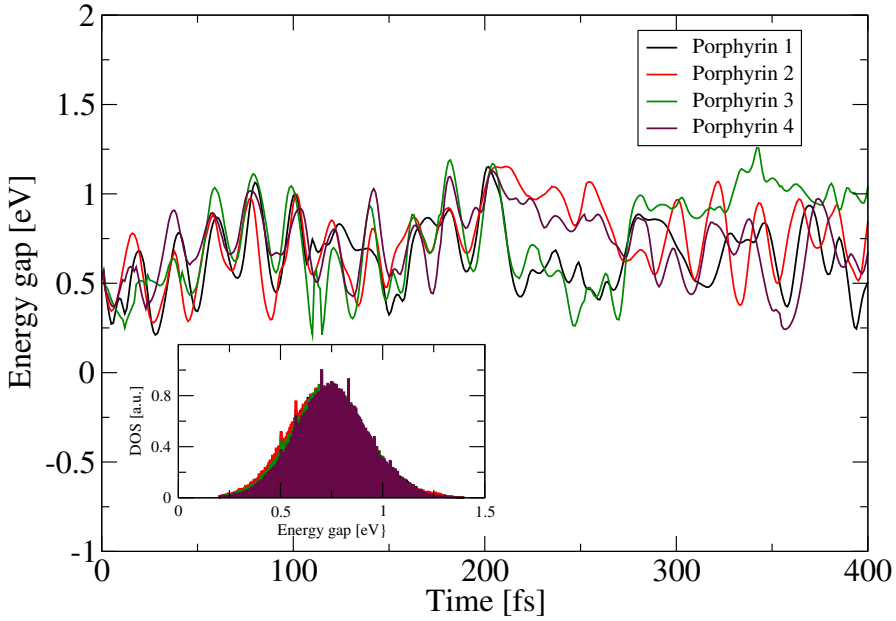

Figure 7.4: Energy gaps fluctuations over time for the four pigments, for the first 400 fs of the trajectory. The densities of states are depicted in the inset.

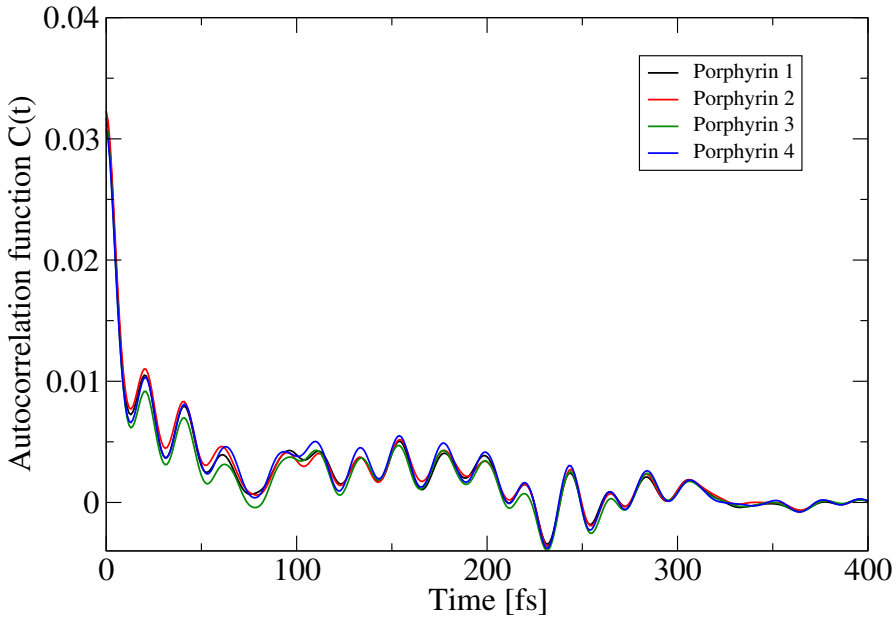

Figure 7.5: Autocorrelation functions for the four poprhyrins present in the unit box.

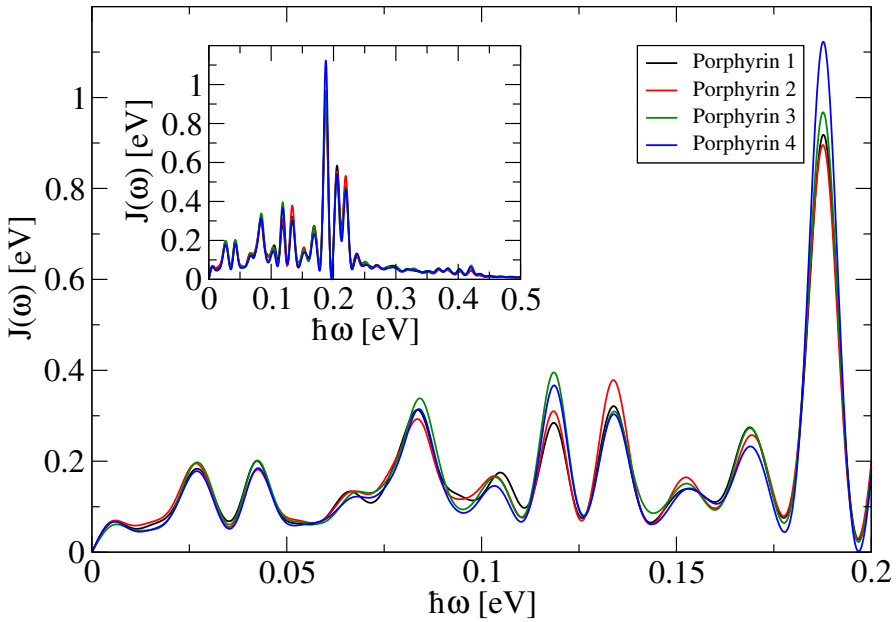

Figure 7.6: Spectral densities for the four poprhyrins present in the unit box.

as expected, since they have the same chemical structure and are surrounded by the same environment. The distributions of the density of states (DOS), reported in the inset of Fig. 7.4, are symmetric and Gaussian for the four pigments, with some exceptions represented by the peaks in the inset of Fig. 7.4. In general (e. g. see Chapter 6) these distributions show a non-Gaussian tail, which is absent here.

This can be due to the different nature of the classical environment with respect to the "standard" present in the systems previously studied. The force-field, as showed by Chandrasekaran et. al., for the case of the FMO complex [144], can also play a role in determining the shape of the DOS and in turn, the behavior of the spectral densities. Having computed the site energies, the four autocorrelation functions and spectral densities can be built by using Eqs. 7.2 and 7.3. They are reported in Fig. 7.5 and Fig. 7.6, respectively. A similar behavior of the four DOS is reflected in a similar form for both autocorrelation functions and spectral densities for the pigments in the unit box (Fig. 7.5 and Fig. 7.6) The first initial decay of the autocorrrelation functions is in agreement with the 5 fs time-scale obtained for the similar pigment BChl a of other LH complexes previously analyzed (see Chapter 4). On the contrary, the absolute value of the oscillations is one order of magnitude bigger than the one of the case of LH2, for example, as showed in Chapter 4. Again, this can be due to the environment, composed in this case, by "copies" of the pigment under study. The spectral density describes the frequency-dependent coupling between the pigment and its environment (see Sec. 3.3). Since in this special case the environment is composed by copies of the pigments, a calculation without point charges (pc) has been performed to see if internal or external modes determines the behavior of the single pigment. As an example, the case of porphyrin 1 is shown in Fig. 7.7. The system response does not depend on the bath fluctuations: the frequency response is due to the internal modes. A similar behavior was found for the PE545 complex by Aghtar et. al. [66].

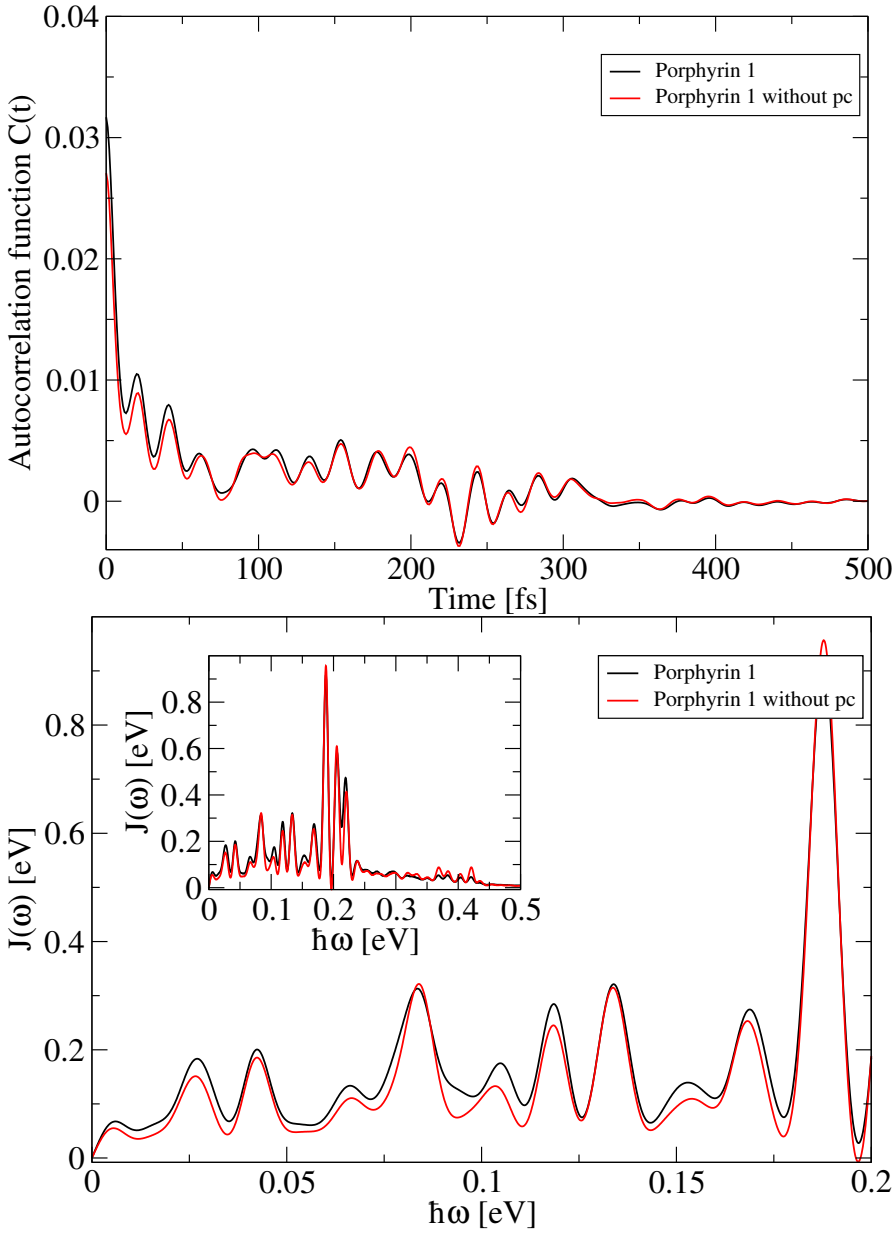

Figure 7.7: Autocorrelation function (top) and spectral density (bottom) in the case of presence and absence of point charges in the MM region. Reported, as example, is the case of Porphyrin 1 of the unit cell.

7.3.3 Coupling, Population Dynamics and Diffusion Coefficient

As the second part of this work, the coupling between pigments has been computed by means of Eq. 7.4. In order to do so, the unit cell has been copied different times, similarly to the case of site energies, but with the configuration shown in Fig. 7.3. This structure has been adopted to save computational cost, since the

diffusion coefficient in the x-y plane was found to be negligible with respect to the one in the z-direction, where the different layers have been placed. The poprhyrins are numbered according tothe porphyrins ID (P. ID) reported in Fig. 7.3. The layers are enumerated in the z-increasing direction.

P. ID	1	2	3	4	5	6	7	8
1		62.9	-1.4	-7.7	8.4	3.0	3.0	1.5
2	62.9		-5.0	-6.3	54.1	-0.7	13.3	1.2
3	-1.4	-5.0		44.4	-4.5	55.3	-2.2	11.4
4	-7.7	-6.3	44.4		-3.3	5.4	-1.5	1.1
5	8.4	54.1	-4.5	-3.3		-7.7	62.9	-1.4
6	3.0	-0.7	55.3	5.4	-7.7		-6.3	44.4
7	3.0	13.3	-2.2	-1.5	62.9	-6.3		-5.0
8	1.5	1.2	11.4	1.1	-1.4	44.4	-5.0	

Table 7.1: Average coupling values for the four-layers system [10^{-4} eV].

The transition charges in Eq. 7.4 were computed by using the Multi-Wave Function (MultiWFN) tool [106]. The porphyrin structure was optimised using PBE/6-311++g(2d,p) in Gaussian09. Then the lowest 5 excited states (either singlets or triplets) were calculated using TD-DFT (same functional and basis set). All excitations with coefficients larger than 0.00001 were counted. The transition charges corresponding to the excitations with the highest oscillator strength were calculated using MultiWFN 3.3.7. The coupling between the pigments composing the four-layer structure have been calculated for each time step of the trajectory. The couplings averaged over time and reported in Tab. 7.1. As can be seen in Tab. 7.1, the couplings between porphyrins with same x-y coordinates are stronger than the others. This is a first indication of the diffusion coefficient to be bigger in the z-direction than in the other two directions.
In order to compute the population dynamics and the diffusion coefficient, the Hamiltonian has been built and diagonalized for each time step. The ensemble-averaged wave-packet dynamics method is employed (see 3.4) to this end. The population dynamics has been computed for 10 ps, and averaged over 300 trajectories. As initial configuration, the probabilty to find the exciton at time $t = 0$ is assumed to be 1 in pigment 1. Starting from this initial condition, the time evolution operator is applied to the wave function and Eq. 7.7 is computed. In the rest of the discussion, the diffusion is analyzed in terms of z-layers, as it should be clear by looking at Tab. 7.1 that the couplings in the x-y plane are too small

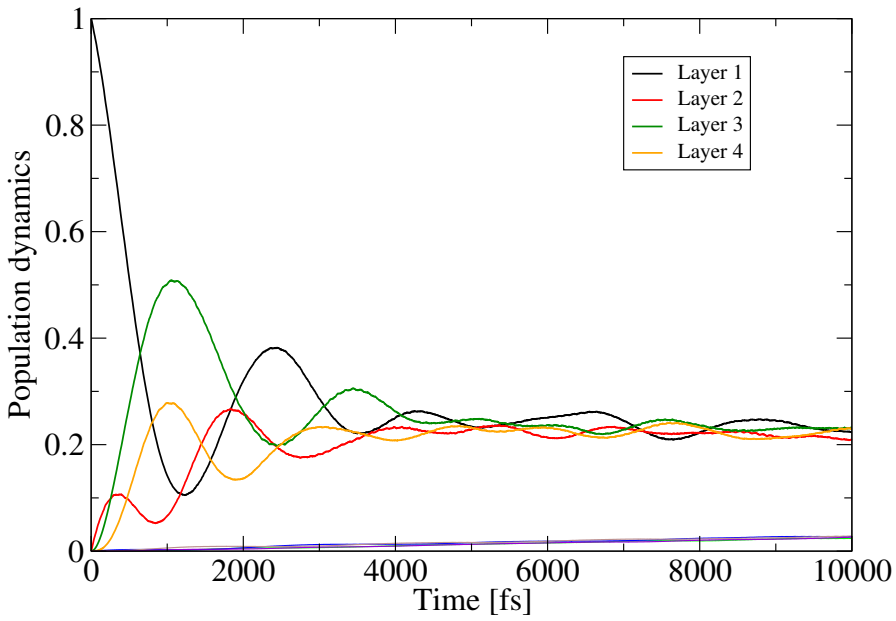

Figure 7.8: Population dynamics in the four layers poprphyrin-based MOF system.

to allow the diffusion in the x-y plane. It is interesting to see how the population, initially located in the first layer, is spread into the lattice. This can be seen in Fig. 7.8. The exciton arrives at layer 2 first, because it is the closest one and therefore the most higly coupled to the excited layer 1. However, as soon as the layer 2 gets excited, the excitation is transmitted to the layers 3 and 4 due to the strong coupling between these layers. In fact, as it can be seen in Tab. 7.1, the layer 3 receives contributions both from layers 1 and 2, which explains why the population in this layer reaches the big value reported in Fig. 7.8 The lower populations in Fig. 7.8 correspond to the populations in porphyrins in layers shifted in the x and y directions. These layers, as expected, never get populated. The non-zero values of the population in these layers can be explained as a drawback of the ensemble-averaged wave-packet dynamics method, which can not reach appropriate thermal equilibrium distributions at long-time scales [85]. For the same reason, at time t = 4 ps the four layers are equally populated. Starting from these considerations, the MSD and the diffusion coefficent have been computed and reported in Fig. 7.9. The result show how important quantum effects are in enhancing the diffusion of the exciton. As it can be seen in Fig. 7.9, at short timescale, the quantum diffusion coefficient is much higher than its classical value of D=0.012Å^2/fs. The long-time values of the diffusion coefficient are not taken into account in this consideration since after 4 ps there is no diffusion, as can be seen also in the population dynamics reported in Fig. 7.8. A similar study on diffusion coefficient has been performed by Fujita and co-workers [227] for the chlorosome

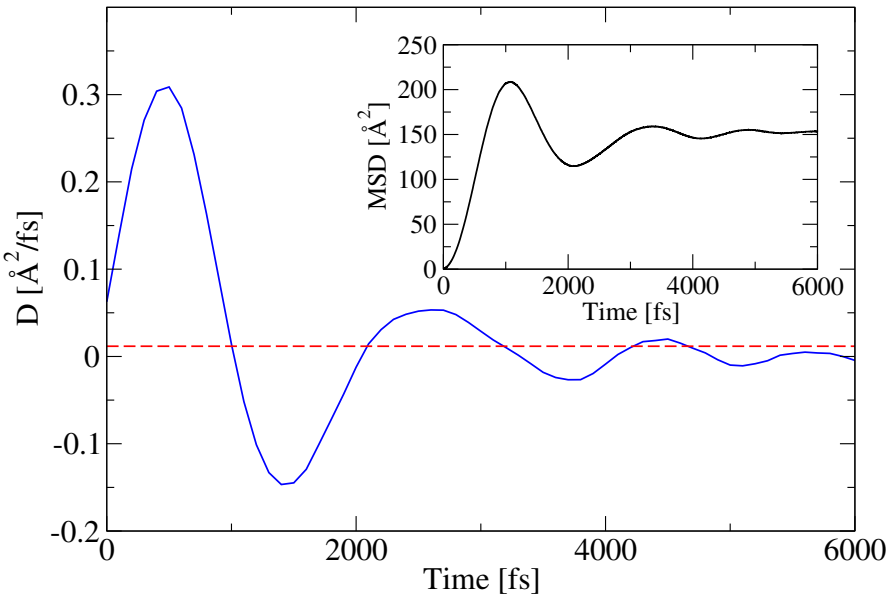

Figure 7.9: Diffusion coefficient obtained by the derivative of the MSD (blue line) and its classical limit (red-dashed line). The inset shows the MSD.

system. Similarly to the case of the present work, the authors computed the diffusion coeffcient and found a privileged direction for the exciton transport.

7.4 Conclusions

The SURMOF-porphyrin based system has been studied in the present work and the exciton diffusion has been analyzed. Starting from a DFTB trajectory, the ZINDO/S-CIS method has been employed within a QM/MM framework to compute the site energies and their distribution, DOSs. These DOSs result in a very symmetric Gaussian-like distributions, and they behave quite similar for the four pigments under study.

Autocorrelation functions and spectral densities have been analyzed as well for each pigment of the unit cell. Again, it can be concluded, as expected, that the pigments behave similarly. In addition to that, it has been shown how the internal modes are responsible for the single-pigment behavior, by comparing autocorrelation functions and spectral densities in case of presence and absence of point charges in the MM region.

In a second step, couplings have been evaluated and the total Hamiltonian of the system has been built to study the exciton transfer. From the joint analysis of coupling values and population dynamics, it can be concluded that the exciton

moves in the z-axis only, the inter-layer direction. These findings have been used as a input for the calculation of the diffusion coefficient, which has been compared to its classical limit. As a result, it has been found that quantum effects are important in enhancing the diffusion of the exciton in the porphyrin lattice.
However, it must be mentioned that this analysis is not complete yet. In fact, only the exciton Hamiltonian has been considered to analyze the diffusion properties among the porphyrin lattice. Due to the small inter-layer distance (about 6 Å), charge transfer effects could have an important role and a mixed exciton-charge Hamiltonian should be considered to take into account all the possible physical processes. A similar work was proposed for the organic semiconductor Dinaphtho[2,3-b:2'3'-f]thieno[3,2-b]-thiophene (DNTT) by Fujita and co-workers [228], and we are currently working in this direction to improve the results already obtained.

Chapter 8

Conclusions

Light-harvesting (LH) processes occurring in plants, algae and bacteria have attracted the attention of the scientists for many years. Photosynthesis is a cascade-process, in which the energy captured by the harvesting pigment is transferred to different compounds until charge separation is reached [2]. Although the process is now well understood at molecular and atomic details, from both experimental and theoretical point of views, we cannot recreate the light-harvesting process with same efficiency and stability in artificial systems yet [1]. This is mainly due to the different time-scales involved and to the fact that both quantum and classical phenomena seem to play a role contemporaneously [77].

Aim of the present thesis was to contribute to clarify the role of one of the timescales involved in the energy-transfer process, the dephasing time (Chapters 4 and 5), to study the excitation energy transfer phenomena in different LH systems (Chapter 6) and to describe the exciton-diffusion process in a bio-inspired artificial system (Chapter 7).

To this end, computer simulations have been performed and a combined quantum-classical approach has been employed. Molecular dynamics simulations have been performed for each system under study, to obtain thermal fluctuations of the ground states of each pigment composing the complex. The semi-empirical method ZINDO/S-CIS [99] has been employed in a QM/MM framework to calculate site energies fluctuations and their distributions, the density of states. These distributions have been analyzed and in a second step used to build autocorrelation functions and spectral densities for each site. In this way, information on the influence of the environment have been studied [109]. Coulomb coupling among pigments has been evaluated as well by employing the TrEsp method [105] and used, together with the site energies, to build the time-dependent Hamiltonian of the system. Such Hamiltonian has been used to apply the ensemble-averaged wave-packet dynamics approach to quantitatively estimate the exciton transfer

properties of the LH systems [85].

In the first part of the thesis, the dephasing phenomenon has been studied in detail. Such phenomenon must be analyzed in order to understand the quantum nature of the excitation-energy transfer process, and its efficiency in particular. Starting from the site energies fluctuations, an analytic method has been developed to relate such fluctuations to the dephasing time of each pigment. Such method is based on the relation firstly found by Akimov and Prezhdo in 2013 [75]. The method has been applied to a large set of data, which includes LH2 [151], FMO [143, 144], PE545 [66], DNA [145], DNA Photolyase [146] and Cryptochrome [147] complexes. It has been shown how the relation between the two quantities was universal and independent from system and method used in the simulations [126]. Moreover, it was shown how the autocorrelation function of the single pigment can be seen as its "molecular fingerprint": in fact, it determines the dephasing properties of the pigment itself. Subsequently, the method was extended to the study of the whole LH complexes. The study was applied to the case of the LH2 [151] complex, the FMO trimer [143, 144], the PE545 system [66] as well as the PE555 aggregate [165]. In this case, the relation refers to the excitonic gaps and even to the neighboring gaps. Again, it was possible to conclude that the relation between dephasing time and excitonic gap fluctuation was still valid, with the same universality feature. The autocorrelation functions play a role in determining the proportionality constant of such relation.
This work on dephasing processes can be seen as a starting point in understanding dephasing-relate phenomena, and it can serve as a input of further theoretical studies, such as the surface hopping method [163, 164].

The second part of the present thesis was focused on the study of the environmental effects on three similar LH complexes, the LH2 complexes of the purple bacteria *Rhodospirillum molischianum* [45] and *Rhodoblastus acidophilus* [201]. and the LH3 complex of *Rhodoblastus acidophilus* [42]. These three systems are composed of the same kind of pigment, the bacteriochlorophyll a (BChl a). However, the number of pigments, as well as absorption bands and environments are slightly different. These variations make the comparison between them an interesting analysis. The results show how these effects can lead to differences in the coupling between pigments, in the interaction with the environment and in the exciton transfer dynamics.

As the final part of the present work, the porphyrin-based MOF system was

studied. This system was created and used to build an organic solar cell by Liu and co-workers in 2015 [74]. In the present thesis, simulations have been performed to understand the exciton diffusion in the porphyrin lattice. Similar to what has been done for the other LH complexes, site energies have been computed for each pigment by using the ZINDO/S-CIS method on top of a DFTB trajectory. Autocorrelation functions and spectral densities have been analyzed, resulting in the primary role of internal modes in determining the frequency-response of the system. The site energies were subsequently combined to coupling studies (again, by employing the TrEsp method) to compute the time-dependent Hamiltonian of the system, used as a input of the ensemble-averaged wave-packet dynamics method. The diffusion coefficient was finally analyzed. In particular, thanks to the comparison between classical and quantum definitions of the diffusion coefficient, it was possible to show the importance of quantum effects in the exciton transport. However, we plan to extend this last study in order to consider charge-transfer (CT) effects, which might occur in the system due to its configuration. A similar work has been proposed by Fujita et. al. [228] for the case of the Dinaphtho[2,3-b:2'3'-f]thieno[3,2-b]-thiophene (DNTT) thin films, a type of organic semiconductor recently introduced [229]. To this end, a mixed exciton-charge transfer Hamiltonian must be built to include the two physical phenomena occurring in the system, relate to the presence of mixed CT states and Frenkel excitons [227].

Due to the computational cost associated to the theoretical study of the LH systems, many approximations are, in general, adopted and possible future advancements strongly depend on their accuracy and consistency. Rosnick and Curutchet, for example, recently proposed a study to overcome the so-called "geometry mismatch" problem due to the use of low-quality structures obtained via MD simulations [154]. A full-quantum description of the LH systems is not possible in a dynamic picture yet, but it has been already proposed for a static configuration [100]. These drawbacks, however, hardly concern the actual computational resources and algorithms. Future applications and improvements will necessarly pass through the implementation of the quantum-chemistry methods in a more sophisticated fashion, in order to design artificial LH complexes able to mimic the nature.

As an extension of this work, we are currently working on a chromatophore system [230]. Chromatophores are cells, or group of cells, containing the LH complexes. They are composed of about 200 protein complexes, where the number de-

pends on the organism: 60-100 LH2 complexes, 10-20 LH1-RC complexes, 1 ATP-synthase, and 5-10 Cytochrome b-Cytochrome c_1 complexes. The specific system under study is the chromatophore of the bacterium *Rhodobacter sphaeroides*. The simulation box is composed of 70.462.162 atoms, and it is the largest simulation of a LH complex. The aim of the work will be to perform the quantum-chemistry calculations on top of a MD trajectory already performed, to evaluate the exciton transfer properties of the system. The site energies calculations for the 1701 pigments of the 63 LH2 systems have already been performed by the author of the present thesis, and we plan to analyze differences in the site energies distributions as well as in the autocorrelation functions and spectral densities. In future, the LH1-RC complexes will be studied as well, aiming to evaluate the transfer properties among the different LH complexes of the chromatophore.

Bibliography

[1] R. E Blankenship. *Molecular mechanisms of photosynthesis.* Blackwell Science, Oxford, 2008.

[2] R. Govindge. Primary Events in Photosynthesis. *Sci. Am.*, 231:68–82, 1974.

[3] J. J. Eaton Rye, B. C. Tripathy, and T. D. Sharkey. *Photosynthesis: Plastid Biology, Energy Conversion and Carbon Assimilation. Advances in Photosynthesis and Respiration*, volume 34. Springer, The Netherlands, 2012.

[4] N. Hunter, F. Daldal, M. C. Thurnauer, and J. T. Beatt. *The Purple Phototrophic Bacteria. Advances in Photosynthesis and Respiration*, volume 28. Springer, Netherlands, 2009.

[5] E. G. Nisbet and N. H. Sleep. The Habitat and Nature of Early Life. *Nature*, 409:1083–1091, 2001.

[6] R. Emerson and W. Arnold. The Photochemical Reaction in Photosyntheis. *J. Gen. Physiol.*, 16:191–205, 1932.

[7] W. Arnold and H. I. Kohn. The Chlorophyll Unit in Photosynthesis. *J. Gen. Physiol.*, 18:109–112, 1934.

[8] K. Wohl. The Mechanism of Photosynthesis in Green Plants. *New Phytol.*, 39:33–64, 1940.

[9] J. F. Hill and Govindjee. The Controversy over the Minimum Quantum Requirement for Oxygen Evolution. *Photosynth. Rev.*, 122:97–112, 2014.

[10] R. K. Chain and D. I. Arnon. Quantum efficiency of photosynthetic energy conversion. *Proc. Natl. Acad. Sci. USA*, 74:3377–3381, 1977.

[11] S. Georgakopoulou, R. N. Frese, E. Jonson, C. Koolhaas, R. J. Cogdell, R. van Grondelle, and G. van der Zwan. Absorption and CD spectroscopy and modeling of various LH2 complexes from purple bacteria. *Biophys. J.*, 82:2184–2197, 2002.

[12] V. I. Novoderezhkin and R. van Grondelle. Physical origins and models of energy transfer in photosynthetic light-harvesting. *Phys. Chem. Chem. Phys.*, 12:7352–7365, 2010.

[13] G. S. Engel, T. R. Calhoun, E. L. Read, T. K. Ahn, T. Mancal, Y. C. Cheng, R. E. Blankenship, and G. R. Fleming. Evidence for Wavelike Energy Transfer Through Quantum Coherence in Photosynthetic Systems. *Nature*, 446:782–786, 2007.

[14] H Lee, Y-C Cheng, and GR Fleming. Coherence Dynamics in Photosynthesis: Protein Protection of Excitonic Coherence. *Science*, 316:1462–1465, 2007.

[15] D. Beljonne, C. Curutchet, G. D. Scholes, and R. J. Silbey. Beyond Förster Resonance Energy Transfer in Biological and Nanoscale Systems. *J. Phys. Chem. B*, 113:6583–6599, 2009.

[16] T. R. Calhoun, N. S. Ginsberg, G. S. Schlau Cohen, Y. C. Cheng, M. Ballottari, R. Bassi, and G. R. Fleming. Quantum Coherence Enabled Determination of the Energy Landscape in Light-Harvesting Complex II. *J. Phys. Chem. B*, 113:16291–16295, 2009.

[17] I. Kassal, J. Yuen Zhou, and S. Rahimi Keshari. Does Coherence Enhance Transport in Photosynthesis? *J. Phys. Chem. Lett.*, 4(3):362–367, 2013.

[18] M. Mohseni, P. Rebentrost, S. Lloyd, and A. Aspuru Guzik. Environment-assisted quantum walks in photosynthetic energy transfer. *J. Chem. Phys.*, 129:174106, 2008.

[19] M. B. Plenio and S. F. Huelga. Dephasing-assisted transport: Quantum network and biomolecules. *New J. Phys.*, 10:113019, 2008.

[20] P. Rebentrost, M. Mohseni, I. Kassal, S. Lloyd, and A. Aspuru Guzik. Environment-assisted quantum transport. *New J. Phys.*, 11:033003, 2009.

[21] F. Caruso, A. W. Chin, A. Datta, S. F. Huelga, and M. B. Plenio. Highly efficient energy excitation transfer in light-harvesting complexes: The fundamental role of noise-assisted transport. *J. Chem. Phys.*, 131:105106, 2009.

[22] T. Brixner, J. Stenger, H. M. Vaswani, M. Cho, R. E. Blankenship, and G. R. Fleming. Two-dimensional Spectroscopy of Electronic Couplings in Photosynthesis. *Nature*, 434:625–628, 2005.

[23] G. Panitchayangkoon, D. Hayes, K. A. Fransted, J. R. Caram, E. Harel, J. Wen, R. E. Blankenship, and G. S. Engel. Long-lived Quantum Coherence in Photosynthetic Complexes at Physiological Temperature. *Proc. Natl. Acad. Sci. USA*, 107:12766–12770, 2010.

[24] E. Collini, C. Y. Wong, K. E. Wilk, P. M. G. Curmi, P. Brumer, and G. D. Scholes. Coherently Wired Light-harvesting in Photosynthetic Marine Algae at Ambient Temperature. *Nature*, 463(7281):644–647, 2010.

[25] P. G. Wolynes. Some quantum weirdness in physiology. *Proc. Natl. Acad. Sci. USA*, 106:17247–17248, 2009.

[26] F. Fassioli, A. Nazir, and A. Olaya Castro. Quantum State Tuning of Energy Transfer in a Correlated Environment. *J. Phys. Chem. Lett.*, 1:2139–2143, 2010.

[27] G. R. Fleming, S. Huelga, and M. Plenio. Focus on Quantum Effects and Noise in Biomolecules. *New J. Phys.*, 12:065002, 2010.

[28] P. Nalbach, J. Eckel, and M. Thorwart. Quantum coherent biomolecular energy transfer with spatially correlated fluctuations. *New J. Phys.*, 12:065043, 2010.

[29] A. Nazir. Correlation-Dependent Coherent to Incoherent Transitions in Resonant Energy Transfer Dynamics. *Phys. Rev. Lett.*, 103:146404, 2009.

[30] J. Strümpfer and K. Schulten. The Effect of Correlated Bath Fluctuations on Exciton Transfer. *J. Chem. Phys.*, 134:095102, 2011.

[31] C. Olbrich, J. Strümpfer, K. Schulten, and U. Kleinekathöfer. Theory and Simulation of the Environmental Effects on FMO Electronic Transitions. *J. Phys. Chem. Lett.*, 2:1771–1776, 2011.

[32] G. D. Scholes, G. R. Fleming, A. Olaya Castro, and R. van Grondelle. Lessons from Nature About Solar Light Harvesting. *Nat. Chem.*, 3:763–764, 2011.

[33] T. Mirkovic, E. E. Ostroumov, M. Anna, R. van Grondelle, Govindjee, and G. D. Scholes. Light Absorption and Energy Transfer in the Antenna Complexes of Photosynthetic Organisms. *Chem. Rev.*, 117(2):249–293, 2017.

[34] D. Abramavicius, B. Palmieri, D. V. Voronine, F. Sanda, and S. Mukamel. Coherent multidimensional optical spectroscopy of excitons in molecular aggregates; quasiparticle versus supermolecule perspectives. *Chem. Rev.*, 109:2350–2358, 2009.

[35] R. Agarwal, A. H. Rizvi, B. S. Prall, J. D. Olsen, C. N. Hunter, and G. R. Fleming. Nature of Disorder and Inter-Complex Energy Transfer in LH2 at Room Temperature: A Three Pulse Photon Echo Peak Shift Study. *J. Phys. Chem. A*, 106:7573–7578, 2002.

[36] S. Georgakopoulou, R. van Grondelle, and G. van der Zwan. Circular dichroism of carotenoids in bacterial light-harvesting complexes: Experiments and modeling. *Biophys. J.*, 87:3010–3022, 2004.

[37] J. T. M. Kennis, A. M. Streltsov, H. Permentier, T. J. Aartsma, and J. Amesz. Exciton Coherence and Energy Transfer in the LH2 Antenna Complex of *Rhodopseudomonas acidophila* at Low Temperature. *J. Phys. Chem. B*, 101:8369–8374, 1997.

[38] V. Novoderezhkin, M. Wendling, and R. van Grondelle. Intra- and interband transfers in the B800-B850 antenna of *Rhodospirillum molischianum*: Redfield theory modeling of polarized pump-probe kinetics. *J. Phys. Chem. B*, 107:11534–11548, 2003.

[39] T. Pullerits, M. Chachisvilis, and V. Sundström. Exciton Delocalization Length in the B850 Antenna of Rhodobacter sphaeroides. *J. Phys. Chem.*, 100(25):10787–10792, 1996.

[40] T. Renger and R. A. Marcus. On the Relation of Protein Dynamics and Exciton Relaxation in Pigment Protein Complexes: An Estimation of the Spectral Density and a Theory for the Calculation of Optical Spectra. *J. Chem. Phys.*, 116:9997–10019, 2002.

[41] G. Britton amd S. Liaaen-Jensen amd H. Pfander. *Carotenoids*. Vol. 4: Natural Functions, Birkhäuser Basel, 2008.

[42] K. McLuskey, S. M. Prince, R. J. Cogdell, and N. W. Isaacs. The crystallographic structure of the b800-820 lh3 light-harvesting complex from the purple bacteria rhodopseudomonas acidophila strain 7050. *Biochemistry*, 40:8783–8789, 2001.

[43] W. F. Humphrey, A. Dalke, and K. Schulten. VMD – Visual Molecular Dynamics. *J. Mol. Graph.*, 14:33–38, 1996.

[44] G. McDermott, S. M. Prince, A. A. Freer, A. M. Hawthornthwaite Lawless, M. Z. Papiz, R. J. Cogdell, and N. W. Isaacs. Crystal structure of an integral membrane light-harvesting complex from photosynthetic bacteria. *Nature*, 374:517–521, 1995.

[45] J. Koepke, X. Hu, C. Muenke, K. Schulten, and H. Michel. The crystal structure of the light harvesting complex II (B800-850) from *Rhodospirillum molischianum*. *Structure*, 4:581–597, 1996.

[46] R. G. Alden, E. Johnson, V. Nagarajan, W. W. ParsonC. J. Law, and R. G. Cogdell. Calculations of Spectroscopic Properties of the LH2 Bacteriochlorophyll: Protein Antenna Complex from *Rhodopseudomonas acidophila*. *J. Phys. Chem. B*, 101:4667–4680, 1997.

[47] X. Hu, T. Ritz, A. Damjanović, and K. Schulten. Pigment Organization and Transfer of Electronic Excitation in the Photosynthetic Unit of Purple Bacteria. *J. Phys. Chem. B*, 101:3854–3871, 1997.

[48] C. P. van der Vegte, J. D. Prajapati, U. Kleinekathöfer, J. Knoester, and T. L. C. Jansen. Atomistic Modeling of Two-Dimensional Electronic Spectra and Excited State Dynamics for a Light Harvesting 2 Complex. *J. Phys. Chem. B*, 119:1302–1313, 2015.

[49] L. M. P. Beekman, F. van Mourik, M. R. Jones, H. Visser, C. N. Hunter, and R. van Grondelle. Trapping Kinetics in Mutants of the Photosynthetic Purple Bacterium Rhodobacter Sphaeroides: Influence of the Charge Separation Rate and Consequences for the Rate-Limiting Step in the Light-Harvesting Process. *Biochemistry*, 33:3143–3147, 1994.

[50] M. T. Milder, B. Brüggemann, R. van Grondelle, and J. L. Herek. Revisiting the optical properties of the FMO protein. *Photosynth. Res.*, 104:257–264, 2010.

[51] E. J. Boekema G. T. Oostergetel, H. van Amerongen. The chlorosome: a prototype for efficient light harvesting in photosynthesis. *Photosynth. Res*, 104:245–255, 2010.

[52] R.E. Fenna, B.W. Matthews, J.M. Olson, and E.K. Shaw. Structure of a bacteriochlorophyll-protein from the green photosynthetic bacterium Chlorobium limicola: Crystallographic evidence for a trimer. *J. Mol. Biol.*, 84(2):231–240, 1974.

[53] B. W. Matthews, R. E. Fenna, M. C. Bolognesi, M. F. Schmid, and J. M. Olson. Structure of a bacteriochlorophyll a-protein from the green photosynthetic bacterium *Prosthecochloris aestuarii*. *J. Mol. Biol.*, 131:259–265, 1979.

[54] D. E. Tronrud, M. F. Schmid, and B. W. Matthews. Structure and X-ray amino acid sequence of a bacteriochlorophyll a protein from *Prosthecochloris aestuarii* refined at 1.9 A resolution. *J. Mol. Biol.*, 188:443–444, 1986.

[55] D. E. Tronrud, J. Wen, L. Gay, and R. E. Blankenship. The structural basis for the difference in absorbance spectra for the FMO antenna protein from various green sulfur bacteria. *Photosynth. Res.*, 100:79–87, 2009.

[56] J. Adolphs and T. Renger. How proteins trigger excitation energy transfer in the FMO complex of green sulfur bacteria. *Biophys J*, 91(8):2778–2797, 2006.

[57] G. Ritschel, J. Roden, W. T. Strunz, A. Aspuru Guzik, and A. Eisfeld. Absence of Quantum Oscillations and Dependence on Site Energies in Electronic Excitation Transfer in the Fenna-Matthews-Olson Trimer. *J. Phys. Chem. Lett.*, 2:2912–2917, 2011.

[58] D. M. Wilkins and N. S. Dattani. Why quantum coherence is not important in the fenna–matthews–olsen complex. *J. Chem. Theory Comp.*, 11:3411–3419, 2015.

[59] C. D. van der Weij-De Wit, A. B. Doust, I. H M. van Stokkum, J. P. Dekker, K. E. Wilk, P. M G. Curmi, G. D. Scholes, and R. van Grondelle. How Energy Funnels from the Phycoerythrin Antenna Complex to Photosystem I and Photosystem Ii in Cryptophyte Rhodomonas Cs24 Cells. *J. Phys. Chem. B*, 110(49):25066–25073, 2006.

[60] A. N. Glazer. Light Harvesting in Phycobilisomes. *Ann. Rev. Biophys. Chem.*, 1985.

[61] K. E. Wilk, S. J Harrop, L. Jankova, D. Edler, G. Keenan, F. Sharples, R. G Hiller, and P. MG Curmi. Evolution of a Light-harvesting Protein by Addition of New Subunits and Rearrangement of Conserved Elements: Crystal Structure of a Cryptophyte Phycoerythrin at 1.63-å Resolution. *Proc. Natl. Acad. Sci. USA*, 96(16):8901–8906, 1999.

[62] A. B. Doust, C. N. Marai, S. J. Harrop, K. E. Wilk, P. M. Curmi, and G. D. Scholes. Developing a Structure-function Model for the Cryptophyte Phycoerythrin 545 using Ultrahigh Resolution Crystallography and Ultrafast Laser Spectroscopy. *J. Mol. Biol.*, 344:135–143, 2004.

[63] S. J. Harrop, K. E. Wilk, R. Dinshaw, E. Collini, T. Mirkovic, C. Y. Teng, D. G. Oblinsky, B. R. Green, K. Hoef Emden, R. G. Hiller, G. D. Scholes, and P. M. G. Curmi. Single-residue insertion switches the quaternary structure and exciton states of cryptophyte light-harvesting proteins. *Proc. Natl. Acad. Sci. U. S. A.*, 111(26):2666–2675, 2014.

[64] H. Hossein-Nejad, C. Curutchet, A. Kubica, and G. D. Scholes. Delocalization-Enhanced Long-Range Energy Transfer between Cryptophyte Algae PE545 Antenna Proteins. *J. Phys. Chem. B*, 115:5243–5243, 2011.

[65] L. Viani, C. Curutchet, and B. Mennucci. Spatial and Electronic Correlations in the PE545 Light-Harvesting Complex. *J. Phys. Chem. Lett.*, 4(3):372–377, 2013.

[66] M. Aghtar, J. Strümpfer, C. Olbrich, K. Schulten, and U. Kleinekathöfer. Different Types of Vibrations Interacting with Electronic Excitations in Phycoerythrin 545 and Fenna-Matthews-Olson Antenna Systems. *J. Phys. Chem. Lett.*, 5:3131–3137, 2014.

[67] A. B. Doust, I. H M. van Stokkum, D. S. Larsen, K. E. Wilk, P. M G. Curmi, R. van Grondelle, and G. D. Scholes. Mediation of Ultrafast Light-harvesting by a Central Dimer in Phycoerythrin 545 studied by Transient Absorption and Global Analysis. *J. Phys. Chem. B*, 109(29):14219–14226, 2005.

[68] L. D. Pulfrey. *Photovoltaic Power Generation.* Van Nostrand Reinhold Co, New York, 1978.

[69] J. Nelson. Polymer:fullerene bulk heterojunction solar cells. *Mat. Today*, 14:462–470, 2011.

[70] R. Po, C. Carbonera, A. Bernardi, F. Tinti, and N. Camaioni. Polymer- and carbon-based electrodes for polymer solar cells: Toward low-cost, continuous fabrication over large area. *Solar Energy Materials and Solar Cells*, 100, 2012.

[71] M. C. Scharber, D. Mühlbacher, M. Koppe, P. Denk, C. Waldauf, A. J. Heeger, and C. J. Brabec. Design rules for donors in bulk-heterojunction solar cells-towards 10% energy-conversion efficiency. *Advanced Materials*, 6, 2006.

[72] M. Jørgensen, K. Norrman, and F.C. Krebs. Stability/degradation of polymer solar cells. *Solar Energy Materials and Solar Cells*, 7, 2008.

[73] Y. Jingbi, D. Letian, Y. Ken, K. Takehito, O. Kenichiro, M. Tom, E. Keith, C. Chun-Chao, G. Jing, L. Gang, and Y. Yang. A polymer tandem solar cell with 10.6% power conversion efficiency. *Nature Comm.*, 4, 2013.

[74] J. Liu, W. Zhou, J. Liu, I. Howard, G. Kilibarda, S. Schlabach, D. Coupry, M. Addicoat, S. Yoneda, Y. Tsutsui, T. Sakurai, S. Seki, Z. Wang, P. Lindemann, E. Redel, T. Heine, and C. Wöll. Photoinduced Charge-Carrier Generation in Epitaxial MOF Thin Films: High Efficiency as a Result of an Indirect Electronic Band Gap? *Angew. Chem. Int. Ed.*, 54:7441–7445, 2015.

[75] A. V. Akimov and O. V. Prezhdo. Persistent Electronic Coherence Despite Rapid Loss of Electron-Nuclear Correlation. *J. Phys. Chem. Lett.*, 4:3857–3864, November 2013.

[76] C. König and J. Neugebauer. Quantum chemical description of absorption properties and excited-state processes in photosynthetic systems. *ChemPhysChem*, 13:386–425, 2011.

[77] C. Curutchet and B. Mennucci. Quantum Chemical Studies of Light Harvesting. *Chem. Rev.*, 117:294–343, 2017.

[78] S. Mukamel. *Principles of Nonlinear Optical Spectroscopy.* Oxford University Press, New York, 1995.

[79] V. May and O. Kühn. *Charge and Energy Transfer in Molecular Systems.* Wiley–VCH, Berlin, 3 edition, 2011.

[80] Y. Tanimura and R. Kubo. Time Evolution of a Quantum System in Contact with a Nearly Gaussian-Markoffian Noise Bath. *J. Phys. Soc. Jpn.*, 58:101, 1989.

[81] M. Schröder, M. Schreiber, and U. Kleinekathöfer. Reduced dynamics of coupled harmonic and anharmonic oscillators using higher-order perturbation theory. *J. Chem. Phys.*, 126:114102–10, 2006.

[82] L. Wang, A. Akimov, and O. V. Prezhdo. Recent progress in surface hopping: 2011-2015. *J. Phys. Chem. Lett.*, 7:2100–2112, 2016.

[83] A. D. McLachlan. A variational solution of the time-dependent Schrodinger equation. *Mol. Phys.*, 8:39, 1964.

[84] D. Marx and J. Hutter. Ab initio molecular dynamics: Theory and Implementation. In J. Grotendorst, editor, *Modern Methods and Algorithms of Quantum Chemistry*, volume 3, pages 329–477, Jülich, 2000. John von Neumann Institute for Computing, NIC Series.

[85] M. Aghtar, J. Liebers, J. Strümpfer, K. Schulten, and U. Kleinekathöfer. Juxtaposing Density Matrix and Classical Path-based Wave Packet Dynamics. *J. Chem. Phys.*, 136(21):214101–9, 2012.

[86] R. Eisberg and R. Resnick. *Quantum Physics of Atoms, Molecules, Solids, Nuclei and Particles.* John Wiley & Sons, Canada, 1974.

[87] J. J. Sakurai and Jim J. Napolitano. *Modern Quantum Mechanics.* Pearson Education Limited, Edinburgh, 2014.

[88] M. Born and R. Oppenheimer. Zur Quantentheorie der Molekeln. *Annalen der Physik*, 389(20):457–484, 1927.

[89] F. Jensen. *Introduction to Computational Chemistry.* John Wiley & Sons, Canada, 2nd edition edition, 2006.

[90] J. Huheey, E. A. Keiter, and R. L. Keiter. *Inorganic Chemistry: Principles of Structure and Reactivity.* Prentice Hall, 4 Edition, 1997.

[91] D. R. Hartree. The wave mechanics of an atom with a non-coulomb central field. part i. theory and methods. *Math. Proc. Camb. Philos.*, 24:89–132, 1928.

[92] J. C. Slater and J. G. Kirkwood. The van der waals forces in gases. *Phys. Rev.*, 37:682, 1931.

[93] E. Hückel. Quantentheoretische beiträge zum benzolproblem-i. die elektronencofiguration dels benzols un verwandter verbindungen. *Zeitschrift für Physik*, 70:204–286, 1931.

[94] R. Hoffmann. An extended hueckel theory. i. hydrocarbons. *J. Chem. Phys.*, 39:1397, 1963.

[95] J. A. Pople, D. P. Santry, and G. A. Segal. Approximate self-consistent molecular orbital theory, I. invariant procedures. *J. Chem. Phys.*, 43, 1965.

[96] J. Ridley and M. C. Zerner. An intermediate neglect of differential overlap technique for spectroscopy: Pyrrole and the azines. *Theor. Chim. Acta*, 32:111–134, 1973.

[97] M. C. Zerner, G. H. Loew, R. F. Kirchner, and U. T. Mueller Westerhoff. An intermediate neglect of differential overlap technique for spectroscopy of transition-metal complexes. Ferrocene. *J. Am. Chem. Soc.*, 102:589–599, 1980.

[98] M. R. Silva Junior and W. Thiel. Benchmark of electronically excited states for semiempirical methods: MNDO, AM1, PM3, OM1, OM2, OM3, INDO/S, and INDO/S2. *J. Chem. Theory Comput.*, 6:1546–1564, 2010.

[99] M. G. Cory, M. C. Zerner, X. Hu, and K. Schulten. Electronic Excitations in Aggregates of Bacteriochlorophylls. *J. Phys. Chem. B*, 102(39):7640–7650, 1998.

[100] M. F Ng, Y. Zhao, and G. H. Chen. Low-lying excited states of light-harvesting system II in purple bacteria. *J. Phys. Chem. B*, 107:9589–9600, 2003.

[101] D. L. Dexter. A theory of sensitized luminescence in solid. *J. Chem. Phys.*, 21:836–850, 1953.

[102] T. Förster. Energiewanderung und fluoreszenz. *Naturwissenschaften*, 33:166–175, 1946.

[103] B.P. Krueger, G.D. Scholes, and G.R. Fleming. Calculation of Couplings and Energy Transfer Pathways Between the Pigments of LH2 by the ab initio Transition Density Cube Method. *J. Phys. Chem. B*, 102:5378–5386, 1998.

[104] T. Förster. Zwischenmolekulare Energiewanderung und Fluoreszenz. *Annalen der Physik*, 437:55–75, 1948.

[105] M. E. Madjet, A. Abdurahman, and T. Renger. Intermolecular coulomb couplings from ab initio electrostatic potentials: Application to optical transitions of strongly coupled pigments in photosynthetic antennae and reaction centers. *J. Phys. Chem. B*, 110:17268–81, 2006.

[106] T. Lu and F. Chen. Multiwfn: A multifunctional wavefunction analyzer. *J. of Comp. Chem.*, 33:580–592, 2012.

[107] G. D. Scholes, C. Curutchet, B. Mennucci, R. Cammi, and J.Tomasi. How Solvent Controls Electronic Energy Transfer and Light Harvesting. *J. Phys. Chem. B*, 111:13253–13265, 2007.

[108] J. Strümpfer and K. Schulten. Light harvesting complex II B850 excitation dynamics. *J. Chem. Phys.*, 131(22):225101–9, 2009.

[109] U. Weiss. *Quantum Dissipative Systems.* World Scientific, Singapore, 2nd edition, 1999.

[110] V. I. Novoderezhkin, A. B. Doust, C. Curutchet, G. D. Scholes, and R. van Grondelle. Excitation Dynamics in Phycoerythrin 545: Modeling of Steady-state Spectra and Transient Absorption with Modified Redfield Theory. *Biophys. J.*, 99:344–352, 2010.

[111] A. Damjanović, I. Kosztin, U. Kleinekathöfer, and K. Schulten. Excitons in a Photosynthetic Light-Harvesting System: A Combined Molecular Dynamics, Quantum Chemistry and Polaron Model Study. *Phys. Rev. E*, 65:031919, 2002.

[112] C. Olbrich and U. Kleinekathöfer. Time-dependent Atomistic View on the Electronic Relaxation in Light-harvesting System II. *J. Phys. Chem. B*, 114:12427–12437, 2010.

[113] S. Valleau, A. Eisfeld, and A. Aspuru Guzik. On the Alternatives for Bath Correlators and Spectral Densities from Mixed Quantum-classical Simulations. *J. Chem. Phys.*, 137(22):224103–13, 2012.

[114] M. Ceccarelli, P. Procacci, and M. Marchi. An ab initio force field for the cofactors of bacterial photosynthesis. *J. Comput. Chem.*, 24:129–132, 2003.

[115] P. L. Freddolino, C. B. Harrison, Y. Liu, and K. Schulten. Challenges in protein folding simulations: Timescale, representation, and analysis. *Nature Physics*, 6:751–758, 2010.

[116] U. Kleinekathöfer, B. Isralewitz, M. Dittrich, and K. Schulten. Domain motion of individual F_1-ATPase β-subunits during unbiased molecular dynamics simulations. *J. Phys. Chem. A*, 115:7267–7274, 2011.

[117] F. Khalili Araghi, J. Gumbart, P. C. Wen, M. Sotomayor, E. Tajkhorshid, and K. Schulten. Molecular Dynamics Simulations of Membrane Channels and Transporters. *Curr. Opin. Struct. Biol.*, 19:128–137, 2009.

[118] H. Grubmüller and K. Schulten. Special issue: Advances in molecular dynamics simulations. *J. Struct. Biol.*, 157:443, 2007.

[119] N. Koga and S. Takada. Folding-based molecular simulations reveal mechanisms of the rotary motor F_1-ATPase. *Proc. Natl. Acad. Sci. USA*, 103:5367–5372, 2006.

[120] S. Pezeshki, C. Chimerel, A. Bessenov, M. Winterhalter, and U. Kleinekathöfer. Understanding ion conductance on a molecular level: An all-atom modeling of the bacterial porin OmpF. *Biophys. J.*, 97:1898–1906, 2009.

[121] R. Schulz, A. V. Vargiu, F. Collu, U. Kleinekathöfer, and P. Ruggerone. Functional Rotation of the Transporter AcrB: Insights into Drug Extrusion from Simulations. *PLoS Comput. Biol.*, 6:e1000806, 2010.

[122] A.D. MacKerell, D. Bashford, M. Bellott, R.L. Dunbrack, J.D. Evanseck, M.J. Field, S. Fischer, J. Gao, H. Guo, S. Ha, D. Joseph McCarthy, L. Kuchnir, K. Kuczera, F.T.K. Lau, C. Mattos, S. Michnick, T. Ngo, D.T. Nguyen, B. Prodhom, W.E. Reiher, B. Roux, M. Schlenkrich, J.C. Smith, R. Stote, J. Straub, M. Watanabe, J. Wiorkiewicz Kuczera, D. Yin, and M. Karplus. All-Atom Empirical Potential for Molecular Modeling and Dynamics Studies of Proteins. *J. Phys. Chem. B*, 102:3586–3616, 1998.

[123] W. D. Cornell, P. Cieplak, C. I Bayly, I. R. Gould, K. M. Merz, D. M. Ferguson, D. C. Spellmeyer, T. Fx, J. W. Caldwell, and P. A. Kollman. A second generation force field for the simulation of proteins, nucleic acids, and organic molecules. *journal of the American Chemical Society*, 117(19):5179–5197, 1995.

[124] D. M. Lockwood, H. Hwang, and P. J. Rossky. Electronic Decoherence in Condensed Phases. *Chem. Phys.*, 268:285–293, 2001.

[125] R. Kubo. Stochastic Theory of Line Shape. In D. ter Haar, editor, *Fluctuation, Relaxation and Resonance in Magnetic Systems*, pages 23–68, Edinburgh, 1962. Oliver & Boyd.

[126] M. I. Mallus, M. Aghtar, S. Chandrasekaran, G. Lüdemann, M. Elstner, and U. Kleinekathöfer. Relation between Dephasing Time and Energy Gap Fluctuations in Biomolecular Systems. *J. Phys. Chem. Lett.*, 7:1102–1108, 2016.

[127] P. Hamm and M. Zanni. *Concepts and Methods of 2D Iinfrared Sectroscopy.* Cambridge University Press, New York, 2011.

[128] J. Schmidt, N. Sundlass, and J. Skinner. Line Shapes and Photo Echoes within a Generalized Kubo Model. *Chem. Phys. Lett.*, 378:559–566, 2003.

[129] C. Narth, N. Gillet, F. Cailliez, B. Levy, and de la Lande A. Electron transfer, decoherence, and protein dynamics: Insights from atomistic simulations. *Acc. Chem. Res*, 48:1090–1097, 2015.

[130] D. N. Beratan, C. Liu, A. Migliore, N. F. Polizzi, S. S. Skourti, P. Zhang, and Y. Zhang. Charge transfer in dynamical biosystems, or the treachery of (static) images. *Acc. Chem. Res*, 48:474–481, 2015.

[131] F. Francesca, R. Dinshaw, P. C. Arpin, and G. D. Scholes. Photosynthetic light harvesting: excitons and coherence. *J. Roy. Soc. Interface.*, 11(92):1742–5662, March 2014.

[132] P. D. Dahlberg, G. J. Norris, C. Wang, S. Viswanathan, V. P. Singh, and G. S. Engel. Coherences observed in vivo in photosynthetic bacteria using two-dimensional electronic spectroscopy. *J. Chem. Phys.*, 143:101101, 2015.

[133] T. Joutsuka, W. H. Thompson, and D. Laage. Vibrational quantum decoherence in liquid wate. *J. Phys. Chem. Lett.*, 7:616–621, 2016.

[134] K. L. Wells, Z. Zhang, J. R. Rouxel, and H.-S. Tan. Measuring the spectral diffusion of chlorophyll a using two-dimensional electronic spectroscopy. *J. Phys. Chem. B*, 117:2294–2299, 2013.

[135] R. Moca, S. R. Meech, and I. A. Heisler. Two-dimensional electronic spectroscopy of chlorophyll a: Solvent dependent spectral evolution. *J. Phys. Chem. B*, 119:8623–8630, 2013.

[136] D. M. Lockwood, H. Hwang, and P. J. Rossky. Electronic decoherence in condensed phases. *Chem. Phys.*, 268:285–293, 2001.

[137] H. Hwang and P. J Rossky. An analysis of electronic dephasing in the spin-boson model. *J. Chem. Phys.*, 120:11380–11385, 2004.

[138] H. Hwang and P. J Rossky. Electronic decoherence induced by intramolecular vibrational motions in a betaine dye molecule. *J. Phys. Chem. B*, 108:6723–6732, 2004.

[139] O. V. Prezhdo and P. J Rossky. Evaluation of quantum transition rates from quantum-classical molecular dynamics simulations. *J. Chem. Phys.*, 107:5863–5878, 1997.

[140] A. de la Lande, J. Řezáč, B. Lévy, B. C. Sanders, and D. R. Salahub. Transmission coefficients for chemical reactions with multiple states: Role of quantum decoherence. *J. Am. Chem. Soc*, 133:3883–3894, 2011.

[141] A. W. Jasper and D. G. Truhlar. Electronic decoherence time for non-born-oppenheimer trajectories. *J. Chem. Phys.*, 123:064103, 2005.

[142] M. Souaille and M. Marchi. Nuclear dynamics and electronic transition in a photosynthetic reaction center. *J. Am. Chem. Soc.*, 119:3948–3958, 1997.

[143] M. Aghtar, C. Strümpfer, J/.and Olbrich, K. Schulten, and U. Kleinekathöfer. The FMO Complex in a Glycerol-Water Mixture. *J. Phys. Chem. B*, 117(24):7157–7163, 2013.

[144] S. Chandrasekaran, M. Aghtar, S. Valleau, A. Aspuru-Guzik, and U. Kleinekathöfer. Influence of force fields and quantum chemistry approach on spectral densities of bchl a in solution and in fmo proteins. *J. Phys. Chem. B*, 119:9995–10004, 2015.

[145] T. Kubař, U. Kleinekathöfer, and M. Elstner. Solvent Fluctuations Drive the Hole Transfer in DNA: a Mixed Quantum-Classical Study. *J. Phys. Chem. B*, 113:13107–13117, 2009.

[146] G. Lüdemann, P. B. Woiczikowski, T. Kubař, M. Elstner, and T. B. Steinbrecher. Charge Transfer in *E. coli* DNA Photolyase: Understanding Polarization and Stabilization Effects via QM/MM Simulations. *J. Phys. Chem. B*, 117(37):10769–10778, 2013.

[147] G. Lüdemann, I. A. Solov'yov, T. Kubař, and M. Elstner. Solvent Driving Force Ensures Fast Formation of a Persistent and Well-Separated Radical Pair in Plant Cryptochrome. *J. Am. Chem. Soc.*, 137(3):1147–1156, 2015.

[148] J. Schmidt, N. Sundlass, and J. Skinner. Line shapes and photon echoes within a generalized kubo model. *Chem. Phys. Lett.*, 378:559–566, 2003.

[149] G. C. Schatz and M. Ratner. *Quantum Mechanics in Chemistry; Prentice Hall*. Englewood Cliffs, NJ, 1993.

[150] J. Liu, S. V. Kilina, S. Tretiak, and O. V. Prezhdo. Ligands slow down pure-dephasing in semiconductor quantum dots. *ACS Nano*, 9:9106–9116, 2015.

[151] M. I. Mallus, M. Aghtar, and U. Kleinekathöfer. Simulation of LH2. (in preparation), 2017.

[152] C. Curutchet, J. Kongsted, A. Munoz Losa, H. Hossein Nejad, G. D. Scholes, and B. Mennucci. Photosynthetic Light-harvesting Is Tuned by the Heterogeneous Polarizable Environment of the Protein. *J. Am. Chem. Soc.*, 133:3078–3084, 2011.

[153] S. Jurinovich, C. Curutchet, and B. Mennucci. The Fenna-Matthews-Olson Protein Revisited: A Fully Polarizable (TD)DFT/MM Description. *ChemPhysChem*, 2014.

[154] A. M. Rosnik and C Curutchet. Theoretical characterization of the spectral density of the water-soluble chlorophyll-binding protein from combined quantum mechanics/molecular mechanics molecular dynamics simulations. *J. Chem. Theory Comput.*, 11:5826–5837, 2015.

[155] S. Jurinovich, L. Viani, C. Curutchet, and B. Mennucci. Limits and potentials of quantum chemical methods in modelling photosynthetic antennae. *Phys. Chem. Chem. Phys.*, 17:30783–30792, 2015.

[156] C. Olbrich, T. L. C. Jansen, J. Liebers, M. Aghtar, J. Strümpfer, K. Schulten, J. Knoester, and U. Kleinekathöfer. From Atomistic Modeling to Excitation Dynamics and Two-dimensional Spectra of the FMO Light-harvesting Complex. *J. Phys. Chem. B*, 115:8609–8621, 2011.

[157] M. Aghtar and U. Kleinekathoöfer. Environmental coupling and population dynamics in the pe545 light-harvesting complex. *J. Lumin.*, 169:406–409, 2016.

[158] J. Liu, A. Neukirch, and O. V. Prezhdo. Phonon-induced puredephasing of luminescence, multiple exciton generation, and fission in silicon clusters. *J. Chem. Phys.*, 139:164303, 2013.

[159] S. Dong, D. Trivedi, S. Chakrabortty, T. Kobayashi, Y. Chan, O. V. Prezhdo, and Z.-H. Loh. Observation of an excitonic quantum coherence in cdse nanocrystals. *Nano Lett*, 15:6875–6882, 2015.

[160] E. Romero, V. I. Novoderezhkin, and R. van Grondelle. Quantum design of photosynthesis for bio-inspired solar-energy conversion. *Nature*, 543(7645):355–365, March 2017.

[161] A. F. Fidler, V. P. Singh, P. D. Long, P. D. Dahlberg, and G. S. Engel. Time Scales of Coherent Dynamics in the Light-Harvesting Complex 2 (LH2) of Rhodobacter sphaeroides. *J. Phys. Chem. Lett.*, pages 1404–1409, April 2013.

[162] A. Boulesbaa and E. Borguet. Capturing the ultrafast vibrational decoherence of hydrogen bonding in interfacial water. *J. Phys. Chem. Lett.*, 7(24):5080–5085, 2016.

[163] A. V. Akimov, R. Long, and O. V. Prezhdo. Coherence penalty functional: A simple method for adding decoherence in Ehrenfest dynamics. *J. Chem. Phys.*, 140(19):–, 2014.

[164] L. Wang, A. Akimov, and O. V. Prezhdo. Recent progress in surface hopping: 2011-2015. *J. Phys. Chem. Lett.*, 7(11):2100–2112, 2016.

[165] S. Chandrasekaran, K. R. Pothula, and U. Kleinekathöfer. Protein arrangement effects on the exciton dynamics in the PE555 Complex. *J. Phys. Chem. B*, page (in press), 2017.

[166] C. Olbrich and U. Kleinekathöfer. From Atomistic Modeling to Electronic Properties of Light-harvesting Systems. In U. Würfel, M. Thorwart, and E. R. Weber, editors, *Quantum Efficiency in Complex Systems, Part II: from Molecular Aggregates to Organic Solar Cells*, volume 85 of *Semiconductors and Semimetals*, pages 83–114, Burlington, 2011. Academic Press.

[167] B. Mennucci and C. Curutchet. The Role of the Environment in Electronic Energy Transfer: a Molecular Modeling Perspective. *Phys. Chem. Chem. Phys.*, 13:11538–11550, 2011.

[168] C. Curutchet, V. I. Novoderezhkin, J. Kongsted, A. Munoz Losa, R. van Grondelle, G. D. Scholes, and B. Mennucci. Energy Flow in the Cryptophyte PE545 Antenna Is Directed by Bilin Pigment Conformation. *J. Phys. Chem. B*, 117:4263–4273, 2013.

[169] J. Gao, W. J. Shi, J. Ye, X. Wang, H. Hirao, and Y. Zhao. QM/MM Modeling of Environmental Effects on Electronic Transitions of the FMO Complex. *J. Phys. Chem. B*, 117(13):3488–3495, 2013.

[170] E. Rivera, D. Montemayor, M. Masia, and D. F. Coker. Influence of Site-Dependent Pigment-Protein Interactions on Excitation Energy Transfer in Photosynthetic Light Harvesting. *J. Phys. Chem. B*, 117(18):5510–5521, 2013.

[171] M. K. Lee and D. F. Coker. Modeling electronic-nuclear interactions for excitation energy transfer processes in light-Harvesting complexes. *J. Phys. Chem. Lett.*, 2016.

[172] F. Zheng, M. Jin, T. Mančal, and Y. Zhao. Study of electronic structures and pigment-protein interactions in the reaction center of thermochromatium tepidum with a dynamic environment. *J. Phys. Chem. B*, 120:10046–10058, 2016.

[173] F. Zheng, S. Fernandez-Alberti, S. Tretiak, and Y. Zhao. Photoinduced intra- and intermolecular energy transfer in chlorophyll a dimer. *J. Phys. Chem. B*, 121:5331–5339, 2017.

[174] H. Zhu, V. May, B. Röder, and T. Renger. Linear absorbance of the pheophorbide-a butanediamine dendrimer P-4 in solution: computational studies using a mixed quantum classical methodology. *J. Chem. Phys.*, 128:154905, 2008.

[175] H. Zhu, V. May, and B. Röder. Mixed quantum classical simulations of electronic excitation energy transfer: The pheophorbide-a DAB dendrimer in solution. *Chem. Phys.*, 351(1-3):117–128, 2008.

[176] T. Nelson, S. Fernandez-Alberti, A. E. Roitberg, and S. Tretiak. Nonadiabatic excited-state molecular dynamics: Treatment of electronic decoherence. *J. Chem. Phys.*, 138, 2013.

[177] P. M. Shenai, S. Fernandez-Alberti, W. P. Bricker, S. Tretiak, and Y. Zhao. Internal conversion and vibrational energy redistribution in chlorophyll a. *J. Phys. Chem. B*, 120:49–58, 2016.

[178] Villy Sundström, Tönunu Pullerits, and Rienk van Grondelle. Photosynthetic Light-Harvesting: Reconciling Dynamics and Structure of Purple Bacterial LH2 Reveals Function of Photosynthetic Unit. *J. Phys. Chem. B*, 103(13):2327–2346, March 1999.

[179] Carolin König and Johannes Neugebauer. Quantum chemical description of absorption properties and excited-state processes in photosynthetic systems. *ChemPhysChem*, 13(2):386–425, February 2012.

[180] Liam Cleary, Hang Chen, Chern Chuang, Robert J. Silbey, and Jianshu Cao. Optimal fold symmetry of LH2 rings on a photosynthetic membrane. *Proc. Natl. Acad. Sci. USA*, 110:8537–8542, May 2013.

[181] Akihito Ishizaki and Graham R. Fleming. Quantum Coherence in Photosynthetic Light Harvesting. *Annu. Rev. Condens. Matter Phys.*, 3(1):333–361, February 2012.

[182] A. W. Chin, J. Prior, R. Rosenbach, F. Caycedo Soler, S. F. Huelga, and M. B. Plenio. The role of non-equilibrium vibrational structures in electronic coherence and recoherence in pigment-protein complexes. *Nat. Phys.*, advance online publication:–, January 2013.

[183] Mirianas Chachisvilis, Oliver Kühn, Tönu Pullerits, and Villy Sundstr öm. Excitons in Photosynthetic Purple Bacteria: Wavelike Motion or Incoherent Hopping? *J. Phys. Chem. B*, 101(37):7275–7283, September 1997.

[184] E. Harel, P. D. Long, and G. S. Engel. Single-shot ultrabroadband two-dimensional electronic spectroscopy of the light-harvesting complex LH2. *Opt. Lett.*, 36:1665–1667, 2011.

[185] Elad Harel and Gregory S. Engel. Quantum coherence spectroscopy reveals complex dynamics in bacterial light-harvesting complex 2 (LH2). *Proc. Natl. Acad. Sci. USA*, 109(3):706–711, January 2012.

[186] Shu-Hao Yeh, Jing Zhu, and Sabre Kais. Population and coherence dynamics in light harvesting complex II (LH2). *J. Chem. Phys.*, 137(8):084110–9, August 2012.

[187] Peter D. Dahlberg, Andrew F. Fidler, Justin R. Caram, Phillip D. Long, and Gregory S. Engel. Energy Transfer Observed in Live Cells Using Two-Dimensional Electronic Spectroscopy. *J. Phys. Chem. Lett.*, 4(21):3636–3640, October 2013.

[188] R. J. Cogdell, N. W. Isaacs, A. A. Freer, T. Howard, A. T. Gardiner, S. M. Prince, and M. Z. Papiz. The structural basis of light-harvesting in purple bacteria. *FEBS Lett.*, 5555:35–39, 2003.

[189] J F Imhoff. Transfer of Rhodopseudomonas acidophila to the new genus Rhodoblastus as Rhodoblastus acidophilus gen. nov., comb. nov. *Int. J. of Syst. Evol. Microbiol.*, 51(5):1863–1866, September 2001.

[190] J. E. Stone, M. Sener, K. L. Vandivort, A. Barragan, A. Singharoy, I. Teo, J. V. Ribeiro, B. Isralewitz, B. Liu, B. C. Goh, J. C. Phillips, C. MacGregor Chatwin, M. Johnson, L. F. Kourkoutis, C.N. Hunter, and K. Schulten. Atomic Detail Visualization of Photosynthetic Membranes with GPU-Accelerated Ray Tracing. *Parallel Comput.*, 55:17–27, 2016.

[191] S. Tretiak, C. Middleton, V. Chernyak, and S. Mukamel. Exciton Hamiltonian for the Bacteriochlorophyll System in the LH2 Antenna Complex ofPurple Bacteria. *J. Phys. Chem. B*, 104:4519–4528, 2000.

[192] A. Damjanović, H. M. Vaswani, P. Fromme, and G. R. Fleming. Chlorophyll Excitations in Photosystem I of *Synechococcus elongatus*. *J. Phys. Chem. B*, 106:10251–10262, 2002.

[193] J. Linnanto and J. Korppi Tommola. Theoretical study of excitation transfer from modified B800 rings of the LH II antenna complex of Rps. acidophila. *Phys. Chem. Chem. Phys.*, 2:3453–3460, 2002.

[194] L. Janosi, I. Kosztin, and A. Damjanović. Theoretical prediction of spectral and optical properties of bacteriochlorophylls in thermally disordered LH2 antenna complexes. *J. Chem. Phys.*, 125:014903, 2006.

[195] J. Linnanto and J. Korppi Tommola. Modelling excitonic energy transfer in the photosynthetic unit of purple bacteria. *Chem. Phys.*, 357:171–180, 2009.

[196] Lu Zhang, Daniel-Adriano Silva, Houdao Zhang, Alexander Yue, YiJing Yan, and Xuhui Huang. Dynamic protein conformations preferentially drive energy transfer along the active chain of the photosystem II reaction centre. *Nat. Commun.*, 5:4170, June 2014.

[197] I. A. Howard, F. Zutterman, G. Deroover, D. Lamoen, and C. Van Alsenoy. Approaches to Calculation of Exciton Interaction Energies for a Molecular Dimer. *J. Phys. Chem. B*, 108:19155–19162, 2004.

[198] M. C. Zwier, J. M. Shorb, and B. P. Krueger. Hybrid molecular dynamics-quantum mechanics simulations of solute spectral properties in the condensed phase: evaluation of simulation parameters. *J. Comput. Chem.*, 28:1572–1581, 2007.

[199] J. S. Kwon, C. M. Choi, H. J. Kim, N. J. Kim, J. Jang, and M. Yang. Combined theoretical modeling of photoexcitation spectrum of an isolated protonated tyrosine. *J. Phys. Chem. A*, 113:2715–2723, 2009.

[200] T. Renger. Theory of excitation energy transfer: from structure to function. *Photosynth. Res.*, 102:471–485, 2009.

[201] M. Z. Papiz, S. M. Prince, T. Howard, R. J. Cogdell, and N. W. Isaacs. The structure and thermal motion of the B800-850 LH2 complex from Rps. acidophila at 2.0 å resolution and 100 k. *J. Mol. Biol.*, 326:1523, 2003.

[202] Narayanan Eswar, Ben Webb, Marc A Marti Renom, MS Madhusudhan, David Eramian, Min-yi Shen, Ursula Pieper, and Andrej Sali. Comparative protein structure modeling using Modeller. *Current Protocols Bioinformatics*, page 5.6, 2006.

[203] K. Vanommeslaeghe, E. Hatcher, C. Acharya, S. Kundu, S. Zhong, J. Shim, E. Darian, O. Guvench, P. Lopes, I. Vorobyov, and A. D. Mackerell. CHARMM general force field: A force field for drug-like molecules compatible with the CHARMM all-atom additive biological force fields. *J. Comput. Chem.*, 31(4):671–690, 2010.

[204] K Vanommeslaeghe and AD MacKerell Jr. Automation of the CHARMM General Force Field (CGenFF) I: bond perception and atom typing. *J. Chem. Inf. Model.*, 52(12):3144–3154, 2012.

[205] K Vanommeslaeghe, E Prabhu Raman, and AD MacKerell Jr. Automation of the CHARMM General Force Field (CGenFF) II: assignment of bonded parameters and partial atomic charges. *J. Chem. Inf. Model.*, 52(12):3155–3168, 2012.

[206] T. Darden, D. York, and L. Pedersen. Particle mesh Ewald: An N log (N) method for Ewald sums in large systems. *J. Chem. Phys.*, 98:10089–10092, 1993.

[207] J. C. Phillips, R. Braun, W. Wang, J. Gumbart, E. Tajkhorshid, E. Villa, C. Chipot, R. D. Skeel, L. Kale, and K. Schulten. Scalable Molecular Dynamics with Namd. *J. Comput. Chem.*, 26:1781–1802, 2005.

[208] R. J. Cogdell, A. Gall, and J. Köhler. The architecture and function of the light-harvesting apparatus of purple bacteria: from single molecules to in vivo membranes. *Q. Rev. Biophys.*, 39:227–324, 2006.

[209] T. L. C. Jansen and J. Knoester. Nonadiabatic effects in the two-dimensional infrared spectra of peptides: alanine dipeptide. *J. Phys. Chem. B*, 110:22910–22916, 2006.

[210] T. L. C. Jansen and J. Knoester. Waiting Time Dynamics in Two-Dimensional Infrared Spectroscopy. *Acc. Chem. Res.*, 42:1405–1411, 2009.

[211] H. Zhu, B. Röder, and V. May. Time and Frequency Resolved Spontaneous Emission from Supramolecular Pheophorbide-a Complexes: A Mixed Quantum Classical Computation. *Chem. Phys.*, 362:19–26, 2009.

[212] S. Yang, D. Z. Xu, Z. Song, and C. P. Sun. Dimerization-assisted energy transport in light-harvesting complexes. *J. Chem. Phys.*, 132(23):234501–10, June 2010.

[213] Seogjoo Jang, Robert J. Silbey, Ralf Kunz, Clemens Hofmann, and Jürgen Köhler. Is There Elliptic Distortion in the Light Harvesting Complex 2 of Purple Bacteria? *J. Phys. Chem. B*, 115(44):12947–12953, September 2011.

[214] Daniel R. Martin and Dmitry V. Matyushov. Non-Gaussian Statistics and Nanosecond Dynamics of Electrostatic Fluctuations Affecting Optical Transitions in Proteins. *J. Phys. Chem. B*, 116(34):10294–10300, August 2012.

[215] B.R. Weinberger, M. Akhtar, and S. C. Gau. Polyacetylene photovoltaic devices. *Synth. Met.*, 4:187–197, 1982.

[216] H. Hoppe and N. S. Sariciftci. Organic solar cells: An overview. *J. Mat. Res.*, 19:1924–1945, 2004.

[217] W. Cao and J. Xue. Recent progress in organic photovoltaics: device architecture and optical design. *Energy & Environ. Science*, 7:2123, 2014.

[218] R. King, D. Bhusari, D. Larrabee, X.-Q. Liu, E. Rehder, K. Edmondson, H. Cotal, R. K. Jones, J. H. Ermer, C. M. Fetzer, D. C. Law, and N. H. Karam. Solar cell generations over 40% efficiency. *Progress in Photovoltaics*, 20:801–815, 2012.

[219] D. Kearns and M. Calvin. Photovoltaic effect and photoconductivity in laminated organic systems. *J. Chem. Phys.*, 29:950, 1958.

[220] J. M. Halls, K. Pichler, and R. H. Friend. Exciton diffusion and dissociation in a poly(p-phenylenevinylene)/c_{60} heterojunction photovoltaic cell. *Appl. Phys. Lett.*, 68:3120–22, 1996.

[221] H. Zhou, X. Li, T. Fan, F. E. Osterloh, J. Ding, E. M. Sabio, D. Zhang, and Q. Guo. Light harvesting: Artificial inorganic leafs for efficient photochemical hydrogen production inspired by natural photosynthesis. *Adv. Mater.*, 22:951–956, 2010.

[222] S. R. Batten, N. R. Champness, X.-M. Chen, J. Garcia-Martinez, S Kitagawa, L Öhrström, M O'Keeffe, M.P. Suh, and J. Reedijk. Terminology of metal–organic frameworks and coordination polymers (iupac recommendations 2013). *Pure Appl. Chem.*, 85:1715, 2013.

[223] A. U. Czaja, N. Trukhanb, and U. Müller. Industrial applications of metal-organic frameworks. *Chem. Soc. Rev.*, 38:1284–1293, 2009.

[224] R. Dutta and B. Bagchia. Effects of dynamic disorder on exciton migration: Quantum diffusion, coherences, and energy. *J. Chem. Phys.*, 145:164907–14, 2016.

[225] S. Chandrasekhar. Stochastic Problems in Physics and Astronomy. *Rev. Mod. Phys.*, 15, 1943.

[226] B. Aradi, B. Hourahine, and Th. Frauenheim. Dftb+, a sparse matrix-based implementation of the dftb method. *J. Phys. Chem. A*, 111:50–68, 2007.

[227] T. Fujita, J. C. Brookes, S. K. Saikin, and A. Aspuru Guzik. Memory-Assisted Exciton Diffusion in the Chlorosome Light-Harvesting Antenna of Green Sulfur Bacteria. *J. Phys. Chem. Lett.*, 3(17):2357–2361, August 2012.

[228] T Fujita, S. Atahan-Evrenk, N. P. D. Sawaya, and A. Aspuru Guzik. Coherent dynamics of mixed frenkel and charge-transfer excitons in dinaphtho[2,3-b:2'3'-f]thieno[3,2-b]-thiophene thin films: The importance of hole delocalization. *J. Phys. Chem. Lett.*, 7(7):1374–1380, 2016.

[229] T. Yamamoto and K. Takimiya. Facile synthesis of highly π-extended heteroaren, dinaphtho[2,3-b:2'3'-f]chalcogenopheno-[3,2-b]chalcogenophenes, and their application to field-effect transistors. *J. Am. Chem. Soc.*, 129:2224–5, 2007.

[230] M. Sener, J. Strumpfer, A. Singharoy, C. N. Hunter, and K. Schulten. Overall energy conversion efficiency of a photosynthetic vesicle. *eLife*, 5:e09541, 2016.